
**AFRL-AFOSR-VA-TR-2022-0027**

# Effects of Redox, Molecular, and Ionic Dopants on the Structure and Electronic Behavior of Haloplumbate Perovskites

**Marder, Seth**
**GEORGIA TECH RESEARCH CORPORATION**
**926 DALNEY ST NW**
**ATLANTA, GA, 30332**
**USA**

**11/18/2021**
**Final Technical Report**



Air Force Research Laboratory
Air Force Office of Scientific Research
Arlington, Virginia 22203
Air Force Materiel Command

# REPORT DOCUMENTATION PAGE

*Form Approved*
*OMB No. 0704-0188*



| **1. REPORT DATE** *(DD-MM-YYYY)* | **2. REPORT TYPE** | **3. DATES COVERED** *(From - To)* |
|---|---|---|
| 18-11-2021 | Final | 15 Aug 2018 - 14 Aug 2021 |

**4. TITLE AND SUBTITLE**
Effects of Redox, Molecular, and Ionic Dopants on the Structure and Electronic Behavior of Haloplumbate Perovskites

**5a. CONTRACT NUMBER**

**5b. GRANT NUMBER**
FA9550-18-1-0499

**5c. PROGRAM ELEMENT NUMBER**
61102F

**6. AUTHOR(S)**
Seth Marder

**5d. PROJECT NUMBER**

**5e. TASK NUMBER**

**5f. WORK UNIT NUMBER**

**7. PERFORMING ORGANIZATION NAME(S) AND ADDRESS(ES)**
GEORGIA TECH RESEARCH CORPORATION
926 DALNEY ST NW
ATLANTA, GA 30332
USA

**8. PERFORMING ORGANIZATION REPORT NUMBER**

**9. SPONSORING/MONITORING AGENCY NAME(S) AND ADDRESS(ES)**
AF Office of Scientific Research
875 N. Randolph St. Room 3112
Arlington, VA 22203

**10. SPONSOR/MONITOR'S ACRONYM(S)**
AFRL/AFOSR RTB2

**11. SPONSOR/MONITOR'S REPORT NUMBER(S)**
AFRL-AFOSR-VA-TR-2022-0027

**12. DISTRIBUTION/AVAILABILITY STATEMENT**
A Distribution Unlimited: PB Public Release

**13. SUPPLEMENTARY NOTES**

**14. ABSTRACT**

The Marder group (Georgia Institute of Technology / University of Colorado) and the Snaith group (University of Oxford), along with a number of additional collaborators – including Bernard Kippelen and Carlos Silva (Georgia Tech), Norbert Koch (Humboldt University of Berlin), Henk Bolink (Valencia), Oanu Jurchescu (Wake Forest University), Tatiana Timofeeva (New Mexico Highlands University), Nathan Jui (Emory), Ed Sargent (Toronto), Ruth Pachter (AFRL), and Shijun Sun (MIT) – have worked together on numerous aspects of relevance to leadhalide perovskite solar cells. These include establishing a method of extrinsically p-doping 3D perovskite materials, providing a potential avenue for highly efficient perovskite photovoltaics with improved long-term stability. Analogous n-doping was less successful. p-Doped polymeric hole-extraction materials for both n-i-p and p-i-n perovskite solar cells have been developed, some of which offer advantages in terms of device stability and/or performance over more wellestablished hole-extraction layers, and various methods for crosslinking these layers have been developed. n-Doped electron-extraction layers for n-i-p cells have also been developed, these being based on benzocyclobutene-functionalized fullerenes that, with or without the addition of oligomers bearing multiple benzocyclobutene moieties, become insolubilized on heating to
moderate temperatures. The use of ionic dopants for perovskite cells has also been investigated. A wide range of low-dimensional lead halide perovskites and related materials have also been investigated with a focus on understanding the role of the organic cation's structure in determining the crystal structure of the resulting hybrid material. Some of these materials have also been used to protect the active layers of perovskite solar cells.

**15. SUBJECT TERMS**

| **16. SECURITY CLASSIFICATION OF:** | | | **17. LIMITATION OF ABSTRACT** | **18. NUMBER OF PAGES** | **19a. NAME OF RESPONSIBLE PERSON** |
|---|---|---|---|---|---|
| **a. REPORT** | **b. ABSTRACT** | **c. THIS PAGE** | | | KENNETH CASTER |
| U | U | U | UU | 74 | **19b. TELEPHONE NUMBER** *(Include area code)* 0000 0000 |

Final Technical Report for

# AFOSR funded project "Effects of Redox, Molecular, & Ionic Dopants on the Structure and Electronic Behavior of Haloplumbate Perovskites"

Performance Period: 15 Aug 2018 –14 Aug 2021
Grant Number: 17RT0905 FA9550-18-1-0499
Program Officer: Dr. Kenneth Caster, AFOSR
PI: Seth Marder, Georgia Institute of Technology
Co-PI: Henry Snaith, University of Oxford

**Abstract:** The Marder group (Georgia Institute of Technology / University of Colorado) and the Snaith group (University of Oxford), along with a number of additional collaborators – including Bernard Kippelen and Carlos Silva (Georgia Tech), Norbert Koch (Humboldt University of Berlin), Henk Bolink (Valencia), Oanu Jurchescu (Wake Forest University), Tatiana Timofeeva (New Mexico Highlands University), Nathan Jui (Emory), Ed Sargent (Toronto), Ruth Pachter (AFRL), and Shijun Sun (MIT) – have worked together on numerous aspects of relevance to lead-halide perovskite solar cells. These include establishing a method of extrinsically p-doping 3D perovskite materials, providing a potential avenue for highly efficient perovskite photovoltaics with improved long-term stability. Analogous n-doping was less successful. p-Doped polymeric hole-extraction materials for both n-i-p and p-i-n perovskite solar cells have been developed, some of which offer advantages in terms of device stability and/or performance over more well-established hole-extraction layers, and various methods for crosslinking these layers have been developed. n-Doped electron-extraction layers for n-i-p cells have also been developed, these being based on benzocyclobutene-functionalized fullerenes that, with or without the addition of oligomers bearing multiple benzocyclobutene moieties, become insolubilized on heating to moderate temperatures. The use of ionic dopants for perovskite cells has also been investigated. A wide range of low-dimensional lead halide perovskites and related materials have also been investigated with a focus on understanding the role of the organic cation's structure in determining the crystal structure of the resulting hybrid material. Some of these materials have also been used to protect the active layers of perovskite solar cells.

**CONTENTS**

## I. ACCOMPLISHMENTS

Our originally stated objectives were to:

- develop novel methods for p- and n-doping haloplumbate perovskites, both in bulk and at surfaces;
- understand whether molecular p- and n-dopants can improve perovskite photovoltaic properties;
- examine whether dopant redox levels are best positioned within or outside the perovskite band gap, and what the pros and cons of different doping methods are;
- explore if doping can lead to new applications for 2D and 3D haloplumbate perovskites;
- compare the effects of redox doping of perovskites with the effects of adding other neutral and ionic additives on the influence of grain boundaries on perovskite properties; and
- determine whether a crosslinked p-doped polymeric hole-transport layer can provide for stable and reproducible performance in high-efficiency perovskite photovoltaic cells.

Our proposed technical approaches included the use of various n- and p-dopants in hand or synthesized in the Marder group, as well as synthesis of crosslinkble polymers in the Marder groups, coupled with Snaith's experience in fabrication and testing of perovskite solar cells. In addition, we have also investigated the use crosslinked doped fullerene electron-transport materials, and investigated the relations between the molecular structures of organic cations and the crystal structures of low-dimensional hybrid lead halide perovskites and related materials.

Major activities during the reported period includes: chemical synthesis of established and new dopants; synthesis of known and new crosslinkable hole-transport polymers, and of electron-transport molecular and oligomeric materials; fabrication of partial and full devices in which perovskite active layers are in contact with these dopants, or with hole- or electron-transport materials; and synthesis and characterization of the structures of low-dimensional hybrid lead-halide materials.

Significant achievements include:

• Demonstrating that surface molecular p-doping *is* a feasible route to tune and control the surface properties of metal halide perovskites (although analogous n-doping proved less successful), that this doping results in a shift of work function and an increase in the total conductivity throughout the film, that the resulting p-doped interface constitutes a homojunction with increased hole-selectivity, enhancing the device performance of perovskite solar cells, and that this surface treatment obviates the need to use the commonly employed additive 4-*tert* butylpyridine (*t*BP);

• Showing that the crosslinkable side-chain polymer approach previously developed for use in multilayer organic light-emitting diodes can also be applied successfully to hole-extraction layers in perovskite solar cells, and that one such crosslinked polymer results in comparable initial p-i-n device performance, but improved device stability, to the widely used PolyTPD main-chain polymer;

• Applying the side-chain polymer approach to develop a hole-extraction material that can replace the widely-used spiro-OMeTAD in n-i-p perovskite solar cells, leading to devices with improved heat and light stability and allowing for use of a thinner hole-extraction layer;

• Showing that addition of a poly(methylmethacrylate) functionalized with multiple benzocyclobutene (BCB) groups to a previously reported BCB-fullerene can improve the conductivity of n-doped films of such a polymer and reduce the leaching of dopant ions from the film on washing, and that n-i-p perovskite solar cells using such blends as the active layer exhibit excellent thermal stability;

• Synthesizing a new BCB-functionalized fullerene that can be insolubilized at only 120 °C;

• Showing that ionic additives, most notably 1,3-di-*tert*-butylimidazolium tetrafluoroborate, can lead to significant improvement in open-circuit voltage and efficiency in perovskite solar cells;

• Obtaining a rare-example of a 3x3 corrugated 2D lead-halide perovskite and correlating its unusual crystal structure with characteristics of its $^{207}$Pb NMR spectrum and its photoluminescence behavior;

• Correlating interlayer offsets and distortions of Pb-I-Pb bond angles from ideality in planar 2D lead iodide perovskites with the molecular structures of the organic cations used in these perovskites;

• Characterizing a number of hybrid lead-iodide materials based on a naphthalene diimide diammonium salt emphasizing the structural diversity possibility in organic-lead-halide systems and demonstrating the impact of close contacts between iodide ions and electron-poor organics on optical properties; and

• Identifying features of organic ammonium derivatives, A – specifically hydrogen-bond acceptor character – that favor the formation of $APbI_3$ hybrid lead iodides consisting of 1D chains of face-sharing $PbI_6$ octahedra rather than 2D perovskites $A_2PbI_4$.

Our results have primarily been disseminated to communities of interest through publications journal articles (12 published to date acknowledging this grant; at least 2 more in the process). Several conference presentations have also been made, although fewer than would normally be expected due to the impact of Covid-19 on the scientific conference scene. In-person and virtual presentations have also been made at AFOSR review meetings.

## II. IMPACTS

**Development of the principal discipline(s) of the project**

The principal discipline of the project is that of lead-halide perovskite solar cells. The findings made in the above-described "achievements" sections have had a significant impact in this field, as evidenced by citations of our work. Particularly notably our publication on surface molecular p-doping has been cited 48 times (according to SciFinder, Nov 2021). Our work on hole- and electron-extraction layers has also inspired related approaches in other groups, some of which has already beem published. Our work on low-dimensional perovskites and related materials may help lead to the identification of protective layers for the active layers of perovskite solar cells. Ultimately our findings help advance the field of perovskite solar cells, which can play a role in contributing to low-carbon power generation, both for specific niche AFOSR applications, where lightweight flexible devices are required, but also for more general applications, such as retrofitting of existing silicon solar panels to increase their power generation efficiency.

**Other disciplines:**

Many of the same issues that apply to the development of extraction layers for perovskite solar cells – including control of transport energy levels, insolubilization to allow for solution processing of multilayer devices, and immobilization of dopant ions – are also relevant to other organic and hybrid electronic devices such as organic solar cells, and organic and perovskite light-emitting diodes. Indeed, we have initially (collaboratively) demonstrated one of our crosslinking approaches in the context of organic solar cells. As well as being potential relevant to perovskite

solar cells, our work on low-dimensional perovskites and related materials, which is already quite well cited (two papers with over 25 citations), may have impacts on perovskite light-emitting diodes and also the numerous other fields in which the use of these materials has been proposed, including use in thermochromic, photocatalytic, switchable dielectrics, hybrid ferroelectrics, and third-order nonlinear optics.

**Describe the impact in this reporting period on the development of human resources / teaching and educational experiences**

This project has provided researchers, including three graduate students, two of whom were female, with opportunities to participate in high multidisciplinary collaborative research involving exchange between the two funded institutions (Georgia Tech and Univ. Oxford), but also interactions with numerous collaborators.

## III. CHANGES

**Changes in approach**

In addition to studying doping of the perovskite itself and the use cross-linkable hole-transport layers, leveraging support from a Canadian fellowship for one student we have been able to broaden our investigation to include structure-property relations for low-dimensional hybrid lead-halide materials. This work is nonetheless related to the original objectives in that these materials may in some cases be directly incorporated into perovskite solar cells and in other cases may be what are in fact formed on the surface of the active layer perovskite as a result of using organic amines or ammonium salts as "passivators" or other additives during device fabrication.

**Changes to the primary place of performance from that originally proposed**

Prof. Marder moved during the final period of this program from Georgia Tech (GT) to the University of Colorado at Boulder. However, funds were not transferred to Colorado and accordingly Prof. M. G. Finn at GT served as official PI and official supervisor of one of Prof. Marder's students at GT who worked on the final stages of this project on the US side.

## IV. TECHNICAL UPDATES

### IV.1. Interfacial Modification of Lead-Halide Perovskites

In a typical PSC, both photogenerated holes and electrons are distributed throughout the entire bulk and are separated at the two interfaces, where the absorber is contacted by materials which are hole selective on one side, and electron selective on the other. Consequently, an efficient perovskite solar cell requires charge selective contacts with transport levels that are appropriately aligned with the perovskite bands such that they facilitate good transfer kinetics for electrons/holes while blocking charges of the opposite polarity. Further, to avoid back-transfer and reduce series resistance losses, the charge carrier mobilities should also be high in their respective charge-selective layer. Additionally, the intrinsic charge-carrier density of the selective contact should be sufficiently low to avoid native recombination events. These requirements allow for a reduction of the interfacial recombination that takes place in an operating device. One possible way to further reduce interface recombination is the deliberate and controlled introduction of homojunctions as additional driving mechanisms for charge separation, analogous to traditional p-n junctions.

One strategy enabling the formation of such a homojunction would be to locally dope the perovskite. However, the science of doping is not currently well-established for metal-halide perovskites; many attempts have been made at doping with extrinsic ions, with varying degrees of success.[1-5] While in some cases these ions have been shown to be incorporated into the perovskite material, reports of changes in the density of free carriers in the host perovskite material are rare. However, there are reports of substrate dependent doping density in these materials, where the p- or n-type character of the material can be modulated by varying the nature of the substrate upon which it is crystallized,[6] and of varying the doping density through manipulating the perovskite stoichiometry.[7] A recent study by Cui et al. reports the fabrication of a photovoltaic device based on a perovskite homojunction.[8] Here, the doping density of the perovskite is modulated by stacking perovskite layers in which the perovskite stoichiometry is varied slightly. An n-type perovskite is produced through crystallisation of the perovskite on $TiO_2$, after which a layer of p-type perovskite is deposited on top of the n-type perovskite through thermal evaporation of $PbI_2$ and a subsequent treatment of methylammonium iodide in isopropanol. This creates a homojunction in the perovskite layer, which the authors posit allows for reduced recombination through the establishment of a built-in field. It is unclear however, given the propensity of perovskite films to undergo ion redistribution and homogenization under light and bias, how stable such a system would be under operating conditions.

4-*tert*-Butylpyridine (*t*BP) is a common additive to one of the most widely used hole-transport materials (HTMs) 2,2',7,7'-tetrakis[N,N-di(4-methoxyphenyl)amino]-9,9'-spirobifluorene (spiro-OMeTAD), and is used in most highly efficient (n-i-p) perovskite solar cells. Habisreutinger et al. have previously investigated the mechanistic role of *t*BP in perovskite solar cells, and found that it directly interacts with the perovskite surface, resulting in improved hole selectivity at the perovskite/spiro-OMeTAD interface.[9] However, the interfacial modification is incidental and may cause degradation of the perovskite absorber in the long term.[10-12] To circumvent these problems, we proposed a controlled and deliberate molecular doping strategy at the perovskite/HTM interface to introduce a charge gradient. The injection of a high concentration of holes *via* interfacial electron-transfer doping should give rise to a narrow field which will block carriers of

the opposite polarity (electrons in this case). This should prevent electrons from reaching the surface, thus reducing non-radiative recombination at the perovskite/HTM interface.

To explore this concept, we employed the two one-electron molybdenum tris(dithiolene) ($Mo(dt)_3$) oxidants, molybdenum tris(1-(trifluoroethanoyl)-2-(trifluoromethyl)ethane-1,2-dithiolene ($Mo(tfd\text{-}COCF_3)_3$) and molybdenum tris(1-(methoxycarbonyl)-2-(trifluoromethyl)ethane-1,2-dithiolene ($Mo(tfd\text{-}CO_2Me)_3$) (Fig. 1), which we have previously shown to be effective p-dopants of spiro-OMeTAD in lieu of the hygroscopic lithium bis((trifluomethyl)sulfonyl) imide (Li-TFSI).[13] Not only are these dopants strong oxidising agents, but they are likely ufficiently large to prevent the migration into the bulk material, allowing the doping to be confined to the perovskite surface. We have also made preliminary investigations of the use of an n-dopant – $(RuCp^*mes)_2$ (also shown in Fig 1).

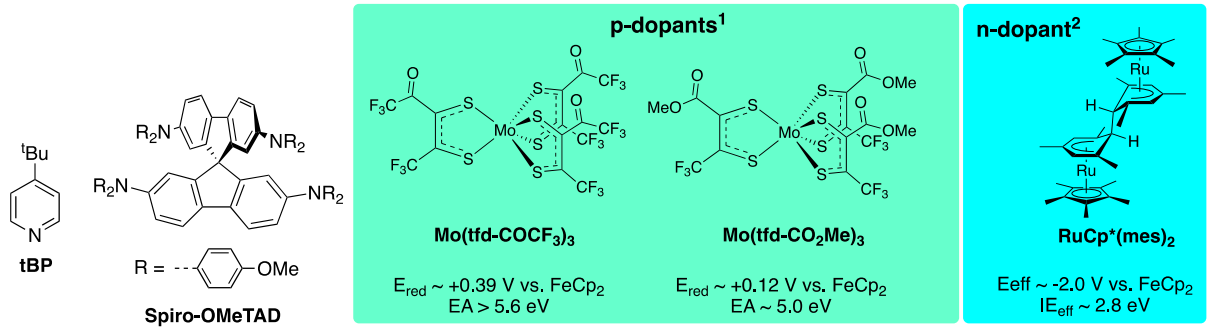


**Fig 1.** Chemical structures of materials discussed in this section.

We mainly focus on $Mo(tfd\text{-}COCF_3)_3$, which is the more oxidizing of the two $Mo(dt)_3$ dopants considered. To investigate whether treating the surface of the perovskite with various concentrations of the Mo-dopant significantly changes the chemical composition of a mixed cation, mixed halide, $FA_{0.85}MA_{0.15}Pb(I_{0.85}Br_{0.15})_3$ perovskite film we treated perovskite films, *via* spin coating, with solutions of $Mo(tfd\text{-}COCF_3)_3$ in chlorobenzene at various concentrations and perform UV-Vis absorption and X-ray diffraction (XRD) measurements. Absorption spectra show no discernible difference between the absorption onsets of the neat and treated perovskite films, suggesting that the chemical composition of the film remains largely unchanged when treated with a 1.0 wt.% solution of the dopant. This is further corroborated by XRD which shows that surface treatment of the films with dilute dopant solutions produces no change in the perovskite crystal structure. These results suggest that the dopant molecules remain at the surface or grain boundaries of the film and are not incorporated into the bulk material. Top-view scanning electron microscope (SEM) images of neat and dopant-treated films suggest no significant changes in the surface morphology of the films when they are treated with very dilute dopant solutions. However, at a concentration of 0.1 wt.%, small, yet distinct particles are visible on the surface of the perovskite film. The density of these particles increases upon treatment with a 1.0 wt.% solution of the dopant. The formation of these particles, which we assign as dopant clusters, on the surface of the perovskite film is likely due to the limited solubility of the $Mo(tfd\text{-}COCF_3)_3$ complex in chlorobenzene. The presence of unreacted dopant is further confirmed through solid-state NMR measurements (see below). At a concentration of 1 wt.%, the dopant solution is very near to its solubility limit, resulting in the formation of a rough and non-uniform film upon deposition.

Kelvin probe (KP) measurements (under $N_2$) on both neat and dopant-treated perovskite films are shown in Fig. 2a; increasing concentrations of Mo(tfd-$COCF_3$)$_3$ result in a significant increase in the of the perovskite work function. The lowest dopant concentration of 0.0001 wt.% produces a shift of 320 meV, while 1.0 wt.% of Mo(tfd-$COCF_3$)$_3$ results in a change of 500 meV. This shift is consistent with the surface of the perovskite becoming increasingly more p-type when it is treated with higher dopant concentrations, suggesting that there is a direct interaction between the dopant molecules and the perovskite surface. If this change in work function occurs because of electron transfer from the perovskite to the dopant complex, we expect both a shift in the Fermi level of the perovskite, as well as the formation of a surface dipole, which would both contribute to the observed shift in the work function (see below). This change in work function also corresponds to a change in the conductivity of the film. The relative conductivities of the neat and dopant-treated perovskite films were determined using dark microwave conductivity measurements (Fig. 2b). Here, we observe that the increase in the overall magnitude of the work function correlates to an increase in the dark conductivity of the film up to a point. At the lowest dopant concentration, the dark conductivity of the treated film is 1.4 times that of the control film. The maximum conductivity achieved for films treated with dopant occurs at 0.1 wt.% where the conductivity of the treated film is approximately twice that of the control film, after which the conductivity begins to decrease. This general increase in the dark conductivity of the perovskite film when it is treated with the Mo(tfd-$COCF_3$)$_3$ dopant is indicative of an increase in the density of mobile charge carriers within the films. The decrease in conductivity which occurs at the highest concentration could possibly be due to two factors: increased cluster formation of the dopant on the surface, which may result in increased recombination, with clusters of unreacted dopant acting as trapping sites, or through making the perovskite material too strongly p-type, which has been shown to result in decreased carrier diffusion lengths.[14] Based on both the size of the dopant molecule, as well as the relatively modest change in the dark conductivity, we can presume that the dopant molecules primarily remain on the surface of the perovskite film, and hence, produce a surface doping effect whereby only the perovskite surface effectively becomes more p-type.

To further investigate the chemistry at the Mo(dt)$_3$/perovskite interface, we perform X-ray and ultraviolet photoelectron spectroscopy (XPS and UPS respectively) studies on neat and dopant-treated perovskite films. p-Doping is expected to shift the core level positions toward lower binding energies. We show the Pb 4f and I 3d spectra in Fig. 3. In both the Pb and I core level signals, we see a spectral shift of between 0.6 eV and 0.7 eV to lower binding energy for the dopant-treated perovskite as compared to the control, consistent with p-doping of perovskite surface. Ultraviolet photoelectron spectroscopy (UPS) and vacuum Kelvin probe (Vac-KP) measurements on undoped and p-doped perovskite thin films. UPS WF values ar in good agreement with the WF obtained from vacuum KP measurements, suggesting that any potential beam damage to the perovskite sample is negligible. UPS data further indicate that the shift in the WF measured by KP is almost entirely due to a shift in the Fermi level of the perovskite with minimal surface dipole contributions. This is somewhat surprising at first sight in that a surface dipole between the positively charged perovskite and the dopant anion overlayer is expected. However, surface roughness could lead to cancelations of dipoles, while the dopant itself is also polar and may orient in such a way as to partially cancel the dipole originating from electron transfer.

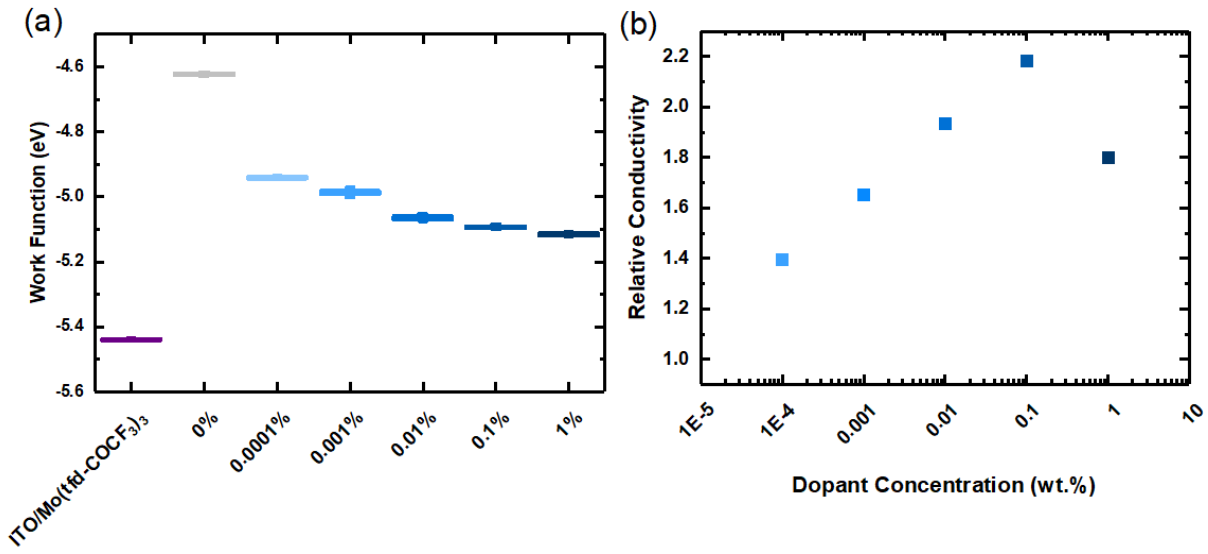


**Fig. 2.** (a) Work functions of the neat Mo(tfd-$COCF_3$)$_3$ dopant, neat perovskite, and perovskite films treated with various concentrations of Mo(tfd-$COCF_3$)$_3$ dopant. (b) Dark conductivities of neat and dopant-treated perovskite films as determined via microwave conductivity.

To gain further insight into the dopant-derived species present on the perovskite surface, we carried out $^{19}$F magic angle spinning (MAS) solid-state NMR spectroscopy on perovskite microcrystals treated with Mo(tfd-$CO_2Me$)$_3$ (while this molecule is slightly less oxidizing, making it a weaker dopant, we have used this dopant complex as it exhibits a single, clear $^{19}$F signal, allowing for a less complex NMR spectrum). These experiments were carried out on single crystals of $FA_{0.85}MA_{0.15}Pb(I_{0.85}Br_{0.15})_3$ grown using the inverse solubility method[15-17] and crushed into a fine powder to increase the surface area, and subsequently treated with a solution of Mo(tfd-$CO_2Me$)$_3$. In Fig.3c we compare the $^{19}$F MAS NMR spectra of the dopant treated perovskite sample to those of neutral Mo(tfd-$CO_2Me$)$_3$, spiro-OMeTAD doped with Mo(tfd-$CO_2Me$)$_3$, and Mo(tfd-$CO_2Me$)$_3$ treated with a strong reductant, $(RhCp^*Cp)_2$. The last two samples serve as model solid-state spectra of materials that contain the paramagnetic Mo(tfd-$CO_2Me$)$_3^-$ monoanion, which forms as a result of the dopant being reduced *via* an electron-transfer reaction. We have previously shown that Mo(tfd-$CO_2Me$)$_3$ can be used to p-dope spiro-OMeTAD, resulting in the formation of the Mo(tfd-$CO_2Me$)$_3^-$ monoanion, and the paramagnetic spiro-OMeTAD$^+$ cation.[13] Similarly, the Mo-dopant reacts with $(RhCp^*Cp)_2$, a much stronger reductant than spiro-OMeTAD, resulting in the formation of the Mo(tfd-$CO_2Me$)$_3^-$ monoanion, and the diamagnetic $RhCp^*Cp^+$ cation.

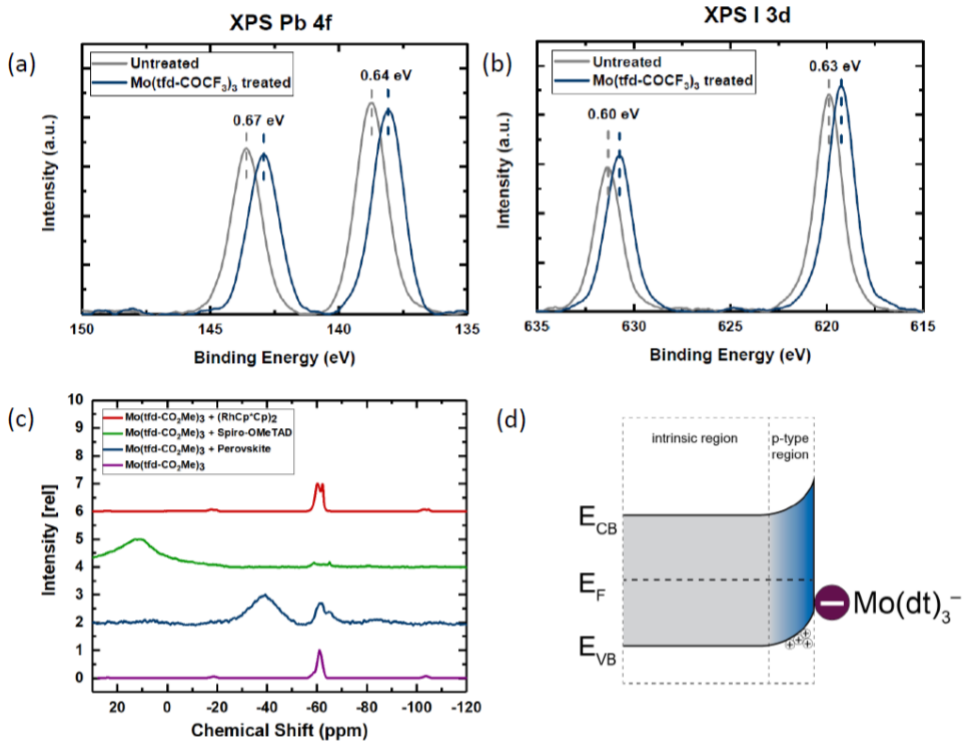


**Fig. 3.** XPS spectra of the (a) Pb 4f and (b) I 3d regions of neat and Mo(tfd-$COCF_3$)$_3$-treated $FA_{0.85}MA_{0.15}Pb(I_{0.85}Br_{0.15})_3$ perovskite films. (c) Solid-state $^{19}F$ MAS NMR spectra of the neat Mo(tfd-$CO_2Me$)$_3$ dopant (deep purple trace), Mo(tfd-$CO_2Me$)$_3$-treated $FA_{0.85}MA_{0.15}Pb(I_{0.85}Br_{0.15})_3$ perovskite crystals (blue trace), Mo(tfd-$CO_2Me$)$_3$-doped spiro-OMeTAD in a 1:100 molar ratio (green trace), and Mo(tfd-$CO_2Me$)$_3$ reacted with a strong reductant, (RhCp*Cp)$_2$ in a 4:1 molar ratio (red trace). (d) Illustration of proposed band bending at the surface of the perovskite crystal due to the electron-transfer reaction with Mo(tfd-$CO_2Me$)$_3$ or Mo(tfd-$COCF_3$)$_3$.

The Mo(tfd-$CO_2Me$)$_3$ + spiro-OMeTAD sample exhibits a dominant, broad peak at 8 ± 1 ppm due to the presence of the Mo(tfd-$CO_2Me$)$_3^-$ monoanion. Additionally, we observe trace signals at -58 ppm (which likely corresponds to unreacted Mo(tfd-$CO_2Me$)$_3$), and at -65 ppm. We hypothesise that the signal at -65 ppm is also due to the presence of the monoanion, but in a different magnetic environment, for example, in close proximity to the unreacted dopant which is diamagnetic, rather than paramagnetic spiro-OMeTAD$^+$. The Mo(tfd-$CO_2Me$)$_3$ + (RhCp*Cp)$_2$ sample, which is expected to contain a 1:1 mixture of neutral and anionic Mo(tfd-$CO_2Me$)$_3$, as well as diamagnetic RhCp*Cp$^+$ ions, in contrast to the Mo(tfd-$CO_2Me$)$_3$ + spiro-OMeTAD spectrum, shows two overlapping, relatively narrow signals at similar chemical shifts to the unreacted dopant. It is evident therefore, that the chemical shift and lineshape of the $^{19}F$ signal from the Mo(tfd-$CO_2Me$)$_3^-$ monoanion is strongly dependent on its magnetic environment, yielding distinctly different spectra when in contact with paramagnetic vs. diamagnetic species. Presumably, in the case of the spiro-OMeTAD sample, most of the dopant monoanions are adjacent to the paramagnetic spiro-OMeTAD$^+$, while in the (RhCp*Cp)$_2$ sample, they interact equally with RhCp*Cp$^+$ ions and unreacted Mo(tfd-$CO_2Me$)$_3$, both of which are diamagnetic species. The dopant treated perovskite exhibits a strong, broad feature at -39 ppm, along with sharper and weaker peaks at -60 ppm and -65 ppm. Based on our model spectra, we can attribute the major peak at -39 ppm to Mo(tfd-$CO_2Me$)$_3^-$ monoanions near other paramagnetic species (specifically other Mo(tfd-$CO_2Me$)$_3^-$ ions on the perovskite surface), while we assign the peak at -60 ppm to unreacted dopant since we observe a similar peak in the $^{19}F$ MAS NMR spectrum of pure Mo(tfd-$CO_2Me$)$_3$ (a comparable

chemical shift of -56.6 ppm is seen for the neutral dopant in solution ).[18] As is the case in the Mo(tfd-$CO_2Me)_3$ + spiro-OMeTAD sample, the minor feature at approximately -65 ppm is likely due to Mo(tfd-$CO_2Me)_3^-$ monoanions in a more diamagnetic environment, i.e., closer proximity of the monoanion to unreacted dopant, or better separation from other paramagnetic species. These data are consistent with the hypothesis that the Mo-complexes are doping the perovskite at the interface leaving a layer of paramagnetic counterion on the surface.

Time-resolved photoluminescence (PL) measurements were carried out. When exciting at the lowest fluence (0.187 nJ/$cm^2$), we mainly probe trap-assisted, non-radiative recombination since the carrier population is sufficiently low for trap-assisted recombination to be the dominant recombination pathway.[19] In this regime the PL decay can be fit to a monoexponential function in order to extract a lifetime, $\tau$. Fig. 4 shows the PL decays of neat and dopant-treated perovskite films; both exhibit a sharp drop in the PL within the first 10 ns of the decay. This sharp decay was present at both high and low fluences, indicating that is likely due to carrier dilution via diffusion, rather than rapid recombination events.[20] This initial drop was excluded in the fitting parameters. We observe a near continuous decrease in the PL lifetime of the Mo-treated films. This decrease scales with increasing dopant concentration, decreasing by an order of magnitude from 4350 ns in the untreated film to 440 ns in the film treated with 1.0 wt.% of Mo(tfd-$COCF_3)_3$. From the experimental results previously discussed, we can surmise that the perovskite film is doped at the surface, rather than through the entire bulk. Based on this, we expect the surface of the perovskite to become more hole-rich, thereby increasing the degree of recombination within the perovskite film and resulting in the reduced PL lifetime which we observe. This result is consistent with a recent finding by Ramirez et al, who investigated the differing material properties when the perovskite film is deposited onto mesoporous scaffolds, and crystallized on either n-type or p-type substrates.[14] Here, it was observed that when the perovskite was crystallized within a porous scaffold atop a p-type NiO substrate, the electronic character of the perovskite was significantly more p-type. The resulting films exhibited significantly shorter PL lifetimes and electron diffusion lengths, indicating the requirement for a very narrow p-type region.

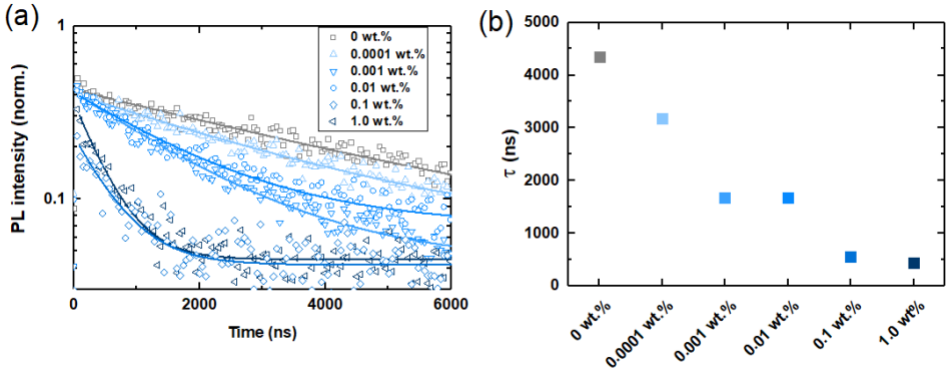


**Fig. 4.** (a) Time-resolved photoluminescence of neat and Mo(tfd-$COCF_3)_3$-treated perovskite films. The data are shown with open symbols and fits are depicted using solid lines of corresponding colour. Samples were excited with a 505 nm laser source at a fluence of 0.187 nJ/$cm^2$. (b) Lifetimes extracted from the fits shown in (a).

The band bending induced by the molecular dopant (Fig 3d) should increase the hole selectivity of the treated perovskite surface. To test this, we incorporate the perovskite layer into a series of devices without selective contacts. A schematic of such a device is shown in Fig. 5a, where the perovskite film is sandwiched between fluorine-doped tin oxide (FTO) and gold electrodes. The

current-voltage (*JV*) characteristics of devices made with treated and untreated films were measured under both dark and illuminated conditions. Fig. 5b shows the dark *J-V* curves for these devices. These curves were fitted to the ideal diode equation, and the reverse saturation current, $J_0$, was extracted (Fig. 5c). As $J_0$ is proportional to the recombination rate, it is a good metric to determine the effect of the dopant-treatment on the interfacial charge recombination. For lower concentrations of the dopant, $J_0$ decreases with increasing doping concentration which indicates that charge recombination is suppressed by the dopant treatment. The lowest $J_0$ is achieved with a dilution of 0.01 wt.% of the dopant. We attribute this behaviour to the increase in the work function (Fig. 2a), and an effective p-doping of this interface. The p-type character of the interface is likely to make the interface more hole-selective i.e. more favourable for hole extraction, whilst in principle repelling photogenerated electrons. Consequently, charges should be more effectively separated at the perovskite-gold interface and fewer will be able to recombine. However, at higher doping concentrations, namely 0.1 wt.% and 1.0 wt.%, the trend is reversed and $J_0$ increases by orders of magnitude with higher doping concentrations, which is indicative of a significant increase in the recombination rate at the interface. This is likely due to the onset of much faster recombination in the p-type region, as the p-type region begins to extend further into the perovskite film, and perhaps down the grain boundaries. It is, therefore, likely that an ideal doping concentration exists, where a small amount of dopant improves the hole selectivity of the contact, but too much doping leads to rapid recombination of minority carriers (electrons) within this doped region. Fig. 5d shows representative *JV* curves, in the dark and under illumination, of both a control device, and a device treated with a 0.01 wt.% solution of $Mo(tfd\text{-}COCF_3)_3$. We note that none of the devices were subjected to pre-biasing in these experiments. From Fig. 5d, we observe that under illumination, the device fabricated from the $Mo(tfd\text{-}COCF_3)_3$-treated perovskite shows significantly improved rectification. This improvement in the diode behaviour is consistent with the notion that the dopant treatment introduces an energetic asymmetry, in the form of a homojunction at the perovskite-gold interface, which enables selective charge extraction in the treated devices.

Having demonstrated that the treatment-induced changes in the hole density at the perovskite surface results in increased charge selectivity of the interface, we proceed to examine the influence of the dopant in a full device with charge-selective layers. To probe this, we use the n-i-p device configuration and employ a matrix of single-walled carbon nanotubes (SWCNTs) and spiro-OMeTAD as the hole-transport layer.[21] From the batch statistics we see that while the short-circuit current density ($J_{SC}$) remains relatively constant up to 0.01 wt.%, both the $V_{OC}$, and the *FF*, increase, resulting in an improvement in the PCE of the devices. At higher dopant concentrations there is a notable decrease in all three parameters. This is likely due to a confluence of factors. At 0.1 wt.% the dopant is very near its solubility limit in chlorobenzene. Hence, when it is deposited onto the surface of the perovskite, in addition to forming agglomerates of unreacted dopant, as was seen in the SEM images, it likely forms a thicker dopant film, a significant portion of which would consist of unreacted dopant. This will act to inhibit charge extraction and cause an increase in surface recombination, thus causing the observed decrease in performance of the solar cells. It is also very likely that at such high doping concentrations, the perovskite film becomes too strongly p-type, and the vastly reduced carrier diffusion lengths begin to negatively affect charge extraction in a planar heterojunction device structure. We show the *JV* characteristics of the best performing control and Mo-treated devices in Fig. 6 and give their performance parameters in Table 1.

**Table 1.** Champion and average device performance parameters for solar cells fabricated from untreated and Mo(tfd-$COCF_3)_3$-treated perovskite films

| | $J_{SC}$ (mA/cm$^2$) | $V_{OC}$ (V) | FF | PCE (%) | $PCE_{MPP}$ (%) |
|---|---|---|---|---|---|
| Untreated (champion) | 22.9 | 1.16 | 0.74 | 19.7 | 19.0 |
| Untreated (average) | 22.9 ± 0.3 | 1.15 ± 0.01 | 0.72 ± 0.03 | 18.8 ± 0.7 | |
| Mo(tfd-$COCF_3)_3$-treated (champion) | 22.7 | 1.18 | 0.79 | 21.2 | 20.9 |
| Mo(tfd-$COCF_3)_3$-treated (average) | 22.6 ± 0.4 | 1.18 ± 0.01 | 0.79 ± 0.02 | 20.2 ± 0.7 | |

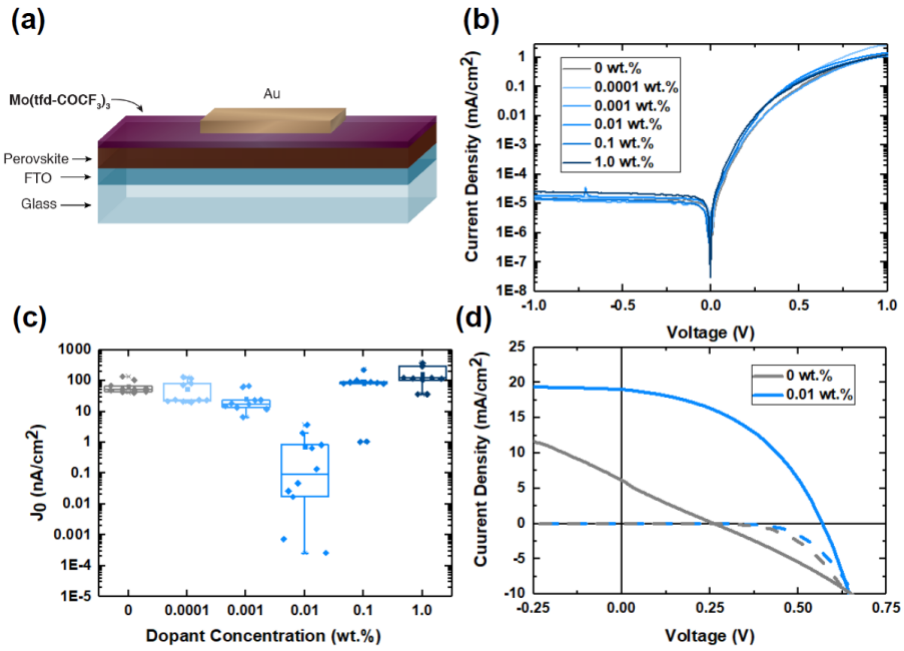


**Fig. 5.** Dark current-voltage (J-V) characteristics of contactless perovskite devices. (a) Schematic of perovskite device fabricated without charge-selective contacts. (b) Dark J-V characteristics of control and Mo(tfd-$COCF_3)_3$-treated devices. (c) Dependence of the reverse saturation current, $J_0$, on the concentration of Mo(tfd-$COCF_3)_3$ used to treat the perovskite surface. (d) Representative J-V curves (in the dark and under illumination) of a control and Mo(tfd-$COCF_3)_3$ treated device.

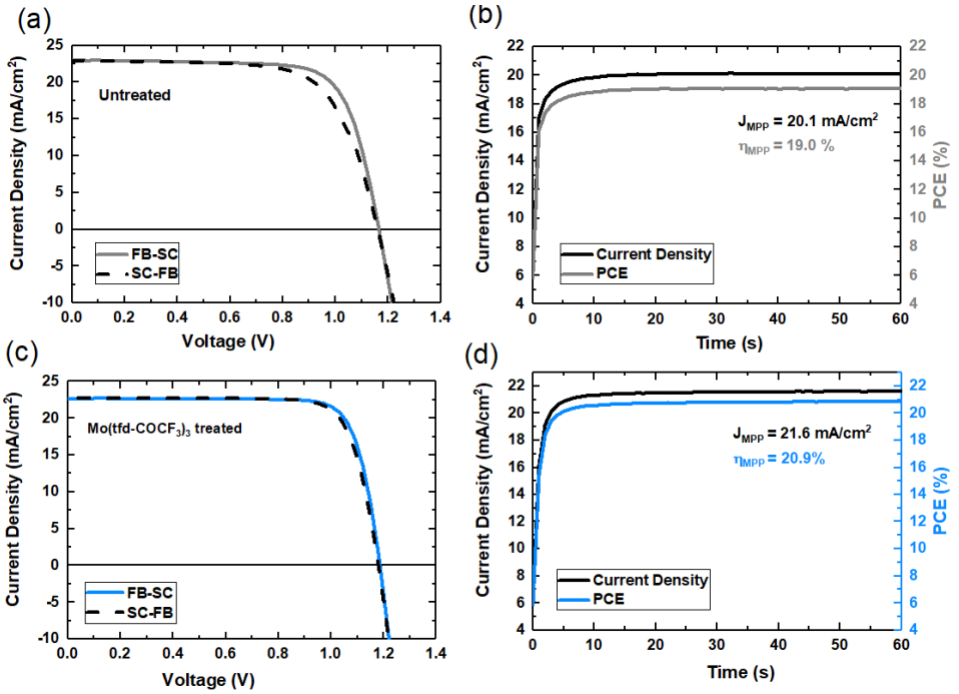


**Fig. 6.** (a) and (c) Current-voltage characteristics under 1 sun simulated AM1.5G solar illumination of the best performing treated and untreated solar cells respectively. (b) and (d) Steady-state current density and efficiency of devices shown in (a) and (c). Measurements were taken by holding the respective devices at their maximum power point (MPP) voltages for 60 s.

From the data shown in Fig. 6 and Table 1, we see that treating the perovskite surface with Mo(tfd-$COCF_3)_3$ causes a significant increase in both the $V_{OC}$ and *FF* of the solar cells. This is indicative of a reduction in recombination, and enhanced charge extraction at the p-type interface. Along with the enhancements in $V_{OC}$ and *FF*, the Mo(tfd-$COCF_3)_3$ devices also exhibit suppressed hysteresis and higher steady-state efficiencies, a result often observed through improving the interfaces in perovskite-based solar cells, thus allowing for more efficient charge extraction.[22] Common examples of this involve surface passivation of the perovskite or modification of the charge collection layers in the device.[23-25] We have previously shown that $Mo(dt)_3$ complexes can be used as dopants for spiro-OMeTAD, enabling the fabrication of efficient perovskite solar cells.[13] To exclude the possibility that the observed improvements in device performance are due to the doping of the HTM by Mo(tfd-$COCF_3)_3$, we also prepare devices where the spiro-OMeTAD was oxidised in solution prior to deposition; even in this case there is a similar improvement in the steady-state device performance when the perovskite surface is treated with Mo(tfd-$COCF_3)_3$, thus ruling out an increase in HTM conductivity as being the underlying cause for the enhancement in device efficiency.

In previous work, we have shown that *t*BP directly interacts with the perovskite layer and causes a 'p-doping' of the perovskite/HTM interface through the formation of a charge accumulation layer.[9] This causes upward band bending and allows for more efficient hole extraction and thus, reduced interfacial recombination and improved steady state efficiencies. We propose a similar effect with the introduction of the Mo(tfd-$COCF_3)_3$ layer, where directly p-doping the perovskite surface results in upward band bending and thus, in enhanced charge extraction at the p-type interface. If both the Mo(tfd-$COCF_3)_3$ and *t*BP serve the same function, it stands to reason that by

surface doping the perovskite with Mo(tfd-$COCF_3$)$_3$ we could obviate the need for *t*BP in spiro-OMeTAD based devices. It is important to note here, that *t*BP may have an additional role in adjusting the pH of the spiro-OMeTAD solution such that the conventional Li-TFSI dopant remains solubilised. Here, since we rely on SWCNTs for rapid charge extraction, we forgo the need for a dopant in spiro-OMeTAD and can thus isolate the role of *t*BP as an interfacial modifier.

To test this hypothesis, we fabricate devices with and without *t*BP. We show the *JV* characteristics and steady-state efficiencies in Fig. 7. The comparison of devices with and without *t*BP confirms previous observations that the presence of *t*BP significantly improves the device performance by enhancing $V_{OC}$ and *FF*, and, most notably, the steady-state efficiency. Remarkably, however, *t*BP-free devices, made with perovskite films that were treated with Mo(tfd-$COCF_3$)$_3$, outperform the control device, which was fabricated with *t*BP, achieving a steady-state efficiency of 20.4%. This strongly corroborates our hypothesis that deliberate, controlled p-doping with Mo(tfd-$COCF_3$)$_3$ has a similar effect to that of *t*BP on device performance in perovskite solar cells. In addition, recent studies have discussed the detrimental effects of *t*BP on the long-term stability of perovskite solar cells.[10-12] We propose surface doping of the perovskite material with molecules such as Mo(tfd-$COCF_3$)$_3$ as a means to improve charge extraction, and hence device performance of perovskite solar cells, without the potentially harmful long-term effects of *t*BP. Indeed, preliminary stability tests show improved performance of Mo(tfd-$COCF_3$)$_3$ treated devices after > 800 hr thermal stressing at 85 °C in the dark, with *t*BP-free devices outperforming devices fabricated with *t*BP. These results indicated that interface doping is a promising route to further improving both the efficiency and stability of perovskite-based photovoltaics.

In summary, we have investigated the interaction between the mixed-cation, mixed-halide perovskite, $FA_{0.85}MA_{0.15}Pb(I_{0.85}Br_{0.15})_3$, and a strongly electron-withdrawing dopant, Mo(tfd-$COCF_3$)$_3$. We find that treating the surface of the perovskite film with a dilute solution of this dopant results in a downward shift in the work function, an increase in the dark conductivity, and a decrease in the photoluminescence lifetime of the perovskite film, indicating an increase in the hole density at the perovskite interface. XPS and UPS measurements confirm the shift of the Fermi level in the perovskite, while solid-state NMR spectroscopy shows the formation of the Mo(dt)$_3$ monoanion, indicating that when the dopant is in contact with the perovskite, an electron-transfer reaction occurs between the perovskite and the Mo(dt)$_3$ complexes. By incorporating the Mo(tfd-$COCF_3$)$_3$-treated films into solar cells we obtain improved charge extraction at the p-type interface, resulting in devices with steady-state efficiencies approaching 21%. Additionally, we find that by using this dopant to p-dope the perovskite surface, we obviate the need for *t*BP, resulting in improved thermal stability of perovskite solar cell. Thus, we have established a method of extrinsically doping the perovskite material and have shown the application of interfacial doping to perovskite devices, providing a potential avenue for highly efficient perovskite photovoltaics with improved long-term stability. The work on surface p-doping been published (#3 in section V.1).[26]

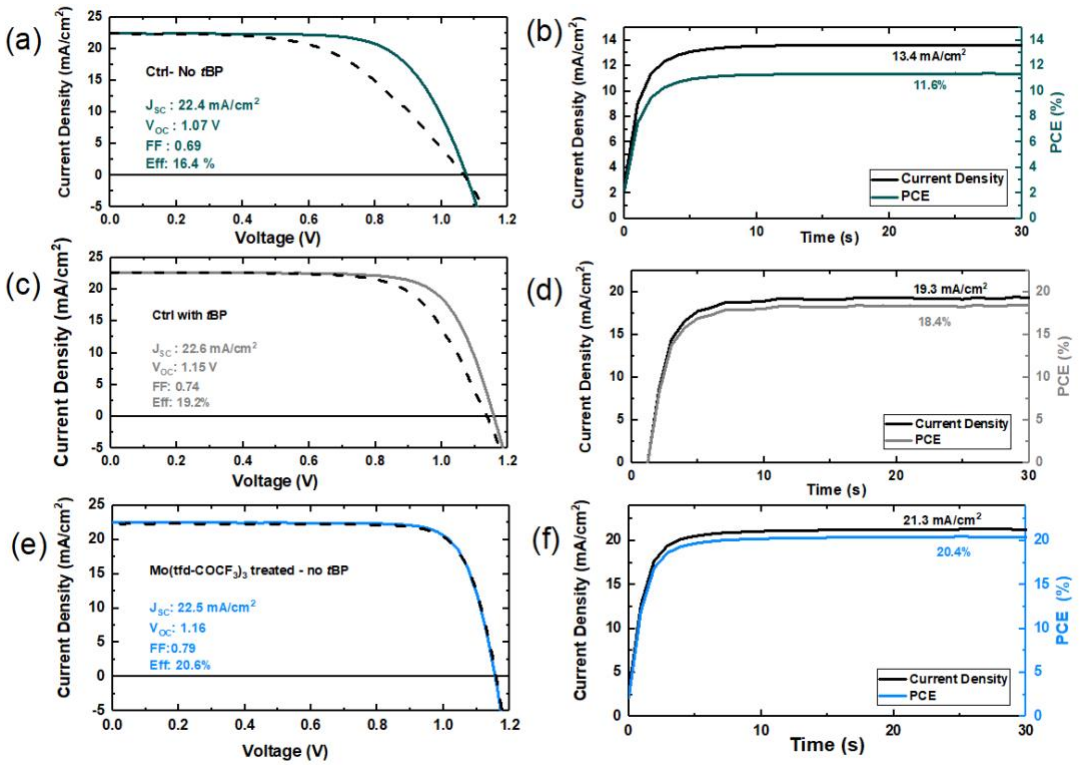


**Fig. 7.** Current-voltage characteristics and steady-state efficiencies of perovskite solar cells fabricated with (a) and (b) SWNTs and spiro-OMeTAD, (c) and (d) SWNTs, spiro-OMeTAD and *t*BP, (e) and (f) Mo(tfd-$COCF_3$)$_3$, SWNTs and spiro-OMeTAD (no *t*BP).

We have extended this work to n-doping of perovskite surfaces may be carried out; in particular, solid-state magic-angle spinning $^2$H NMR studies of microcrystalline perovskite treated with deuterated (RuCp*mes)$_2$ indicate the presence of monomeric RuCp*mes$^+$, which is the expected product if the dimer does indeed n-doped the perovskite. However, we found no improvement in the electrical properties of devices incorporating such surface doped material, and have not continued to work on surface doping.

In addition to investigations of redox doping of perovskite surfaces, this grant also partly supported a collaboration with David Ginger (U WA) and Carlos Silva (GT), primarily supported by the DoE, on the use of excitation correlation spectroscopy to investigate the role of the passivating agent, APTMS ($NH_2(CH_2)_3Si(OMe)_3$), in passivating a $FA_{0.83}Cs_{0.17}Pb(I_{0.85}Br_{0.15})_3$ surface. The work indicates carrier trapping on a sub-ns timescale and that APTMS passivates both deep and shallow traps. It has now been published (#12 in section V.1).[27]

## IV.2. Hole-Transport Materials for Perovskite Solar Cells

Our overall approach to hole-transport materials (HTMs) is based on copolymers of monomers with pendant HTM moieties and that may also include monomers with pendant crosslinking groups. The approach is modular in that the properties of the polymer can be adjusted through varying the HTM:crosslinker ratio, the ionization energy (IE) of the polymer can be varied through

the substitution pattern of the HTM monomer, and other properties can be varied through the choice of the polymer backbone.

*ROMP-Based Polymers with or without Cinnamate Crosslinking Groups.*

As described in the final report for our previous grant (FA9550-15-1-0115) our first crosslinkable HTM (Fig. 8) was designed to have a similar chemical structure and ionization energy to spiro-OMeTAD (Fig. 1), which is one of the most widely used HTMs in n-i-p PSCs. Indeed, electrochemical estimates of IE are ca. 4.8 eV for both materials.

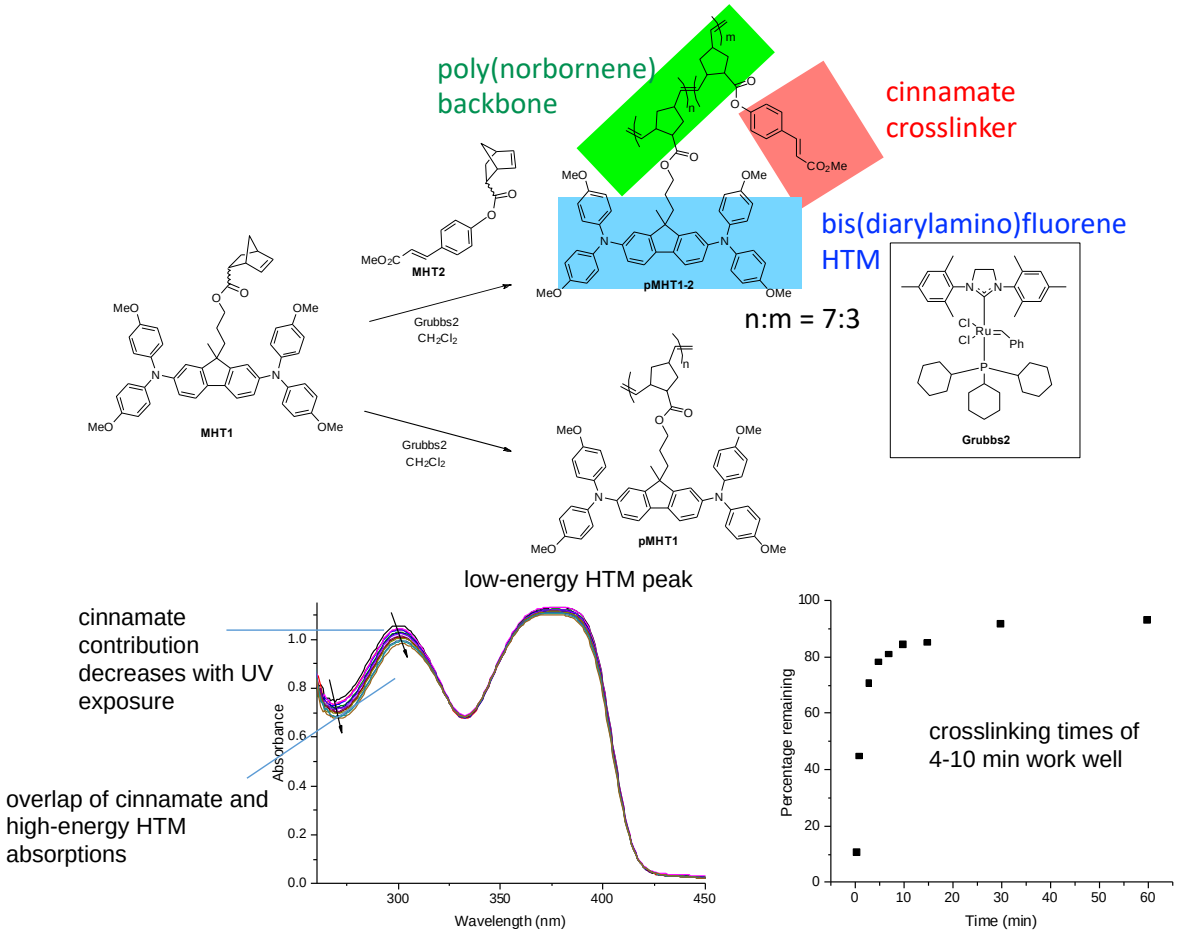


**Fig. 8.** Top: synthesis of a UV-crosslinkable norbornene HTM, **pMHT1-2**, along with that of the corresponding non-crosslinkable homopolymer, **pMHT1** (synthesis of monomer, **MHT1**, not shown). The top left inset shows the 2+2 dimerization of the cinnamate moieties on which the UV crosslinking relies, while that on the right shows the structure of the ruthenium initiator used in the polymerization. Bottom: UV-vis. spectrum of a film of **pMHT1-2** showing the decrease in the cinnamate peak with UV (356 nm) exposure, while the amine-based peaks remain unchanged, and graph showing increasing resistance of films to solvent with increased UV exposure.

We have used this material in both n-i-p cells, doped with Mo(tfd-$COCF_3$)$_3$ (see Fig. 1, above) in which PCE values compare well to spiro-OMeTAD devices (Fig. 9). However, both types of cell exhibit strong hysteresis, something which seems to be a general feature when using Mo(tfd-$COCF_3$)$_3$-doped HTMs in n-i-p cells. We also fabricated p-i-n cells in which we compared the ROMP polymer to PolyTPD (Fig. 10), which is widely used in p-i-n architectures, achieving a record of 19.1% PCE. However, the ROMP polymer performed significantly more poorly than the

reference material. We then shifted to our attention in this context to a side-chain polymer with an IE better matched to that of PolyTPD (see following sub-section).

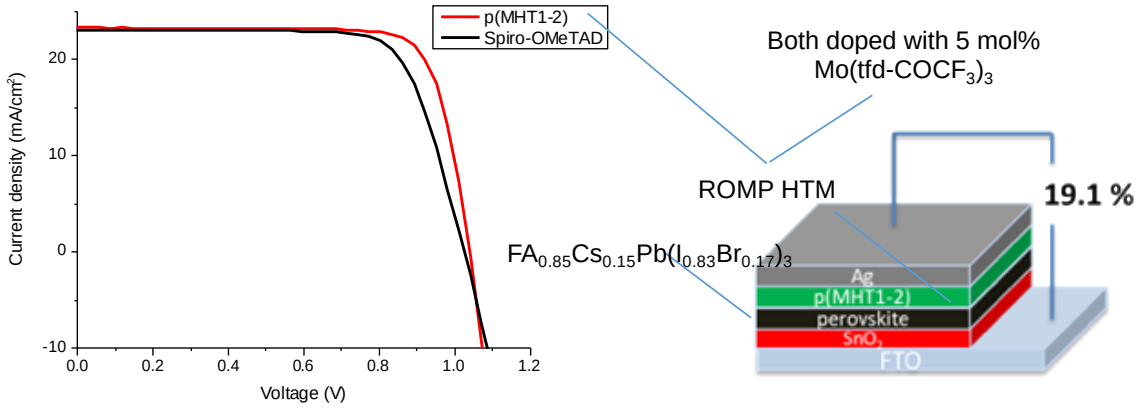


| HTM | $J_{sc}$ (mA/cm²) | PCE (%) | $V_{oc}$ (V) | FF |
|---|---|---|---|---|
| **ROMP HTM** | 23.20 | 19.08 | 1.04 | 0.79 |
| **Spiro-OMeTAD** | 22.99 | 17.50 | 1.01 | 0.75 |
| **Spiro-OMeTAD (literature*)** | 21.98 | 17.20 | 1.06 | 0.74 |

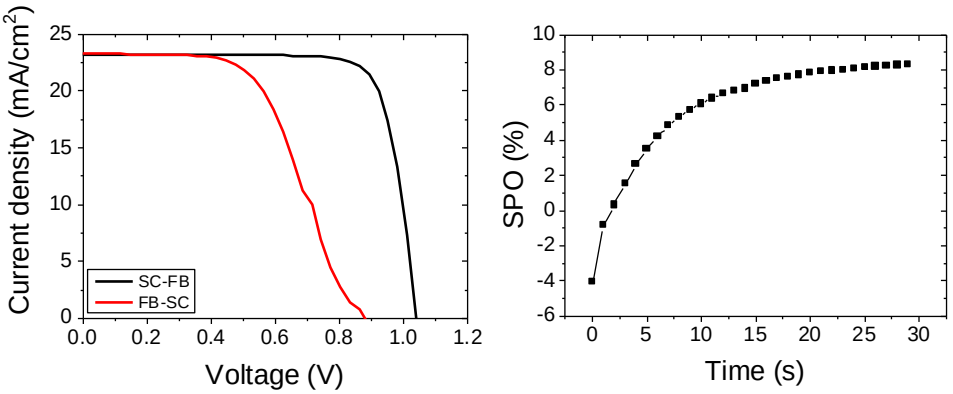


**Fig. 9.** Top: comparison of J-V curves for PSCs with spiro-OMeTAD and ROMP crosslinked polymers (Fig. 8) as HTMs (device structures as shown on the right). Center: device performance (literature data from ref. 13, using PCBM interlayer between the $SnO_2$ and perovskite). Bottom: hysteresis behavior of the devices with the ROMP HTM (FB = forward bias; SC = short circuit).

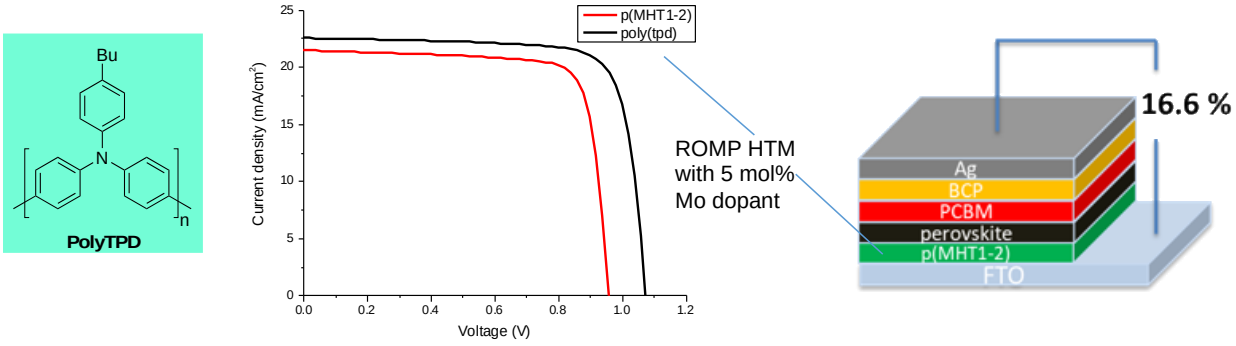


| HTM | $J_{sc}$ (mA/cm²) | PCE (%) | $V_{oc}$ (V) | FF |
|---|---|---|---|---|
| ROMP HTM | 21.47 | 16.59 | 0.96 | 0.80 |
| Poly(tpd) | 22.51 | 19.30 | 1.08 | 0.78 |

**Fig 10.** Top left: structure of PolyTPD. Center top: comparison of J-V curves for p-i-n devices (structure shown on the right) using PolyTPD and **p(MHT1-2)** as HTMs. Bottom: table comparisng performance.

Subsequently, we returned to the **pMHT1** system to examine whether hysteresis can be avoided by using alternative dopants. For simplicity we have carried out these studies using the **pMHT1** homopolymer, rather than its crosslinked version, **pMHT1-2**. We chose to examine Li-TFSI and 4-*tert*-butylpyridine as a potential dopant system for **pMHT1** since these, in combination with air exposure, are often used to p-dope spiro-OMeTAD, as well as Mo(tfd-$COCF_3$)$_3$. As expected from the similar redox potentials for spiro-OMeTAD and **pMHT1**, optical absorption measurements upon addition of Li-TFSI/tBP or Mo(tfd-$COCF_3$)$_3$ to a solution containing **pMHT1** (see Fig. 11) show the growth of new peaks consistent with a bis(diarylamino)fluorene radical cation.

To investigate the effect of Li-TFSI/tBP-doped **pMHT1** and spiro-OMeTAD on perovskite stability, films of the HTMs were spin-coated on top of $Cs_{0.05}FA_{0.95}Pb(I_{0.83}Br_{0.17})_3$ on clean glass; both samples showed similar PL quenching (PLQE = 0.02 in each case) compared to that of the bare perovskite film (PLQE = 0.28) suggesting comparable losses due to non-radiative recombination at the perovskite/HTM interface, likely related to their similar structures and optical properties. Deposition of some molecules with Lewis basic substituents on top of the perovskite has been suggested to passivate defects.[28-31] Several studies, including ours, have found ester-containing materials can play a useful role in perovskite growth and/or passivation. The added ester moieties on the polymer could potentially bind to any undercoordinated lead ions at the surface, effectively screening the charge and reducing recombination. Photoluminescence (PL) lifetime experiments on films of perovskite in contact with doped **pMHT1** or spiro-OMeTAD (see Fig. 12) are consistent with this idea; the former exhibit longer lifetimes associated with bimolecular recombination. Moreover, the PL peak of the **pMHT1**-containing film is blue-shifted compared to the spiro-OMeTAD one, which also suggests that there is passivation of trap states at the interface between the HTM and perovskite layers.

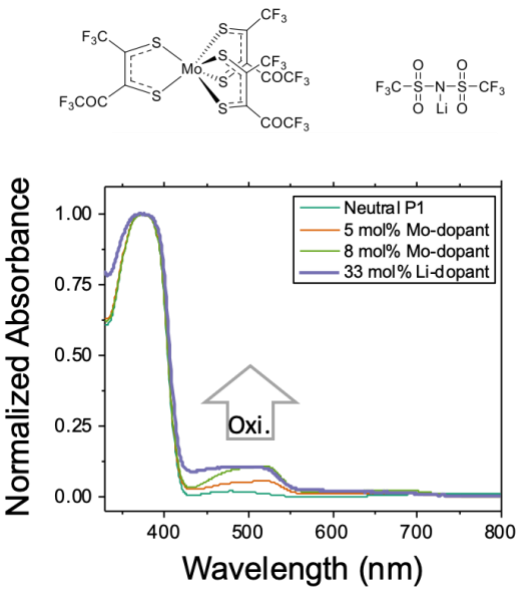


**Fig. 11.** Chemical structure of Mo(tfd-$COCF_3$)$_3$ and Li-TFSI. Doping of **pMHT1** (**P1** in the legend) with Mo(tfd-$COCF_3$)$_3$ (taken at t = 0 h) and Li-TFSI/tBP (taken after 24 h air exposure) in $CH_2Cl_2$. The weak absorption seen between 600 and 700 nm for the Mo(tfd-$COCF_3$)$_3$-doped samples is attributable to Mo(tfd-$COCF_3$)$_3^-$.[32]

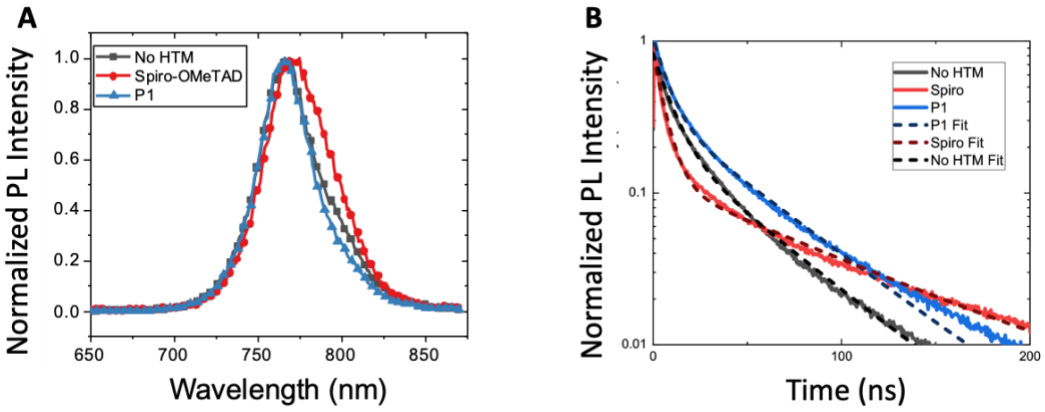


**Fig. 12.** (A) Photoluminescence of glass/perovskite/HTM half devices. The PL maximum for the spiro-OMeTAD sample is slightly red-shifted relative to that of the MHTP1 (here labeled **P1)** and the bare perovskite sample, which may indicate more band-bending due to shallow-trap formation in the spiro-OMeTAD case.[7,8] (B) Fitting of the time-resolved PL of the glass/perovskite/HTM half devices.

In addition to possibly passivating the perovskite, it was hypothesized that the polymer could also better protect the perovskite from extrinsic factors (such as moisture or oxygen penetration) compared to the small spiro-OMeTAD molecule.[33, 34] In order to probe if the polymer **pMHT1** could improve the stability of the solar cells, we fabricated half-cells with the architecture FTO/$Cs_{0.05}FA_{0.95}Pb(I_{0.83}Br_{0.17})_3$/HTMs (undoped) and heated them in an aging box (conditions: 85 °C, 76 mW cm$^{-2}$, 50% relative humidity). We measured the PXRD of the half-cells over time by periodically moving the films to ambient conditions for the time of measurement (see Fig. 13A-B). After 20 h, the bare perovskite film no longer shows the (110) peak of the 3D perovskite at ~14°, while the **pMHT1**- and spiro-OMeTAD-coated films retained 50% and 25% of the peak intensity respectively, clearly showing the advantage of using the polymeric material. We also followed the decomposition of the perovskite by UV-vis spectroscopy (see Fig. 4C-D). After 48h in the aging box, the spiro-OMeTAD-coated film turned gray and no longer showed a discernable

onset of absorption at the perovskite band gap at ~775 nm, while for the **pMHT1** containing film, this feature was still observable.

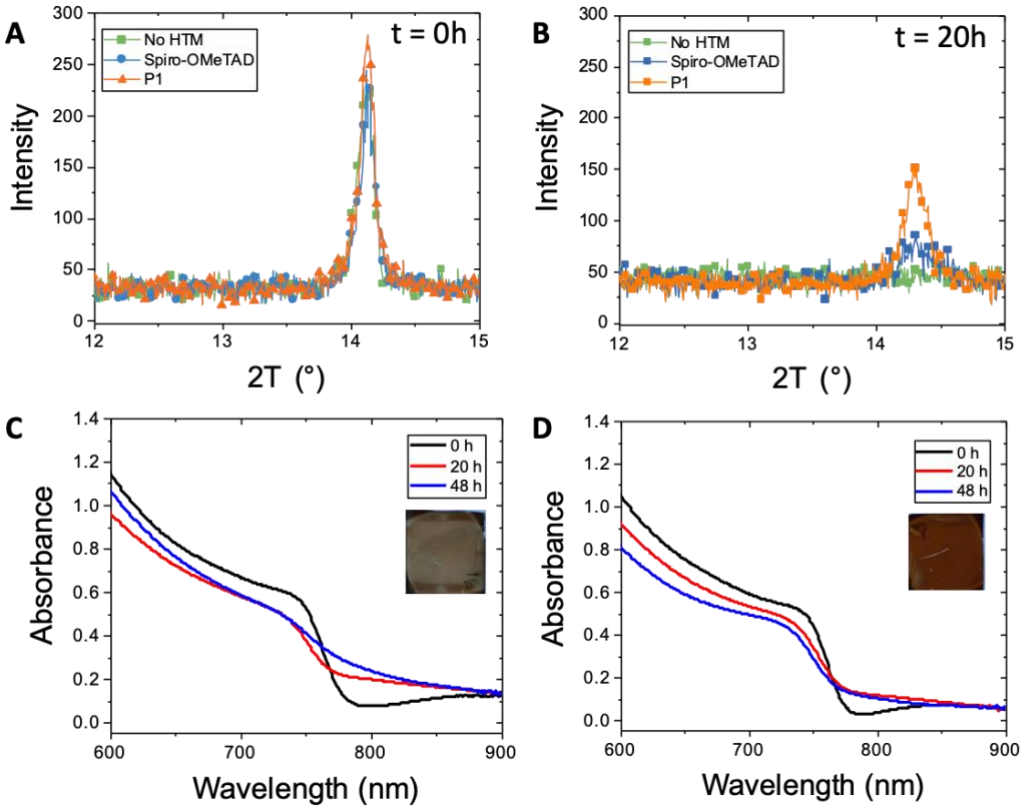


**Fig. 13.** Stability study of the glass/perovskite/HTM half devices. PXRD of the films without thermal stress (A) and after 20 h in an aging box (conditions: 85 °C, 76 mW $cm^{-2}$, 50% relative humidity) (B). Absorption spectra after various times under stress in the aging box for samples with (C) spiro-OMeTAD and (D) **pMHT1** as the HTM. Insets: photographs of the films after 48 h in the aging box.

We investigated the performance of the new HTM **pMHT1** in n-i-p PSCs using the following architecture; FTO/$SnO_2$/$FA_{0.85}Cs_{0.15}Pb(I_{0.83}Br_{0.17})_3$/PEA-I/p-doped HTM/Ag, where FTO = fluorine-doped tin oxide, FA = formamidinium, HTM is spiro-OMeTAD or **pMHT1** and PEA-I is phenylethylammonium iodide, a known passivating agent.[35] The devices using p-optimally doped P1 are reported in Fig. 14 and Table 1. We obtained a champion PCE of 15.5% for Li-TFSI-doped devices, which is similar to that for the control devices with doped spiro-OMeTAD (16.5%) (see Table S2). The current density−voltage (J−V) characteristics of the best performing devices using Li-TFSI-doped spiro-OMeTAD and **pMHT1** recorded under simulated AM1.5, 1 sun irradiance are presented in Fig. 14. As it can be seen from **Error! Reference source not found.**, **pMHT1** and spiro-OMeTAD have similar performance with the averaged performance of **pMHT1** being slightly higher compared to spiro-OMeTAD. The reduced spread in the data also shows improved reproducibility over spiro-OMeTAD, which has previously been shown to form films with poor uniformity.[31] Furthermore, the improved thermal and atmospheric stability of half devices with P1 suggests that the lifetime power output for devices based on **pMHT1** may be greater than those with spiro-OMeTAD.

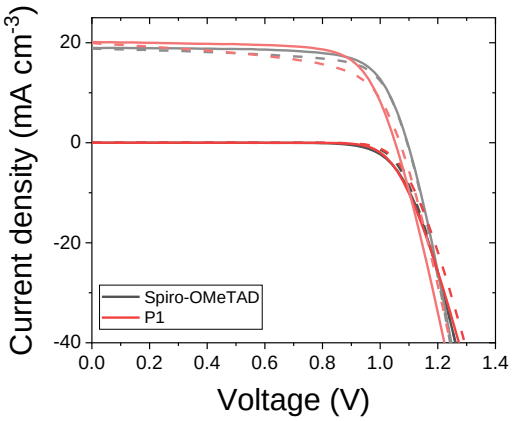


**Fig. 14.** Comparison of the JV curves of the champion cells obtained for Li-TFSI-doped **pMHT1** (**P1** in the legend) and spiro-OMeTAD HTMs under 1 sun and in the dark.

**Table 1.** Basic parameters for the champion n-i-p cell prepared with the two HTMs p-doped using Li-TFSI and tBP.

| HTM | | PCE (%) | $J_{sc}$ (mA cm$^{-2}$) | $V_{oc}$ (V) | FF |
|---|---|---|---|---|---|
| Spiro-OMeTAD | Average | 14 ± 2 | 18 ± 1 | 1.06 ± 0.02 | 0.69 ± 0.03 |
| | Maximum | 16.5 | 19.8 | 1.10 | 0.75 |
| **pMHT1** | Average | 14.6 ± 0.9 | 19.3 ± 0.8 | 1.05 ± 0.01 | 0.71 ± 0.02 |
| | Maximum | 15.5 | 20.1 | 1.06 | 0.73 |

Using spiro-OMeTAD ca. 1.5x more material (85 mg mL$^{-1}$ vs. 55 mg mL$^{-1}$ for **pMHT1**) is needed to obtain similar photovoltaic performance. The thickness of an optimal **pMHT1** layer was approximately half that of an optimal spiro-OMeTAD layer (~100 nm vs. 200 nm as determined by profilometry). Both **pMHT1** and spiro-OMeTAD films have visible "comets", as is typical for spiro-OMeTAD films. Careful optimization of Li-TFSI and tBP helps to decrease the density of pinholes and to reach optimal device performance. For **pMHT1**the optimal Li-TFSI dopant concentration is 25 mol%, while that for spiro-OMeTAD is 50 mol%, which in both cases corresponding to oxidation of half of the bis(diarylamino)fluorene units.

In summary, we have described the use of a polymeric HTM analogue to spiro-OMeTAD in n-i-p PSCs. PCEs using **pMHT1** are as high as 15.5% similar to those obtained using the widely used HTM spiro-OMeTAD in analogous devices. Half-device stability under harsh conditions is also significantly improved when using **pMHT1**. Some aspects of the work on the homopolymer have now been published (#10 in section V.1).[36]

*Acrylate Hole-Transport Polymers with Cinnamate Crosslining Groups*

As a crosslinked side-chain polymer to be used in lieu of PolyTPD (5.2 eV) a higher IE is needed than that of **p(MHT1-2)** (4.8 eV). We chose the crosslinkable polymer **P1-2** (Fig. 15), a material that we have previously used as an HTM in multilayer organic light-emitting diodes and for which (based on the electrochemistry of the monomer) an IE of 5.1 eV is estimated. This higher IE is due to the absence of electron-donating methoxy substituents and to the presence of a non-planar biphenyl, rather than planar fluorene, bridge between the two diarylamino groups. The polymer

also differs in the use of an acrylate, rather than norbornene, polymerizable group. Like **P(MHT1-2)**, however, it is easily photocrosslinkable (to give **CL1-2**) by virtue of incorporation of cinnamate monomers. From the point of view of PSC fabrication, this facile photocrosslinking is potentially advantageous over alternative thermal crosslinker approaches that require high temperatures >150 °C since the process can be done at ambient temperature on plastic substrates. Moreover, for n-i-p structures, the low power UV-lamp used would not degrade the underlying perovskite layer, whereas the temperatures required for many thermal crosslinking reactions would. **P1-2** has a slightly higher energy onset of optical absorption than PolyTPD (Fig. 15), which is potentially advantageous in allowing more of the solar spectrum to reach the active layer, potentially reducing parasitic absorption and maximizing current density. Addition of the p-dopant $F_4$-TCNQ to solutions of either PolyTPD or **P1-2** leads to only moderate changes in the optical spectra, suggesting inefficient doping with this oxidant. This is further illustrated by Fig. 15, where the effects of successive dopant addition are shown for the case of **P1-2**. The low yield of oxidized HTM in each case is expected given the oxidation and reduction potentials of **P1-2** and $F_4$TCNQ, respectively (+0.26 V and +0.15 V in the $CH_2Cl_2$/0.1 M $Bu_4NPF_6$).

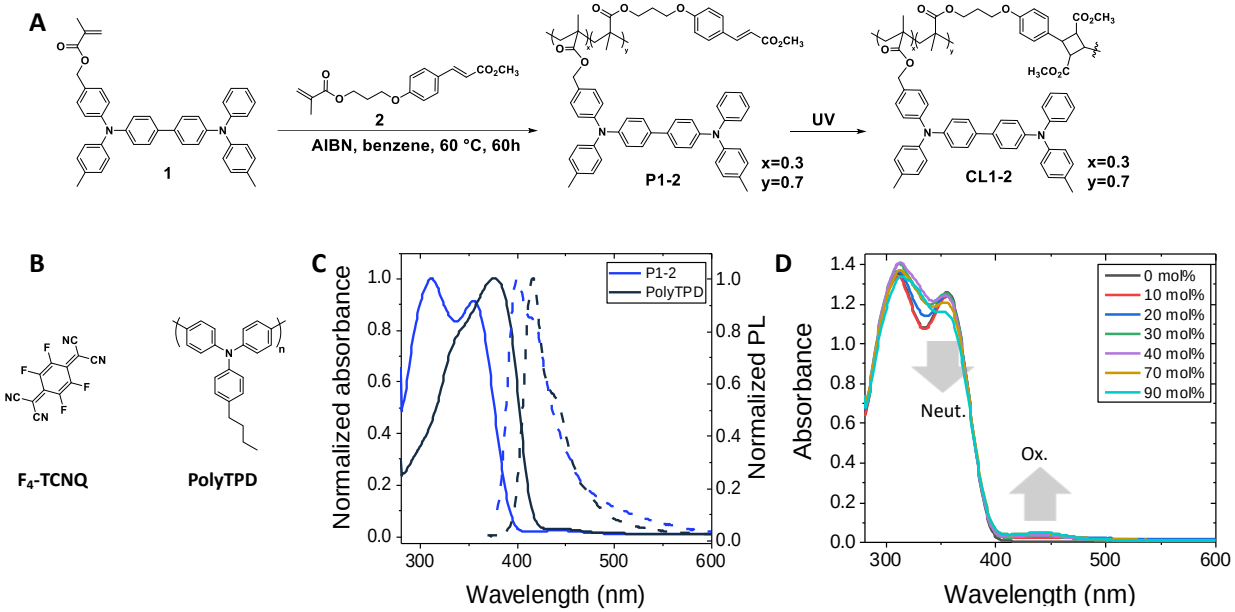


**Fig. 15** (A) Synthesis of copolymer **P1-2** from the bis(triarylamine) **1** and the cinnamate **2**. The crosslinked material **CL1-2** can be obtained after illumination with UV light. (B) Chemical structure of PolyTPD and $F_4$-TCNQ, the dopant usually used to dope triarylamine-based HTMs. (C) Comparison of the absorbance (solid line) and photoluminescence (dashed line) spectra of **P1-2** and PolyTPD in toluene (with 20 mol% $F_4$-TCNQ per triarylamine unit). (D) UV-vis spectrum showing the doping in toluene solution of **P1-2** with $F_4$-TCNQ (where Neut. and Ox. indicate signals attributable to the neutral and oxidized bis(diarylamino)biphenyl units, respectively, and *x* mol% is relative to the number of triarylamine units, i.e. corresonds 2*x* molar equivalents per 100 moles of monomer).

Atomic force microscopy of thin films of **CL1-2** and PolyTPD on glass substrates showed similar homogeneity and smoothness. Perovskite films crystallized on top of the two HTM films on FTO substrates also appeared similar by scanning electron microscopy (SEM), although we observed a larger distribution of bright color grains on the **CL1-2** film than on PolyTPD; it is unclear what the cause of this observation is, or whether it has any device consequence, although excess $PbI_2$ has been found to be beneficial in previous PSC studies. The powder X-ray diffraction (PXRD) of the perovskite films on top of the two different HTMs are also similar, indicating comparable perovskite growth on both material when FTO is used as the substrate.

The conductivity of the HTMs was characterized using four-point probe measurements with and without $F_4$-TCNQ. Slightly lower conductivity was measured for pristine PolyTPD compared to pristine **CL1-2** (see Fig. 16) after annealing at 130 °C (the temperature at which the HTMs were annealed). In both cases, doping the HTM with $F_4$-TCNQ p-dopant increased the conductivity of the HTM by similar amounts; however, as discussed in the following section, PSC device performance was comparable for undoped and doped **CL1-2,** while the performance increased upon doping of PolyTPD (see device data later). Although the active layers of the PSCs fabricated in this work (see below) are annealed at only 100 °C, some perovskite materials necessitate high annealing temperature (e.g., often >200 °C for inorganic $CsPbX_3$ perovskites). Accordingly, we also investigated the effect of higher temperatures on both doped **CL1-2** and doped uncrosslinked **P1-2**. After annealing at 180 °C, the doped **CL1-2** conductivity was found to be higher than that of doped uncrosslinked **P1-2**, which is consistent with crosslinking perhaps helping to retain the volatile $F_4$-TCNQ within the film. When films were further annealed at 250 °C, the conductivity of **CL1-2** actually increased, while the integrity of the PolyTPD film was damaged, and the conductivity of PolyTPD decreased dramatically, perhaps due to film damage occurring above the $T_g$ of the latter polymer. This enhanced dopant retention of doped **CL1-2** may, therefore, make it a suitable HTM for PSCs in which subsequently deposited layers require high annealing temperatures.

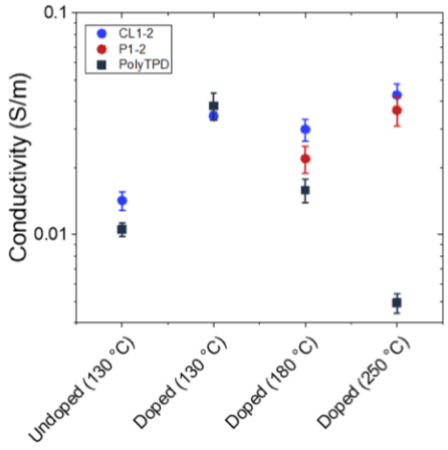


**Fig. 16.** 4-point probe conductivity measurement of PolyTPD and **P1-2/CL1-2**. Films are 10 nm thick. The samples are first annealed 130 °C, which correspond to the processing temperature in the solar cells, and further annealed at the indicated temperature for 10 min. The HTMs are both doped with 20 mol% $F_4$-TCNQ in solution prior to film deposition

To investigate the charge transfer at the perovskite and the HTM interface, we performed steady-state PL measurements. The doped **CL1-2** showed similar PL quantum yield quenching compared to that of PolyTPD, indicating comparable hole-extraction capability of both HTMs at the perovskite/HTM interface, but different PL lifetimes (see below). The photovoltaic performance of **CL1-2** and PolyTPD as HTMs in PSCs was compared using the architecture: FTO/HTM/$Cs_{0.05}(FA_{0.85}MA_{0.15})_{0.95}Pb(I_{0.9}Br_{0.1})_3$/PCBM/BCP/Ag (or Cr/Au for thermal stability tests), where FTO = fluorine-doped tin oxide, MA = methylammonium, FA = formamidinium, PCBM = phenyl-$C_{61}$-butyric acid methyl ester, and BCP = bathocuproine. The two HTM layers had approximately the same thickness (~6-8 nm as determined by profilometry). Both pristine and doped **CL1-2** showed similar performance to PolyTPD. The current-density-voltage (J–V)

characteristics were measured under a simulated AM 1.5G (100 mW $cm^{-2}$) sunlight (see Fig. 17). Only a slight improvement was noticed when **CL1-2** was doped using $F_4$-TCNQ, while a significant improvement was obtained for PolyTPD devices. The devices using undoped **CL1-2** in its optimal condition, shows a PCE of (16±2)%, which is similar to the control device with doped PolyTPD ((16±2)%). The cells presented here also exhibit minimal hysteresis. The SPO provides a more complete view of solar cell performance under operating conditions and avoids the ambiguities associated with JV hysteresis. **CL1-2** achieves 18.7% SPO, matching its scanned efficiency, while PolyTPD achieves 17.7% and exhibits a transient decay. Typically, when SPO is lower than scanned efficiency it is related to hysteresis induced by ion migration and unbalanced charge extraction rates at selective contacts, yet with doped PolyTPD we observe SPO decay without accompanying J-V hysteresis. This behavior may be related to a photo instability, such as the evolution of photo-induced trap states, rather than to mobile ions and unbalanced charge extraction. In such a case, a J-V scan collected over a few seconds may not reflect the longer term SPO. This possibility is consistent with photoluminescence quantum efficiency for half devices (FTO/PolyTPD/perovskite), collected at comparable time scales to the SPO, and the intermediate term UV stability of full devices. Both measurements reflect an illumination- and time-dependent decay similar to that observed in the SPO, as discussed further in the device stability section. The performance of the cells over time is consistent with the trend seen on the J-V curves. Despite the longer wavelength onset of absorption seen for PolyTPD, all devices gave similar external quantum efficiency (EQE) spectra, which is consistent with the similar $J_{sc}$ measured in the J-V scans. Moreover, PSCs made with $FA_{0.83}Cs_{0.17}PbI_{0.83}Br_{0.17}$ also showed comparable performance with **CL1-2** and PolyTPD, showing that this HTM also performs well with this more stable double-cation perovskite

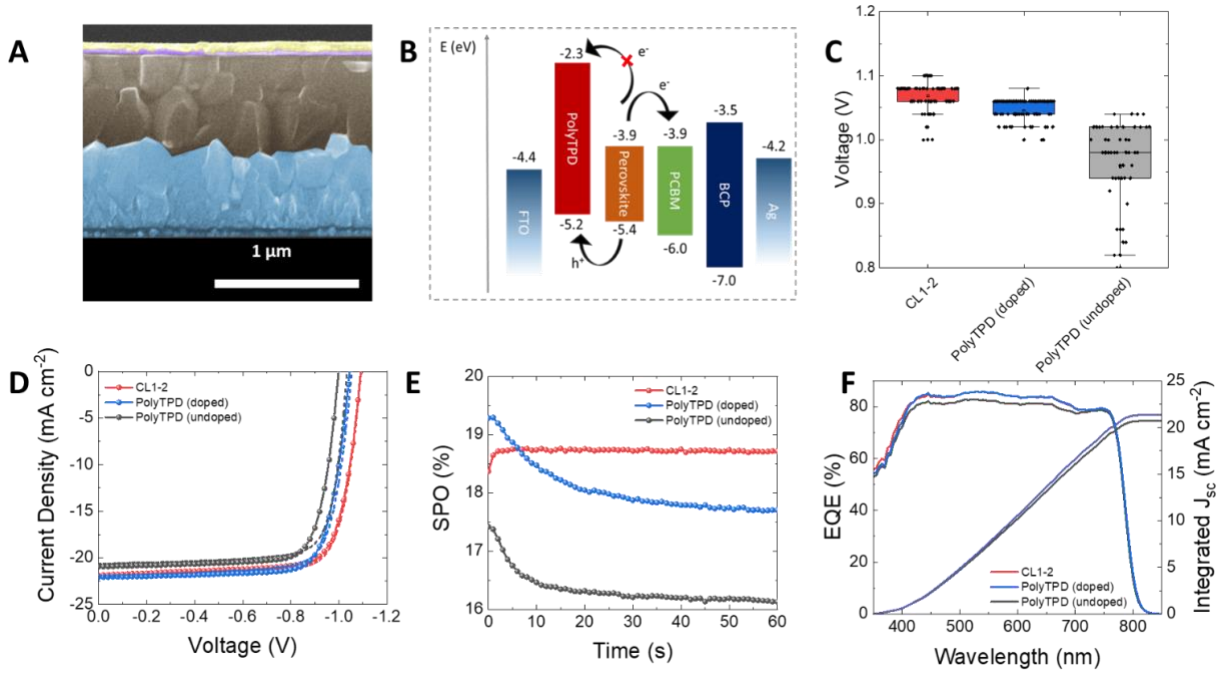


**Fig. 17.** (A) SEM device cross section with FTO (blue), **CL1-2**, $Cs_{0.05}(FA_{0.85}MA_{0.15})_{0.95}Pb(I_{0.9}Br_{0.1})_3$ (gray), PCBM and BCP (purple), and Ag electrode (yellow). (B) Schematic representation of the inverted "p-i-n" PSCs. (C) Comparison of $V_{oc}$ for undoped **CL1-2**, doped PolyTPD, and undoped PolyTPD. (D) J-V characteristics for champion

devices employing undoped **CL1-2**, doped PolyTPD, and undoped PolyTPD collected under AM 1.5G simulated sunlight. (E) Steady-state power output. (F) External quantum efficiency (EQE).

One way that the solar-cell performance of cells with PolyTPD and **CL1-2** HTMs differ is that the latter exhibit somewhat larger $V_{oc}$ values (Fig. 17C). It has previously been shown that Lewis base-containing HTMs or small molecules can passivate the surface traps and electronic disorder at the surface of the perovskite layer; in the present case coordination of the multiple ester moieties present in **CL1-2** to the perovskite surface might act in a similar way, thus reducing recombination and increasing $V_{oc}$ (Fig. 17C). PL lifetime experiments on films of perovskite in contact with undoped **CL1-2** or doped PolyTPD are consistent, the former exhibiting longer lifetimes associated with bimolecular recombination. Correlations between PL decay and $V_{OC}$ have been reported in the literature. In addition, several previous studies have found esters can play a useful role in perovskite growth and/or passivation: poly(methyl methacrylate) has been codeposited with the active layer of n-i-p cells, and used an interlayer between perovskite and HTM in both n-i-p and p-i-n cells.

While no major differences were noticed on the perovskite film on top of FTO/HTMs by SEM and PXRD, a major difference in the perovskite growth is noticeable when glass or tin-doped indium oxide (ITO), both of which are considerably smoother substrates than FTO, are used as the substrate. ITO has achieved slightly higher transmittance in the visible spectrum and can offer somewhat lower resistivity than FTO, making it attractive when maximum current density and fill factor are desired. The **CL1-2** film displays slightly more hydrophilic surface, with a water contact angle, θ, of (82±3)°, than the PolyTPD film (θ = 93±6)°, which could explain why it is easier to spin-coat perovskite on smooth **CL1-2** films on glass or ITO, while it is not possible or difficult for PolyTPD films on glass and ITO. Stronger perovskite-HTM interactions could also be the cause for the improved wettability of **CL1-2** relative to PolyTPD. Indeed, the esters or ether groups of **CL1-2** could possibly hydrogen bond with the cations of the perovskite to facilitate its deposition, or the carbonyl group could form an intermediate adduct with $PbI_2$,[42] and hypotheses such as this will be probed in the future. While PolyTPD can be treated with UV-ozone to improve its wettability, sufficient treatment time to ensure full perovskite film coverage of the substrate substantially degrades photovoltaic device performance. In order to make PSCs on ITO using PolyTPD, we tested a polyelectrolyte that has previously been used to improve the wettability and performance of PTAA in p-i-n PSCs.[41] We find that (9,9-bis(3-(*N*,*N*-dimethylamino)propyl)fluorene-2,7-diyl)-*alt*-(9,9-dioctylfluoren-2,7-diyl) (PFN) treatment on PolyTPD degrades fill factor and the SPO of the PolyTPD devices.

Another consequence of the improved growth of perovskites on **CL1-2** on a smooth substrate relative to that on PolyTPD is shown in Fig. 18. Here we show that a layer of $MAPbI_3$ can be successively coated onto **CL1-2** deposited onto $FA_{0.83}Cs_{0.17}Pb(I_{0.90}Br_{0.10})_3$ (itself grown on FTO), whereas it does not coat an analogous structure using a PolyTPD interlayer. This result suggests cross-linked organic semiconductors may help facilitate solution processing of tandem solar cells, where the crosslinking approach could potentially be extended to allow for a recombination layer that is itself a multilayer composed of sequentially deposited and crosslinked materials with separate hole- and electron-transport functions and potentially with and without dopants. Although multilayer recombination layers of this kind have been fabricated using organic semiconductors, they generally require vacuum evaporation to avoid the deposition of one layer leading to

dissolution of another. An alternative solution-processed approach involves the use of PEDOT:PSS and ITO nanoparticles, but the former may lead to incorporation of traces of water in the device, and both can impair transmission

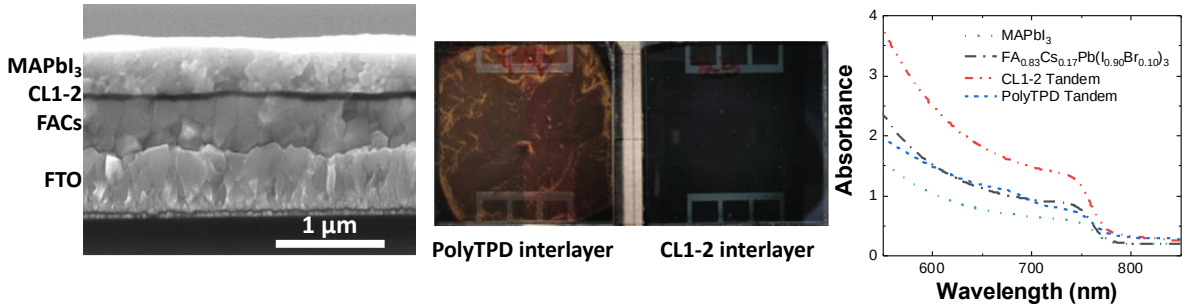


**Fig. 18** Left: SEM cross section showing a "tandem" structure FTO/FACs/**CL1-2**/$MAPbI_3$ (FACs = $FA_{0.83}Cs_{0.17}Pb(I_{0.90}Br_{0.10})_3$). Center: photographs from the top of structures such as those shown left with PolyTPD and **CL1-2** interlayers, indicating a poorer coverage of $MAPbI_3$ when using PolyTPD. Right: absorption spectra of the films shown in the center, compared to those of films of the two perovskite materials deposited separately. These data show use of **CL1-2** leads to a structure that is much more strongly absorbing than FACs alone due to successful deposition of $MAPbI_3$, whereas use of polyTPD does not.

The photo- and thermal-stability of the $Cs_{0.05}(FA_{0.85}MA_{0.15})_{0.95}Pb(I_{0.9}Br_{0.1})_3$ PSCs incorporating **CL1-2** and PolyTPD were studied without encapsulation in a $N_2$-filled glovebox. The devices were periodically removed to ambient atmosphere for measurements under an AM 1.5G solar simulator, where the SPO was measured after 50 s. Fig. 19A shows the stability in an oven at 85 °C; **CL1-2** showed similar stability to PolyTPD devices. Remarkably, the devices show an improvement in performance over the first 1000 hours of aging, and retain greater than their initial efficiency until after 3000 h, which to the best of our knowledge is the longest 85 °C thermal stability timescale reported in the literature.

Photostability was studied under a high intensity LED array (365 nm LED, equivalent to 12 suns UV component of the AM 1.5G spectrum). Initially, a drop in SPO is seen for the PolyTPD devices, while the **CL1-2** devices stayed approximately at the same initial SPO (Fig. 19B). The current density decreased at a greater extent for PolyTPD devices (Fig. 19C). In order to study this instability, we measured the photoluminescence quantum efficiency (PLQE) over time of the perovskite film crystallized on top of the HTM layer on FTO. We observe a 70% drop in PolyTPD PLQE after stabilization (2 min), while the **CL1-2** doped and pristine PLQE retained 81% and 87% of their initial PLQE respectively (Fig. 19D).

In summary, we have described the first use of a photocrosslinked HTM in PSCs. The crosslinkable acrylate copolymer with bis(triarylamine) and cinnamate side chains presented here is promising since it has similar performance to PolyTPD, a widely used HTM, combined with outstanding 85 °C thermal stability and improved PSC UV photostability. Solar cells using **CL1-2** match the state-of-the-art HTM PolyTPD in terms of both performance and stability under 85 °C. We also demonstrated multiple advantages of **CL1-2** over PolyTPD: **CL1-2** does not need to be doped, while PolyTPD does; we achieved highly reproducible photovoltaic performance across multiple batches of devices; the HTM is transparent in the visible region, while PolyTPD is not;

and the perovskite is easier to process on top of the **CL1-2** HTM, which together suggest that the crosslinkable polymeric **CL1-2** is a promising candidate for single junction and tandem solar cells. A paper describing this work has been published (#6 in section V.1).[37]

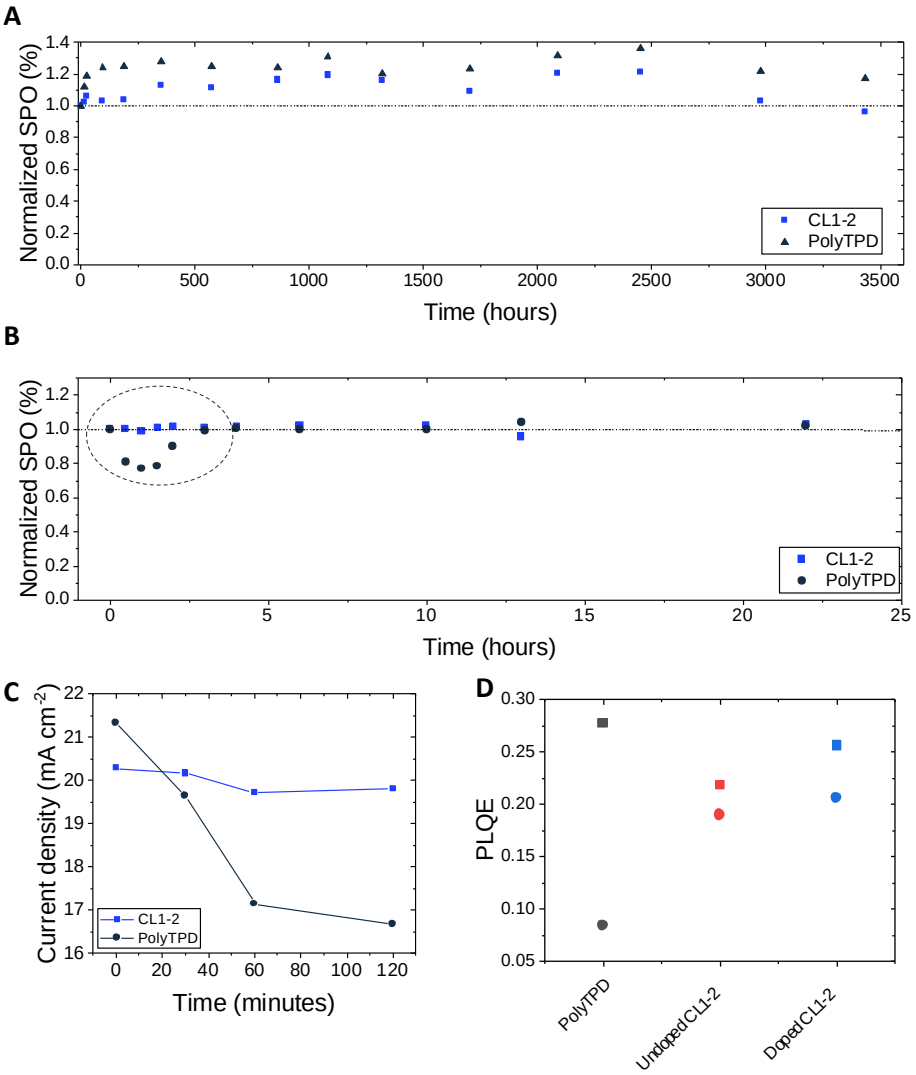


**Fig. 19.** Normalized stabilized power output (SPO) over 50 s after (A) aging the devices at 85 °C in an oven inside a $N_2$-filled glovebox without encapsulation, (B) aging the devices with a UV LED light inside a $N_2$-filled glovebox without encapsulation. The devices were periodically removed to atmosphere for measurements. Both HTMs are doped with $F_4$-TCNQ. (C) Evolution of the current density of **CL1-2** and PolyTPD devices when aged under UV LED light (same experiments as B). (D) Initial (square) and stabilized (circle) PLQE of the half devices (FTO/HTM/perovskite).

*ROMP-Based Polymer with Benzocyclobutene Crosslinking Group*

More recently we have have synthesized a ROMP polymer in which the crosslinking group is a *thermally* crosslinkable benzocyclobutene (BCB), rather than a photocrosslinkable cinnamate. The synthesis of the hole-transporting monomer **A** was carried out as depicted in Fig 20a and was designed to be particularly straightforward, avoid the substitution patterns of the materials

described in the previous sections, while exhibiting an IE close to that of polyTPD. Firstly **I** was subjected to Vilsmeier conditions to obtain the mono aldehyde **II** with 39% yield. Reduction of **II** with sodium borohydride in MeOH, followed by an esterification reaction with exo-5-norbornene-2-carboxylic acid, gave the monomer **A** with 70% yield. **B** was synthesized from the esterification reaction of exo-5-norbornene-2-carboxylic acid and compound **IV** with an excellent yield (80%) (Fig. 20b). The particular BCB crosslinker was chosen based on recent work showing that this BCB structural motif, with OBu substitution on the four-membered ring, allows for crosslinking at only ca. 120 °C,[38] potentially allowing for compatibility with flexible substrates and also for use in n-i-p architectures subsequent to perovskite deposition. **Poly(TPD-co-BBCB)** was successfully synthesized using the Grubbs 3$^{nd}$ generation initiator (see Fig. 20c**)** with different ratios of the crosslinking monomer **B**. The polymer was soluble in a range of organic solvents including, chloroform, dichloromethane, and dichlorobenzene. A broadening of the $^{1}$H NMR peaks was observed, consistent with the formation of a polymer. Moreover, an appreciable downfield chemical shift corresponding to the norbornene alkene protons was observed in the $^{1}$H NMR spectrum of the polymer, consistent with ring-opening of the norbornene. **Poly(TPD-co-BBCB)** was synthesized with 20, 30, and 40% (w/w) of **B**.

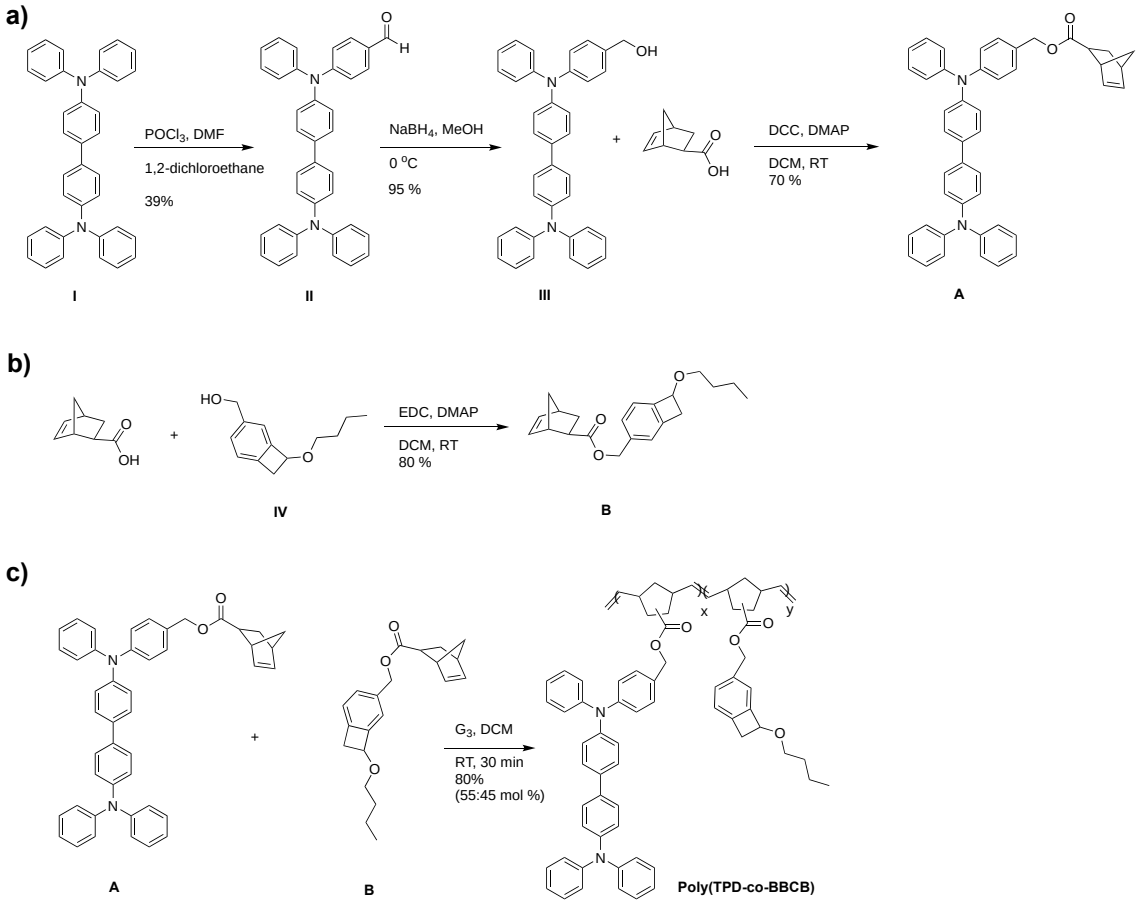


**Fig. 20.** Synthesis routes for monomers **A** and **B** and their copolymer **poly(TPD-BBCB)**.

The insolubilization of the polymers was measured by dissolving 20 mg/mL of the polymer in o-DCB, spin-coating and annealing the film at 120 ºC for 10 min. The film retention was evaluated

by relative change in the optical absorption at 350 nm, upon rinsing with o-DCB. The polymer with 20% **B** showed 0% film retention. When the film was heated at 150 ºC for 10 min, the film retention was calculated to be about 78% (Fig. 21). The polymer with 30% **B** exhibited film retention of 75 % when it was heated at 120 °C for 10 min, **Figure 4.2 (b)** and annealing the film for 20 min, did not improved the film the film retention. However, annealing at 150 ºC for 10 min, resulted the full film retention. Alternatively, by incorporation of 40% **B**, film retention of 100% was achieved when the film is annealed at 120 º C for 10 min.

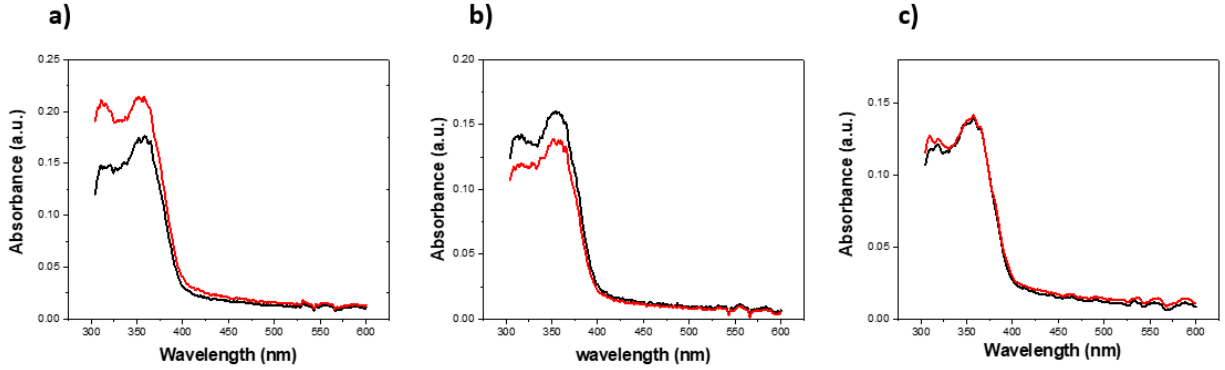


**Fig. 21.** Optical absorption of (a) **poly(TPD-BBCB)** (20 % (w/w) of **B** before (red) and after (black) thermal annealing at 150 ºC for 10 min (b) **poly(TPD-BBCB)** (30 % (w/w) of **B** before (red) and after (black) thermal annealing at 120 ºC for 10 min and (c) **poly(TPD-BBCB)** (40 % (w/w) of **B** before (red) and after (black) thermal annealing at 120 ºC for 10 min.

The IE of the polymer was estimated to be ca. 5.2 eV, i.e. of borderline feasibility for doping with $F_4$TCNQ. Indeed, addition of $F_4$-TCNQ to solutions of **poly(TPD-co-BBCB)** leads to only moderate changes in the optical spectra, suggesting inefficient doping with this oxidant. On the other hand, chemical oxidation of poly(TPD-co-BBCB) (10 mg/mL) with 2.5 mg of Mo(tfd-$CO_2CF_3)_3$ in o-DCB resulted in the immediate formation of a dark orange solution of the radical cation. Films of the doped solution were spin-coated and UV-vis-NIR of films were obtained before and after cross-linking (annealing the films at 120 ºC for 10 min) to examine the compatibility of the thermal crosslinking approach with doping prior to crosslinking. For **poly(TPD-co-BBCB)** the absorptions in the UV-vis region (309, 356 nm) (Fig. 22) (black) are replaced by appearance of signals at 1000-2000 nm and 500 nm and which are characteristic of radical cations of this type (red). However, annealing the doped film resulted decomposition of doped film as the color of the doped film changed from orange to dark blue and the signals for radical cation species were found to disappear.

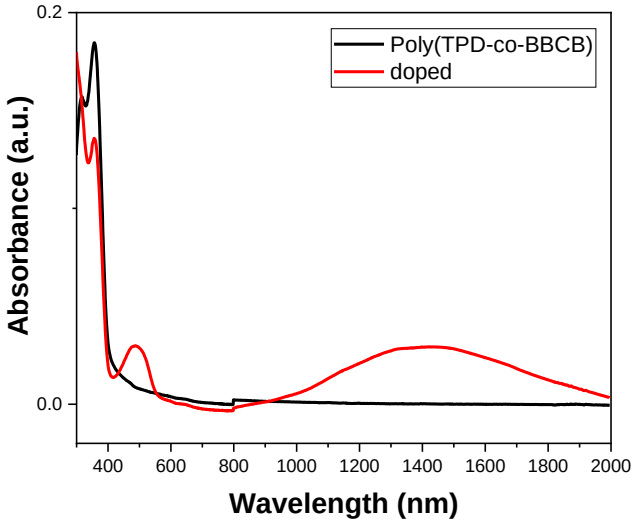


**Fig. 22.** Optical absorption of poly(TPD-co-BBCB) and doped poly(TPD-co-BBCB) using $Mo(tfd\text{-}CO_2CF_3)_3$

We wondered if the diradical intermediate involved in BCB ring opening and dimerization undergoes reaction with $Mo(tfd\text{-}CO_2CF_3)_3$ (or its anion), causing the decomposition of doped films. To test the hypothesis, 12 mg of $Mo(tfd\text{-}CO_2CF_3)_3$ and 5 mg of a simple BCB-containing molecule were dissolved in o-DCB in glove box and heated at 120 ºC for 15 min. The $^{19}F$ NMR of the mixture was obtained in $CDCl_3$. $Mo(tfd\text{-}CO_2CF_3)_3$ represents two signals at (Fig. 23a), however, after $Mo(tfd\text{-}CO_2CF_3)_3$ was mixed with Br-BBCB and heated at 120 ºC, showed a very complex $^{19}F$ NMR spectrum was obtained, confirming the decomposition of $Mo(tfd\text{-}CO_2CF_3)_3$ (Fig. 23b).

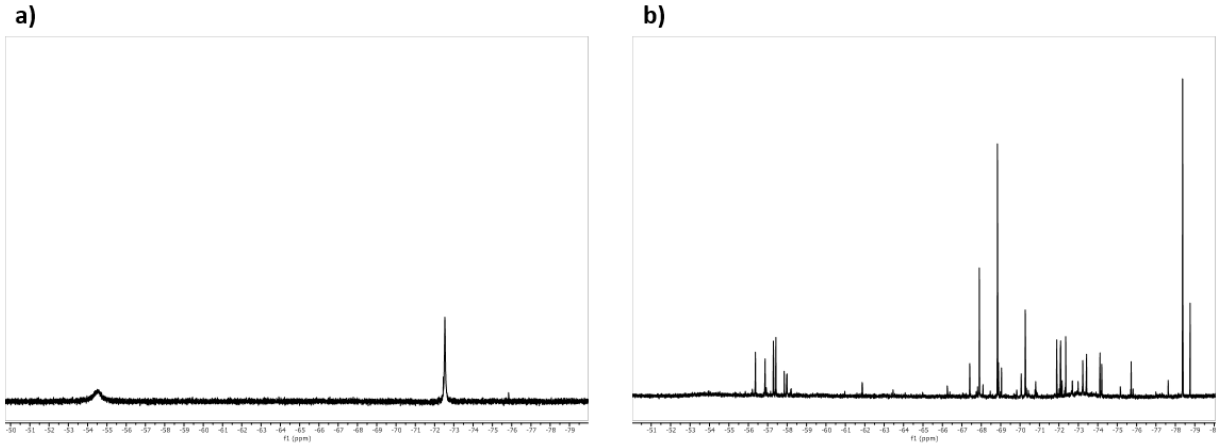


**Fig. 23.** $^{19}$ F NMR of $Mo(tfd\text{-}CO_2CF_3)_3$ mixed with a simple BCB before (a) and after (b) heating at 120 °C for 15 min.

Next, “magic blue” (tris(4-bromophenyl)ammoniumyl hexachloroantimonate) was investigated for doping studies of poly(TPD-co-BBCB). Magic blue has limited solubility in o-DCB but $CH_3CN$ dissolves it very well. On the other hand, poly(TPD-co-BBCB) has very low solubility in $CH_3CN$. Therefore, it was decided to use sequential doping instead of solution mixed doping. To

do that, films of the **poly(TPD-co-BBCB)** (5.0 mg/mL) were spin-coated. Magic blue in $CH_3CN$ (2.0 mg/mL) was spin-coated on the top of the poly(TPD-co-BBCB) that lead to immediate formation of an orange film. UV-vis-NIR of films were obtained before and after cross-linking (annealing the films at 120 °C for 10 min). Fig. 24a shows upon sequential doping with magic blue, the signals corresponded to radical cation appeared (presence of a broad signal at 1000-2000 nm, but that, after crosslinking, the polymer seemed to dedope with the broad signal in the NIR region disappearing. We also wondered if the diradical intermediate used in crosslinking reacts with the dopant or the doped polymer. To test this idea another (non-crosslinkable) hole-transport polymer was doped with magic blue in the same way and annealed at 120 °C. Again, the doped polymer underwent dedoping under thermal annealing, Fig 4b indicating that the doped polymers of this type, at least when doped with magic blue, are unstable under thermally crosslinking conditions, even in the absence of crosslinking groups. Further work is required to fully understand this observation. Some dopants such as $F_4TCNQ$ are known to undergo thermal dedoping, but this can be attributed to the reverse electron transfer followed by sublimation of the volatile neutral dopant. However, such a mechanism is likely not operative in the present case since the counterion introduced is the more-or-less redox-inactive $SbCl_6^-$ and magic blue itself is involatile.

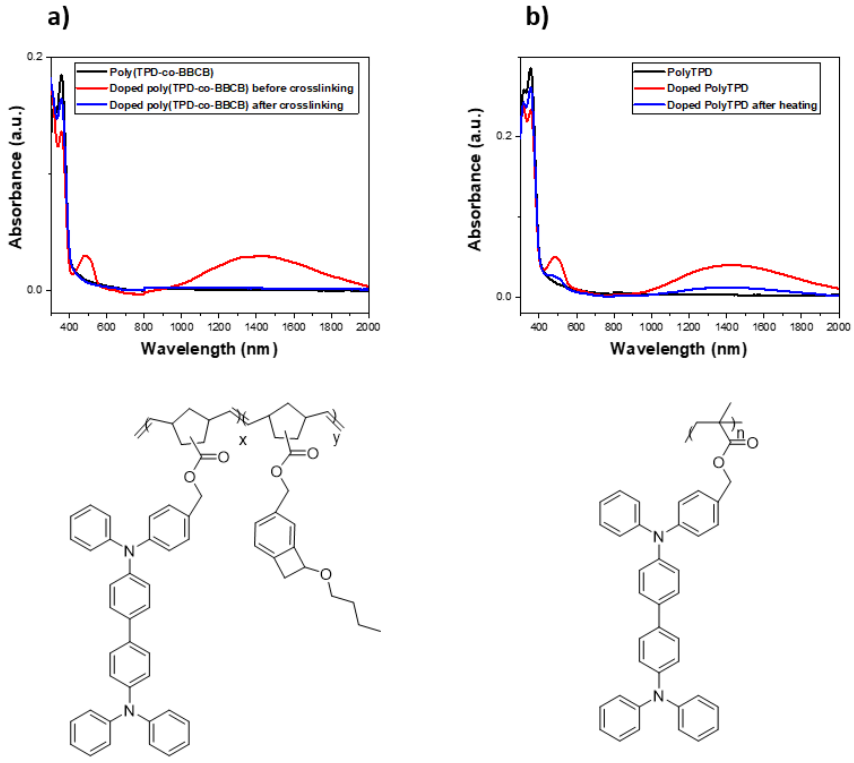


**Fig. 25.** Magic-blue-doped side-chain polymers before and after thermal annealing at 120 °C.

*Universal Crosslinker Approach*

In the previous sections moieties were incorporated into hole-transport polymers that undergo dimerization – either photochemically (cinnamates) or thermally (BCBs). An alternative, and potentially simpler, approach to incorporation of crosslinking groups into hole-transport polymer

is to mix a homopolymer with a "universal crosslinker" that has several reactive groups that can "bite" into several homopolymer chains. Aryl azides constitute one such class: UV leads to liberation of $N_2$ and generation of a reactive nitrene that inserts into the most accessible C—H bonds, typically in alkyl groups (Fig. 26 right). We have made several such azides (Fig. 26 left) as potential crosslinkers for hole-transport materials in PSCs. We note that may equally well be suitable for crosslinking electron-transport materials.

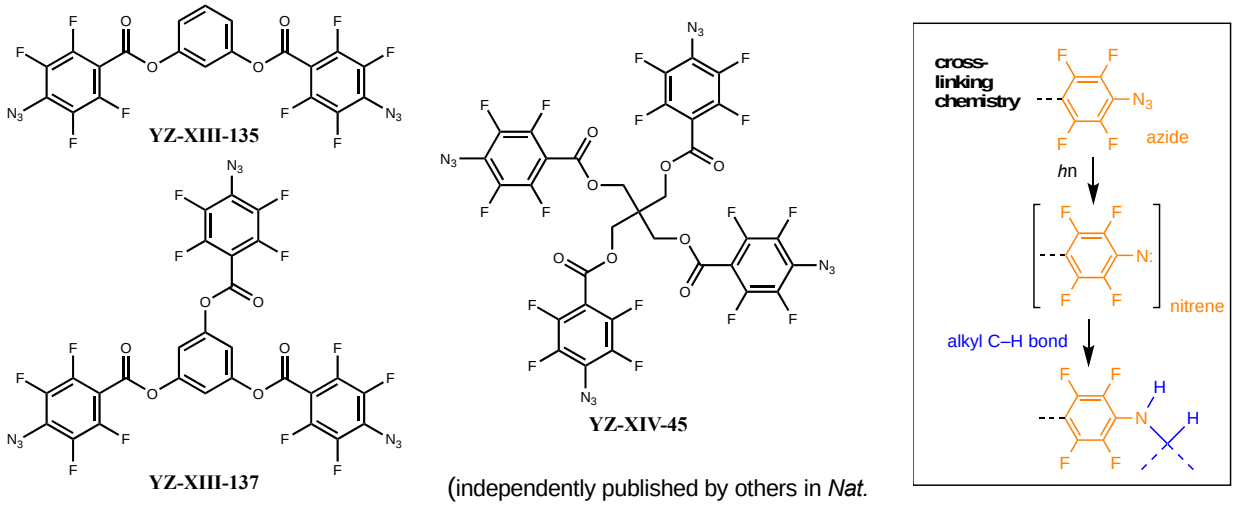


**Fig. 26.** Left: oligo(aryl azides) synthesized. Right: irradiation of an aryl azide, followed by insertion of the resulting nitrene into a C—H bond.

The use of such crosslinkers has been demonstrated by collaboration with Ronald Osterbackä's group at Åbo Academie University (Finland), where the tris(azide) was used to insolubilize P3HT (Fig. 27), with the crosslinked layer permitting subsequent deposition of an additional semiconductor, specifically a P3HT:PCBM bulk heterojunction blend, with the crosslinked layer serving as a hole-extraction layer that, when doped, behaves similarly to PEDOT:PSS (Fig. 27). Over-doping leads to poorer performance, however, which can be explained by dopant migration into the active layer. Thus, longer term stability may be impacted by this dopant migration, indicating that photo-activation does not result in efficient reaction of nitrenes with the C—H bonds of the dopants. These we will be important consideration to bear in mind going forward with the application of such crosslinking chemistries to the insolubilization of hole-extraction layers for PSCs. A paper on this work is currently under revision (#14 in section V.1).

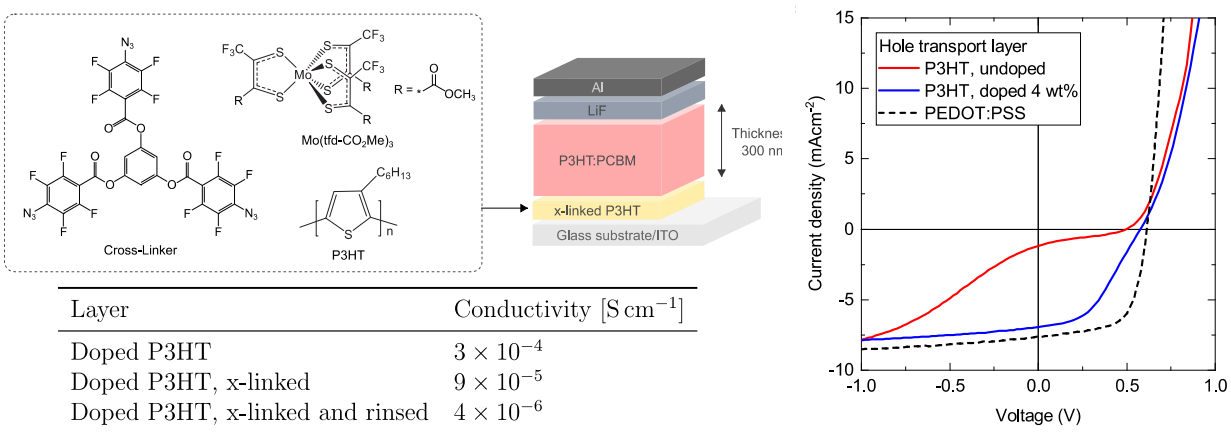


| Layer | Conductivity [S cm$^{-1}$] |
|---|---|
| Doped P3HT | $3 \times 10^{-4}$ |
| Doped P3HT, x-linked | $9 \times 10^{-5}$ |
| Doped P3HT, x-linked and rinsed | $4 \times 10^{-6}$ |

**Fig. 27.** Use of a tris(azide) to insolubilize doped P3HT for use as a hole-extraction layer (top left), conductivity data for P3HT (doped at 2 wt %) with and without crosslinking and solvent rinsing (lower left), and J-V characteristics for a cell wth doped and undoped crosslinked P3HT hole-extraction layers compared to PEDOT:PSS.

## IV.3. Electron-Transport Materials for Perovskite Solar Cells

*Use of Additive in PCBCB Electron-Extraction Layers*

Fullerene derivatives work well and have been extensively used in PSCs, in part due to the favorable alignment of their lowest unoccupied molecular orbitals with the conduction band of perovskite absorbers. Insolubilization of the ETM subsequent to deposition is an effective approach to increase the mechanical and thermal stability of the material, to permit solution deposition of additional layers, and may also be expected to restrict diffusion of ions.[39] The Marder group has previously reported an analogue of the widely used PCBM (Fig. 28) in which the methyl group is replaced by a benzocyclobutene (BCB) moiety. Heating to 150 °C results in the formation of fullerene oligomers $(PCBCB)_n$ (dimers are detected by mass spectrometry) and insolubilization of films in solvents such as DMF and chlorobenzene.[40,41] BCBs are well known to undergo thermal ring opening of the four-membered ring to give *o*-quinodimethane derivatives, which can then dimerize to form dibenzocyclooctanes. In PCBCB the quinodimethane intermediates can also undergo cycloaddition with the fullerene core.[40, 42] We have previously used thermally insolubilized $(PCBCB)_n$ to prevent aggregation of fullerenes in OPVs under thermal aging at 150 °C,[40] and as an ETM in so-called *n-i-p* (negative-intrinsic-positive) PSCs,[41] which reached stabilized power conversion efficiencies (PCEs) above 17%.[43]

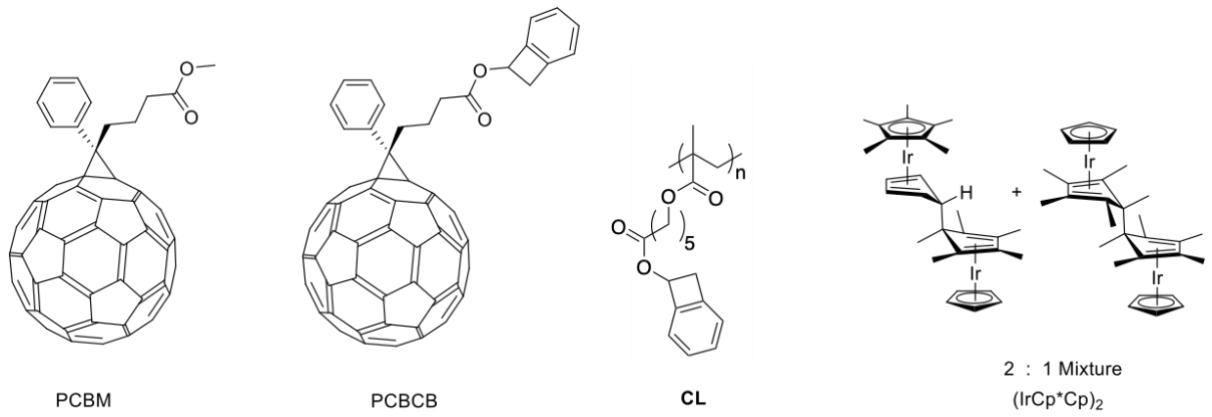


**Fig. 28.** Molecular structures of the materials discussed in this section: the ETMs PCBM (reference) and PCBCB, the crosslinker (CL) and the *n*-type electrical dopant $(IrCp^*Cp)_2$.

We speculated that the stability of PCBCB films might be further improved if a fully crosslinked film could be formed on heating. During this reporting period, we have examined the possibility of using a crosslinker, CL (Fig. 28), consisting of poly(methacrylate) with pendant BCB groups, as an approach to increasing connectivity between the $(PCBCB)_n$ oligomers. The polymeric crosslinker CL was synthesized via polymerization of a methacrylate monomer containing a BCB moiety using the radical initiator azobisisobutyronitrile (AIBN) (see Fig. 29). The polymer had good solubility in chlorobenzene, the solvent used in previous work for the solution deposition of PCBCB. Gel permeation chromatography against polystyrene standards yielded a molecular weight of 580 kg/mol and a dispersity index of 2.

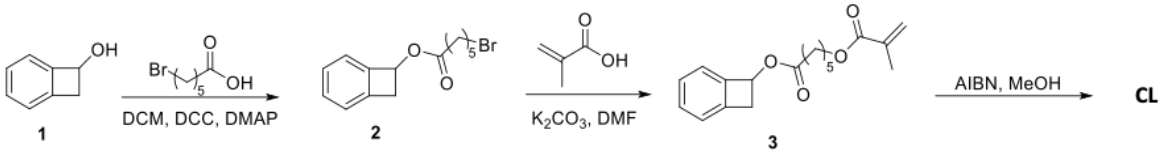


**Fig. 29.** Synthesis of the crosslinker CL. DCM = dichloromethane, DCC = *N*,*N'*-dicyclohexylcarbodiimide, DMAP = 4-dimethylaminopyridine, DMF = *N*,*N*-dimethylformamide, AIBN = azobisisobutyronitrile, MeOH = methanol.

n-Doping can be used to fill electronic traps and increase the number of charge carriers in an ETM, leading to increased conductivity of the ETM, and to reduce barriers for electron extraction (and injection). Moderately air-stable 19-electron sandwich organometallic dimers, $(MCp^*Cp)_2$ (where Cp* = pentamethylcyclopentadienyl; Cp = cyclopentadienyl, M = Rh,[44] Ir[45]) and $(RuCp^*mes)_2$,[46] can n-dope ETMs with electron affinities as small as ca. 2.8 eV and do not form byproducts.[47-51] The fairly large size of the corresponding monomeric cations formed on doping, at least relative to those of species such as alkali-metal ions, may hinder their diffusion in the ETM layer. We find $(IrCp^*Cp)_2$ dopes both solutions of PCBCB and films of $(PCBCB)_n$, forming fullerene radical anions, $PCBCB^{\bullet}$, and iridium monomer cations, $(IrCp^*Cp)^+$. As the molar concentration of dopant is increased, the absorption peak corresponding to the neutral acceptor at 330 nm[40] decreases in intensity while the presence of a peak at 1070 nm, corresponding to the fullerene radical anion,[52, 53] becomes more evident.

Transmission-line measurements were performed to quantify the impact of dopant and cross-linker addition on the in-plane electrical conductivity of $(PCBCB)_n$ films. The sheet resistance ($R_s$) of the ETMs spin-coated on glass with a silver electrode on top was measured to determine their

conductivity ($\sigma$), their resistivity ($\rho$), and the resistance at the ETM/Ag contact ($R_c$). A $(PCBCB)_n$ film insolubilized by heating to 200 °C for 10 min has an in-plane conductivity comparable to that of PCBM films. When the organometallic dimer is incorporated into the casting solution, the conductivity of $(PCBCB)_n$ increases by up to four orders-of-magnitude ($3.7 \times 10^{-7} \pm 2.2 \times 10^{-7}$ S $cm^{-1}$ to $1.4 \times 10^{-3} \pm 3.8 \times 10^{-4}$ S $cm^{-1}$), confirming doping of the ETM by the Ir-dimer. To assess the impact of the introduction of CL (1-30 mol%) on the in-plane electrical conductivity, the nominal concentration of $(IrCp^*Cp)^+$ in the $(PCBCB)_n$ films (based on the contents of the casting solution) was kept constant at 3 mol%. Use of 1 mol% CL in the casting solution causes the conductivity to increase ten-fold ($3.3 \times 10^{-4} \pm 2.3 \times 10^{-4}$ S $cm^{-1}$ to $5.5 \times 10^{-3} \pm 5.4 \times 10^{-4}$ S $cm^{-1}$). The conductivity remains roughly constant with additional CL, up to 30 mol% ($5.9 \times 10^{-3} \pm 3.4 \times 10^{-3}$ S $cm^{-1}$). This may be related to previous observations that the rheological, mechanical and electrical properties of organic semiconductors can in some cases be improved by addition of simple polymers such as poly(methyl methacrylate (PMMA) (i.e., a polymer similar to CL, but lacking the BCP side chain).[54-59]

We performed x-ray photoelectron spectroscopy measurements (XPS) to determine the impact of CL addition on the retention of $(IrCpCp^*)^+$ cation in $(PCBCB)_n$ films upon washing (see Fig. 30). We measured the elemental composition of $(PCBCB)_n$ films (doped with a nominal 3 mol% of IrCp*Cp) with and without crosslinker, as prepared and after spin-coating solvents commonly used in device fabrication (chlorobenzene and DMF). Without CL, the iridium elemental contribution – calculated from the area under the Ir 4f peaks – of the $(PCBCB)_n$ films decreases upon washing with chlorobenzene and DMF. When 10 mol% of CL was added in the precursor solution of doped PCBCB, the elemental contribution of iridium remains unchanged after washing with DMF or chlorobenzene, showing a better immobilization of the dopant in the films containing CL.

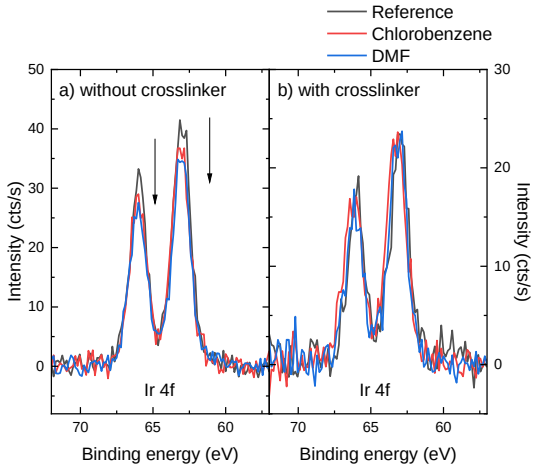


**Fig. 30.** Iridium elemental contribution in doped $(PCBCB)_n$ films with 3 mol% $(IrCp^*Cp)_2$ without CL (a) and with 10 mol% CL (b) as prepared, and after spin-coating chlorobenzene or DMF onto the film. The elemental contribution of iridium is calculated from the area under the Ir 4f peaks in XPS spectra. The carbon elemental contribution in the same films is constant regardless of washing.

PSCs with the *p-i-n* architecture were fabricated to assess the impact of the additive crosslinker on device performance and stability. The device structure was FTO/$F_4$-TCNQ-doped PolyTPD/$Cs_{0.05}(FA_{0.85}MA_{0.15})_{0.95}Pb(I_{0.9}Br_{0.1})_3$/ETM/BCP/Ag, where ETM is either PCBM or $(PCBCB)_n$ with and without crosslinker and dopant, FA is formamidinium, MA is methylammonium, PolyTPD is poly(4-butyl-triphenylamine-4',4"-diyl) and BCP is

bathocuproine. The selected perovskite is a relatively stable triple cation (FAMACs) lead mixed-halide perovskite, processed from solutions of DMF and dimethylsulfoxide (DMSO). State-of-the-art solar cells with ETM = PCBM were used as the reference. The device performance parameters averaged over 20 solar cells for each type of ETM, as well as the champion cells, are shown in Table 1. The current density – voltage (*J* – *V*) curves of the best-performing solar cells are shown in Fig. 31.

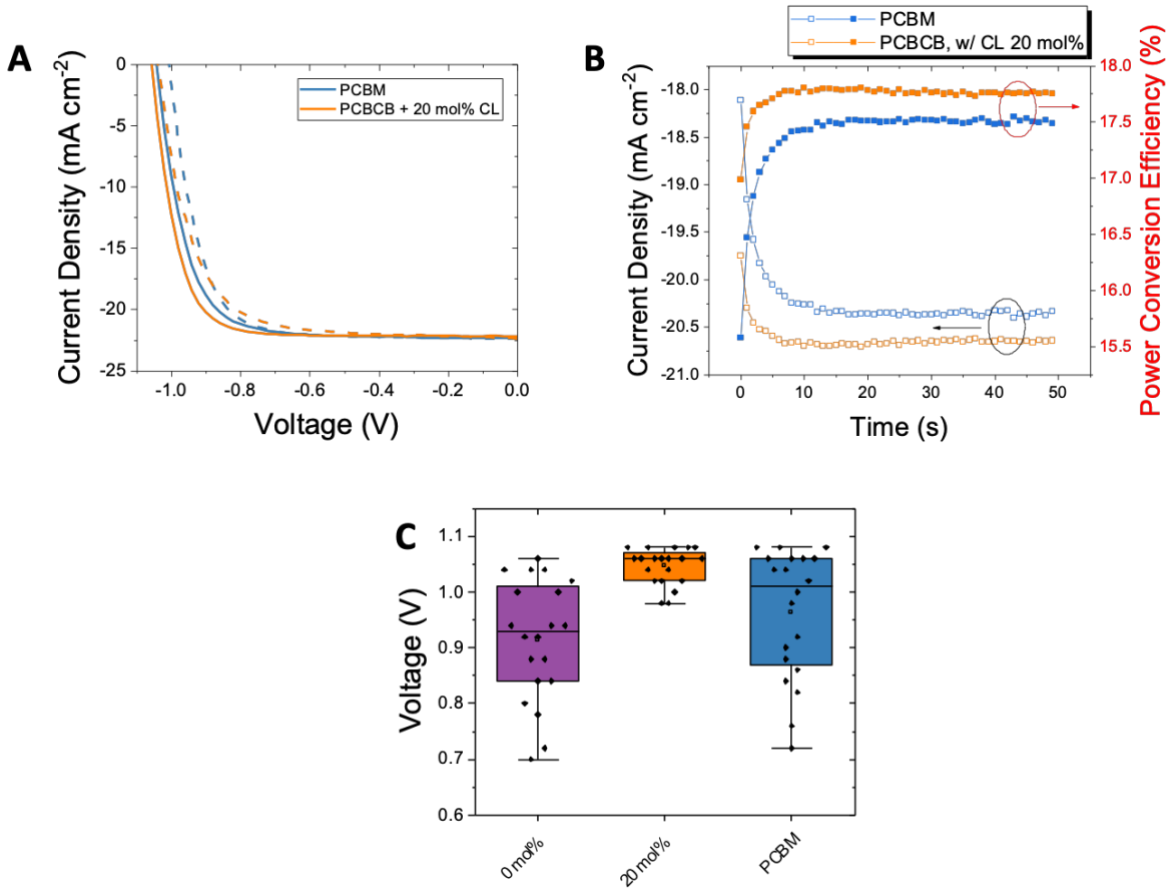


**Fig. 31.** (A) *J-V* characteristics for champion devices employing $(PCBCB)_n$ with 20 mol% CL and PCBCB collected under AM 1.5G simulated sunlight. Solid line: reverse scan, dotted line: forward scan. (B) Steady-state power output and current density over time. (C) Comparison of $V_{oc}$ for $(PCBCB)_n$, $(PCBCB)_n$ with 20 mol% CL and PCBM.

**Table 2.** Statistics for 20 individual FAMACs devices using undoped ETM. PCBCB films were thermally insolubilized.

| | | $J_{sc}$ (mA cm$^{-2}$) | $V_{oc}$ (V) | FF | PCE (%) |
|---|---|---|---|---|---|
| $(PCBCB)_n$ | Average | 21 ± 2 | 0.92 ± 0.1 | 0.65 ± 0.05 | 12 ± 2 |
| | Maximum | 23.20 | 1.06 | 0.72 | 15.35 |
| $(PCBCB)_n$ with 20 mol% CL | Average | 21.5 ± 0.8 | 1.05 ± 0.03 | 0.68 ± 0.03 | 16 ± 2 |
| | Maximum | 22.87 | 1.08 | 0.78 | 18.54 |
| PCBM | Average | 20 ± 2 | 1.0 ± 0.1 | 0.70 ± 0.07 | 14 ± 3 |
| | Maximum | 22.39 | 1.08 | 0.77 | 17.64 |

On average, the $V_{OC}$ obtained during the reverse scan are 0.92 V and 1.05 V for PSCs fabricated with undoped $(PCBCB)_n$ and $(PCBCB)_n$·CL, respectively. The increase in $V_{OC}$, shown in Fig. 31, suggests a reduction of non-radiative recombination at the interface. Moreover, variations in $V_{OC}$ across devices with $(PCBCB)_n$·CL (20 mol%) are smaller compared to those in devices with unmodified $(PCBCB)_n$ or PCBM, showing better reproducibility of the devices incorporating CL in the ETL. The improved average $V_{OC}$ for $(PCBCB)_n$·CL PSCs leads to an improvement of PCE, which is 16% on average, with a maximum value of 18.5%. The champion cells containing $(PCBCB)_n$·CL exceeded the performance of those using state-of-the-art PCBM as ETM.

While doping PCBM with n-dopants such as N-DMBI-H improves the performance of the PSC using this architecture,[60-64] those made with Ir-doped $(PCBCB)_n$ did not show an improvement over the undoped analogue. Nevertheless, in other types of architecture, this type of dopant has been seen to improve the performance of the PSCs.[49, 50, 65] The $V_{oc}$ of the PSCs decreases upon doping of the ETM, probably due to an increase of charge recombination at the perovskite:ETM interface. It has previously been shown that improvements in the conductivity of a charge-transport material do not necessarily lead to an improvement of the solar cell performance.[66, 67]

The photoluminescence (PL) properties of the different ETMs on top of the perovskite film on glass are comparable, which is not surprising due to the chemical similarities of the ETMs (Fig. 33). The carrier lifetime and photoluminescence quantum efficiency (PLQE) are similar across all ETMs. Notably, the PL spectra appear to contain, two features; one centred at ~ 770nm and one at ~790nm. Since this material does contain mixed halides, we presume that the higher energy feature corresponds to the majority phase emission of the $Cs_{0.05}(FA_{0.85}MA_{0.15})_{0.95}Pb(I_{0.9}Br_{0.1})_3$ compound, and the lower energy feature corresponds to iodide-rich phase-segregated domains. Since we observe a smaller contribution from the low energy emission feature from all the films containing the ETM layers, our results suggest that the halide segregation is supressed by the presence of the ETM layers, possibly due to a lower net photoinduced electron density in the perovskite absorber layer due to electron extraction.

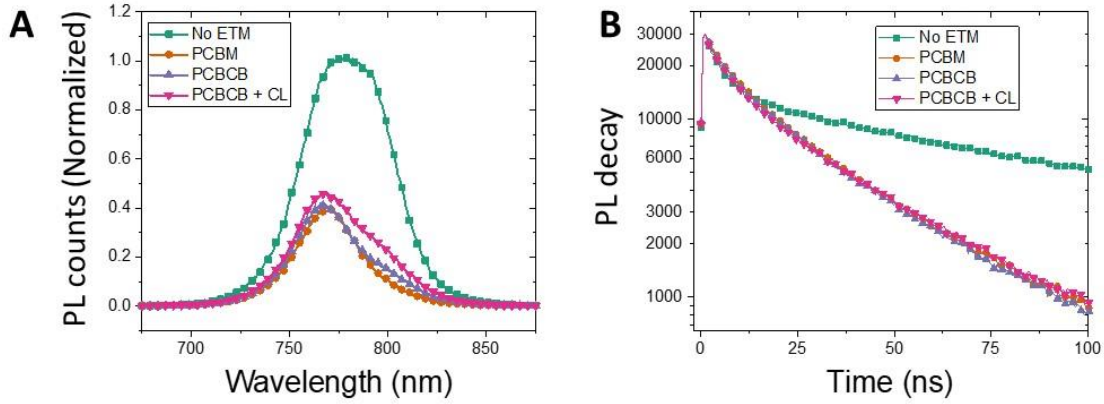


**Fig. 32.** Steady state PL (A) and time-resolved PL (B) of half devices on FTO.

PSCs with the p-i-n architecture were aged in the dark in inert atmosphere at 85 °C to investigate the dependence of the thermal stability on the choice of ETM (see Fig. 33 for data for the doped ETMs). The PSCs were brought to atmosphere and room temperature for steady-state power output (SPO) measurement. Despite some fluctuations, the PSCs were stable for more than 3000 h. From

500 hours onwards, the PCBM cells had degraded more than the cels containing $(PCBCB)_n$, and after 4500 h, there is a clear distinction between. The additive cross-linker also appears to slightly improve the stability of the cells over the oligomeric analogue ($(PCBCB)_n$·CL vs $(PCBCB)_n$). Notably, after 3000 hours, the best cells retained 90% of their starting efficiency, and still retained 87% of their starting efficiency after 4500 hours.

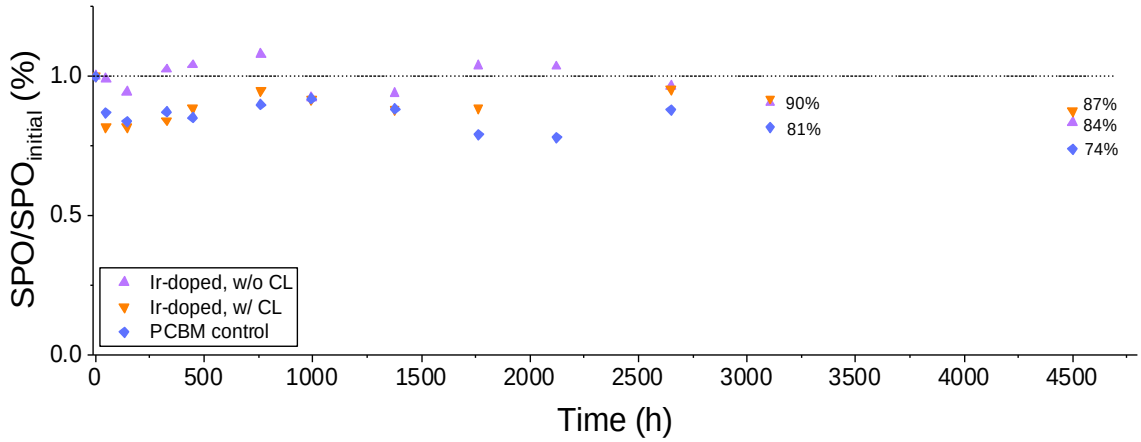


**Fig. 33.** Stability comparison of non-encapsulated perovskite solar cells (PSCs) fabricated using doped $(PCBCB)_n$, doped $(PCBCB)_n$·CL (20 mol%) and PCBM. An average of four devices per each data point is reported. The SPO is normalized to the initial SPO.

In summary, adding the crosslinker CL to PCBCB inhibits washing of $(IrCp^*Cp)^+$ from the film and does not negatively affect the electrical conductivity of the doped $(PCBCB)_n$. While the conductivity of the $(PCBCB)_n$ film was improved using the $(IrCp^*Cp)_2$ dopant, the performance of the PSCs decreased with its addition. PCSs made using $(PCBCB)_n$ with CL leads to an improvement in PCE, as well as an improved performance reproducibility. The PSC degradation is diminished when the crosslinker is added, showing a promising avenue to obtain long-term stable solar cells. This work has now been published (#11 in section V.1).[68]

*Reducing the PCBCB Crosslinking Temperature*

PCBCB, discussed in the previous sub-section, becomes insolubilized at 150-200 °C. It has recently been reported that an alkoxy (hereafter BBCB where the first B represents "butoxy"), rather than ester moiety, on the four-membered ring of a BCB lowers the ring-opening reaction temperature still further.[38] Synthesis of a PCBM-like fullerene with incorporating this lower-temperature insolubilizing group was carried out as shown in Fig. 34. [6,6]-phenyl-$C_{60}$-butyric acid (PCBA) was synthesized from commercially sourced PCBM.[40] The alcohol-BBCB precursor was synthesized from the reduction of the corresponding aldehyde using $NaBH_4$ in MeOH with 80% yield. The PCBA was subsequently esterified with the BBCB alcohol under *N*,*N*-dicyclohexylcarbodiimide (DCC)-assisted esterification conditions in o-DCB in order to obtain the desired product, phenyl-$C_{61}$-butyric acid butoxybenzocyclobutene ester BBCBPCB, which is readily soluble in common organic solvents (toluene, $CH_2Cl_2$, benzene), and was purified though column chromatography with 50% yield.

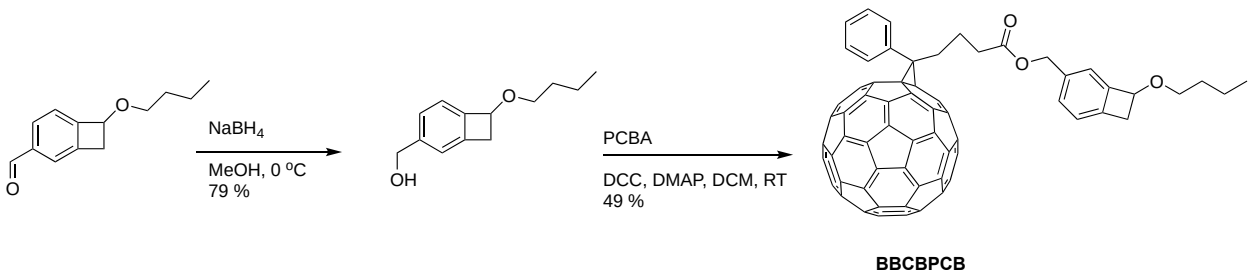


**Fig.** Error! No text of specified style in document.**4** Synthesis of fullerene with a BBCB thermal crosslinker, BBCBPCB.

DSC analysis of the BBCBPCB in hermetically sealed Al pans was carried out from a starting temperature of -50 °C with heating to 300 °C at a rate of 10 °C min. The heating and cooling cycles are shown in Fig. 35a. The first cycle showed a feature indicative of an exothermic chemical reaction beginning at 120 °C, consistent with expectations for a BBCB derivative, and attributed to the dimerization or oligomerization reactions of BBCB. To determine the effect of heating the BBCBPCB precursor on solubility, UV-vis spectroscopy was used. Drop-cast films from the PCBBCB precursor (1 mg) in $CH_2Cl_2$ (1 ml) were deposited on glass substrates and annealed at different temperatures for 10 min. The films were subsequently washed with 1 ml of $CH_2Cl_2$ each and sonicated to remove any soluble parts of the film. These 1 ml solutions were diluted to 10 times their volume and the absorption spectra for those were then obtained. As it can be seen, by varying the annealing temperature from 90 °C to 120 °C, the percentage conversion increased; at 120 °C no detectable soluble material was obtained, suggesting 98% of the film to be insoluble (Fig. 35b). Fig. 36 shows the anticipated reactions that lead to insolubilization based on those seen for PCBCB.[69] We have conducted some tests on the doping of BBCBPCB and immobilization of custom-synthesized BBCB-functionalized dopants in this material, but these studies are beyond the scope of this report. The use of this dopant in PSCs will be examined in future.

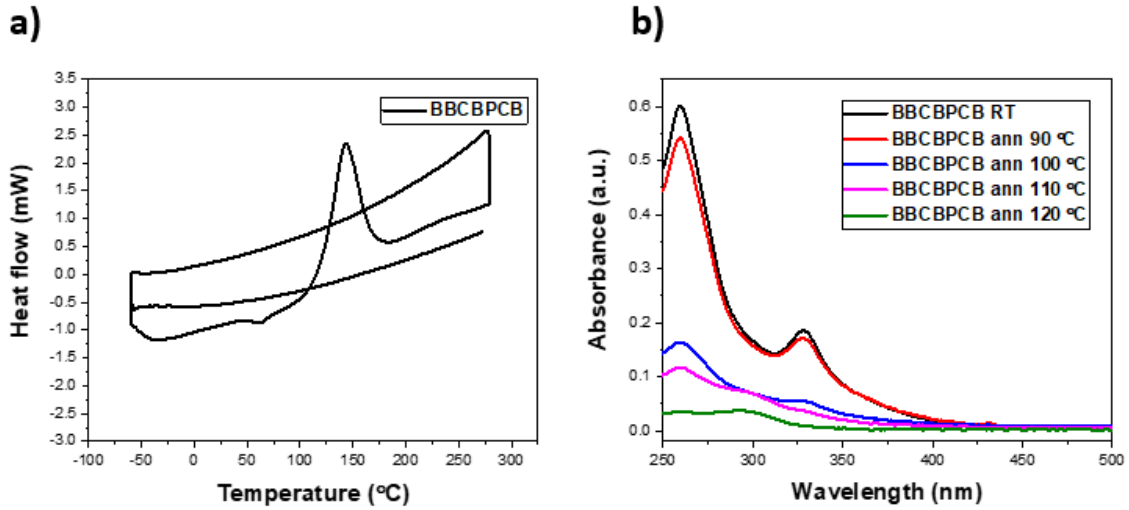


We h

**Fig. 35.** a) DSC thermogram of cross-linking reaction of BBCBPCB moieties and b) UV-vis absorption spectra of BBCBPCB annealed at different temperatures.

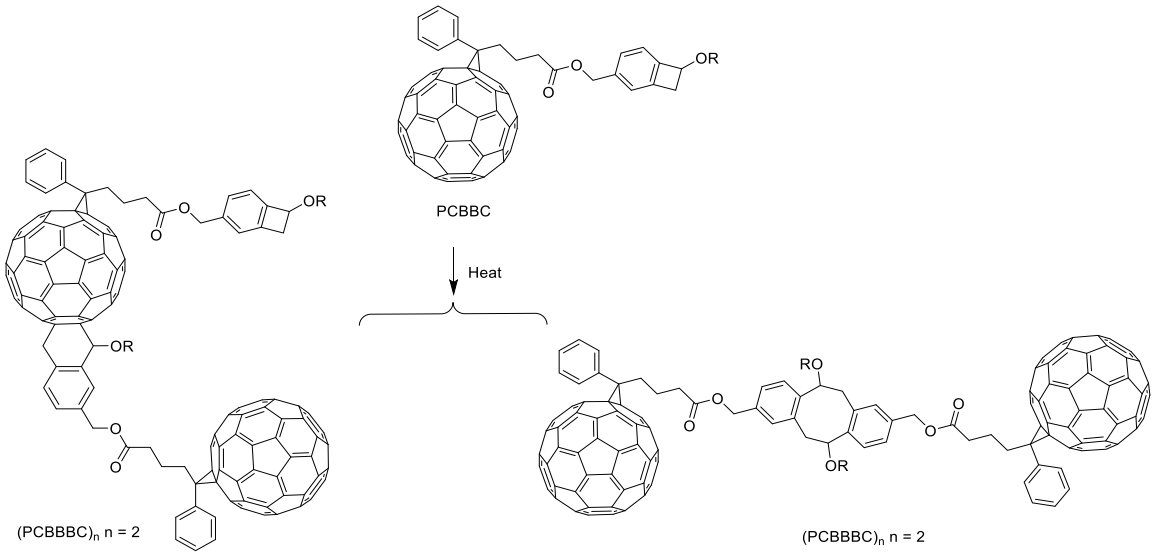


**Fig. 36.** Schematic representation of oligomeric fullerene formation ((PCBCB)n, n = 2) via thermal cross-linking of BBCBPCB.

*Other Studies of Electron-Transport Layers*

The Marder group has also collaborated with other groups in the area of electron-transport layers for PSCs, in particular providing the n-dopant $(RuCp^*mes)_2$ (Fig. 1) to the groups of Henk Bolink at the University of Valencia (Spain) and Henry Yan at the Hong Kong University of Science of Technology (China). Work with Bolink is summarized in Fig. 37, which shows fully evaporated PSCs fabricated on ITO substrates. Without doping, the devices give a low open-circuit voltage. Optimal doping of the $C_{60}$ layer with $(RuCp^*mes)_2$, however, leads to greatly improved $V_{OC}$ and to a PCE of almost 18%. This work has now been published (#4 in section V.1).[70]

The Yan group have used the same n-dopant for the solution doping of a solution-processed non-fullerene electron-transport material, QS25, in two different device architectures; in both cases, the PCE of the devices is significantly improved. In particular, devices ITO/P3CT-Na/$MAPbI_3$/QS25:$(RuCp^*mes)_2$/$C_{60}$/BCP/Ag, exhibit an exceptionally high fill factor of 0.86.

A study of the effects of surface modification of an $SnO_2$ electron-extraction layer with phosphonic acids has also been completed and published (#2 in section V.1).[71] Finally, this grant has also partially supported work on an "electrostatic crosslinking" approach to n-doping that may be useful in insolubilizing electron-transport materials through activation of doping to form multiply-charged cations. Fig. 39 shows the dopant that we have synthesized. Its doping behavior and role in insolubilizing polymeric electron-transport materials has been studied in collaboration with Norbert Koch (Humboldt University of Berlin) and a paper is currently in preparation.

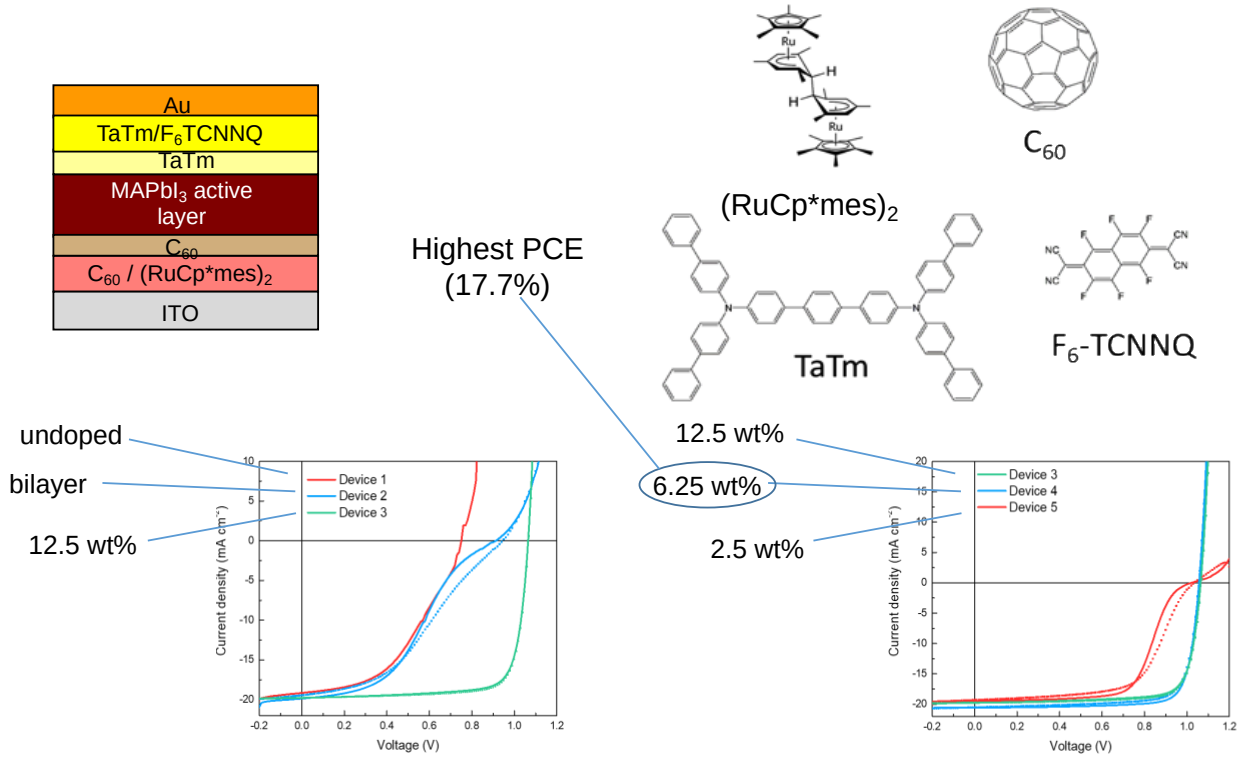


**Fig. 37.** Fully evaporated PSCs fabricated on ITO in the Bolink group.

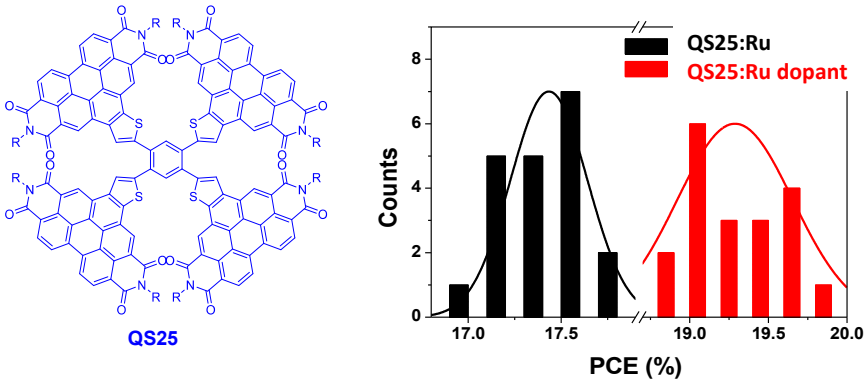


**Fig 38.** Structure of QS25 and PCE statistics (Yan group) for ITO/P3CT-Na/$MAPbI_3$/QS25:$(RuCp^*mes)_2$/$C_{60}$/BCP/Ag PSCs, showing effects of $(RuCp^*mes)_2$ doping.

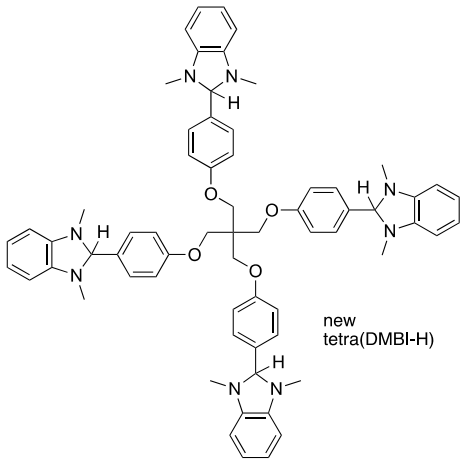


**Fig. 39.** Tetra(DMBI-H) dopant that loses four hydrides (the hydrogens explicitly shown) on thermal activation to form a tetracation, electrostatic interactions between which and the charge carriers introduced to a polymer host can lead to insolubilization.

## IV.4. Ionic Dopants for Perovskite Active Layers

In this last part of the project we have been investigating the impact of doping the perovskite films with different ionic dopants upon performance and stability of perovskite absorbers and solar cells. In Fig. 40, we show a schematic of the device structure, along with the chemical structure of some of the additives employed.

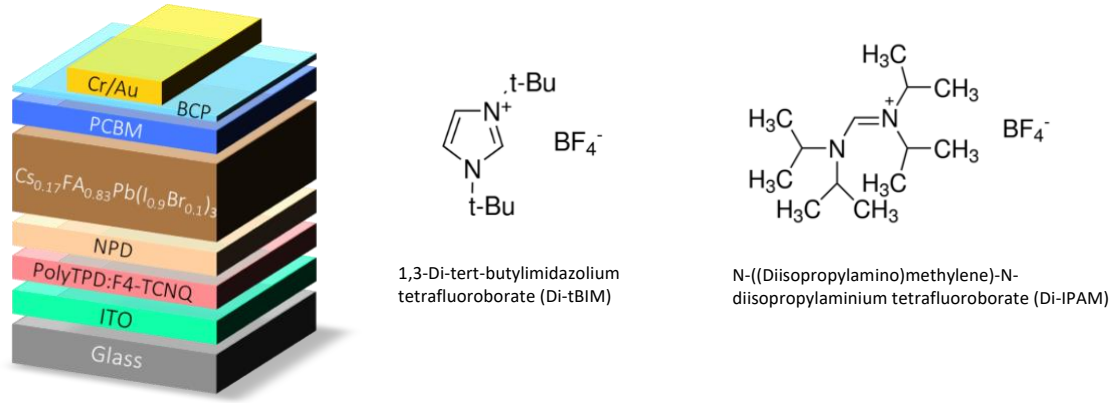


**Fig. 40.** Schematic illustration of the device structure employed and the composition of the perovskite absorber layer used. Middle and right) chemical structure of the ionic additives combined within the perovskite absorber layers.

We investigated a range of different size ions, as the ionic additives, and found that the precise choice of ions did impact whether the solar cell performance improved or not. In the examples given here, 1,3-Di-*tert*-butylimidazoliu tetrafluoroborate (Di-tBIM) delivered the most significant improvement in open-circuit voltage and efficiency, which we show in Fig.41.

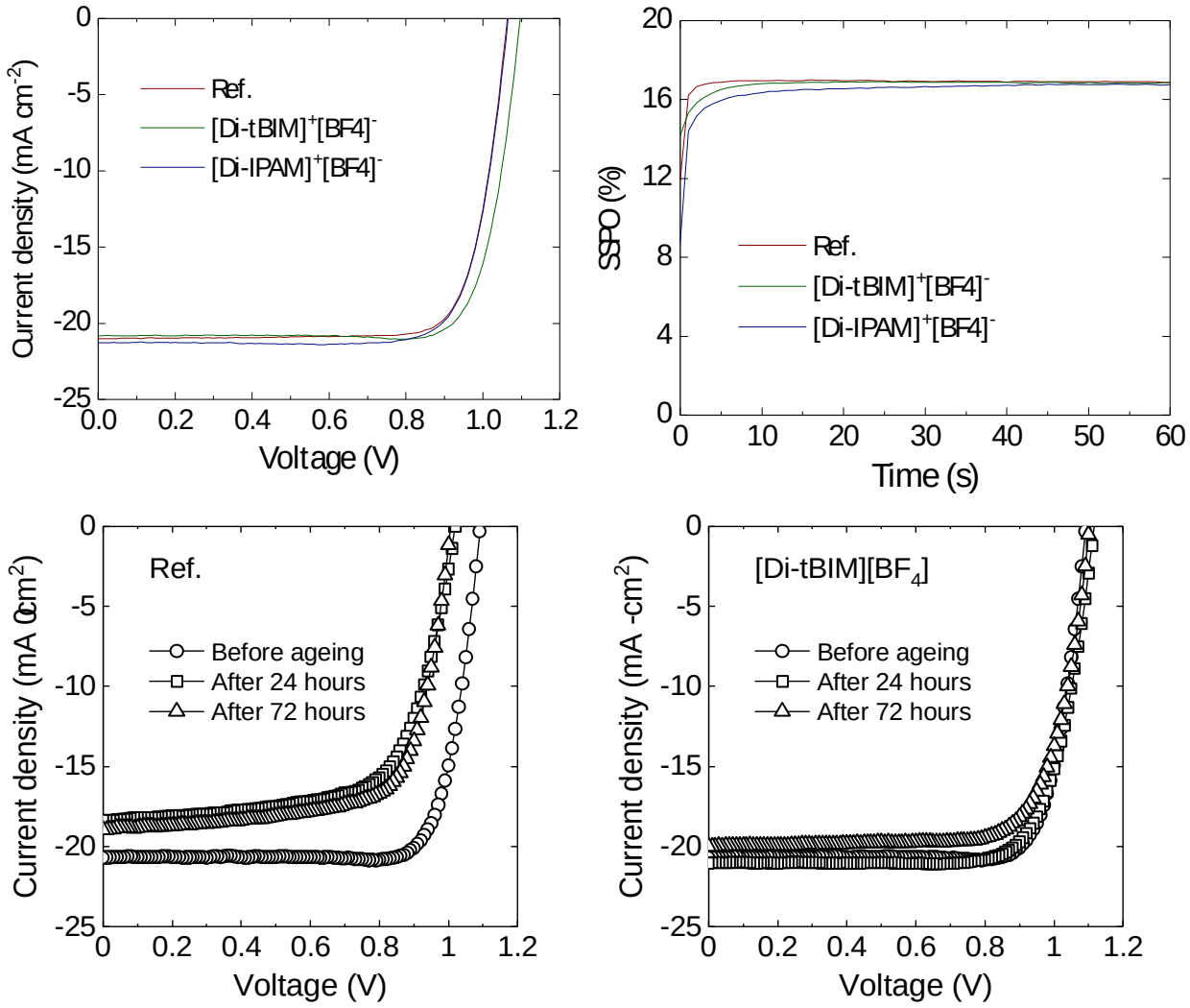


**Fig. 41.** Top left) current density voltage curves for perovskite solar cells illustrated in figure 1, measured under AM1.5 simulated sun light at 100mWcm$^2$, for reference cells ($J_{SC}$: 21.0 mA·cm$^{-2}$ ; $V_{OC}$:1.06 V; PCE: 18.2 % ; FF: 0.80 ) with Di-tBIM doping ($J_{SC}$: 20.8 mA·cm$^{-2}$ ; $V_{OC}$:1.10 V PCE: 18.9 % ; FF: 0.81) and with Di-IPAM doping ($J_{SC}$: 21.3 mA·cm$^{-2}$ ; $V_{OC}$:1.07 V; PCE: 18.3 % ; FF: 0.78). Top right) Steady-state power output (SSPO) for the different cells. Bottom) JV curves of PV cells tested under AM1.5 100mWcm$^{-2}$ simulated sun light, after different stressing times under full spectrum sun light at 85°C for control reference cells (left) and doped cells (right).

We further investigated the impact of the dopants upon long term stability under environment stressing factors. One of the key stress factors for perovskite solar cells is the combination of full spectrum sun light at elevated temperatures. In Fig. 41, we show the current voltage curves of reference cells and those doped with Di-tBIM at different times after aging at 85°C under full spectrum simulated sun light. In Table 3, we show the determined solar cell performance parameters.

**Table 3.** solar cell performance parameters for solar cells stressed for different lengths of time under 85°C one sun irradiance.

| Champion cell | Ageing | PCE (%) | $V_{OC}$ (V) | $J_{SC}$ (mA/cm$^2$) | FF |
|---|---|---|---|---|---|
| Ref. | Before | 17.83 | 1.06 | -20.57 | 0.80 |
| | 24 h | 12.88 | 1.02 | -18.37 | 0.70 |
| | 72 h | 13.87 | 1.01 | -18.96 | 0.70 |
| [Di-tBIM][$BF_4$] | Before | 18.51 | 1.09 | -20.69 | 0.80 |
| | 24 h | 18.20 | 1.12 | -21.03 | 0.75 |
| | 72 h | 16.88 | 1.10 | -20.00 | 0.74 |

## IV.5 Low-Dimensional Lead Halide Perovskites and Perovskitoids

Hybrid iodoplumbate perovskites and perovskitoids (Fig. 42) consist of catenated $PbI_6$ octahedra bearing an overall negative charge and positively charged organic cations. 3D examples have of course been used in highly efficient solar cells,[72-81] but other possibilities include light-emitting diodes and field-effect transistor lasers.[82, 83] Their limited moisture and heat stability has driven the interest in lower-dimensional hybrid perovskites and perovskitoids that, in addition to higher stability, offer structural versatility, prompting their use in a wide range of applications. Many have been synthesized and structurally characterized; for example, more than one hundred different organic cations have been successfully incorporated into 2D hybrid iodoplumbates, which have been used as the active layer for solar cells[72-81] and light emitting diodes.[82, 83] They can also be used as protective layers for 3D perovskites; see section 2.3 in which we use PEA-I (PEA = $PhCH_2CH_2NH_3^+$) as an interlayer, which may form a 2D phase or "quasi-2D" mixed-cation phase. Compared with their 3D counterparts they can offer superior stability and a much wider structural diversity, since the cation size is not limited by the interstitial volume of the lattice 3D lead iodide lattice. However, it is not well understood what structural features of the cation favor the formation of a 2D structure, and what features favor lower dimensional (1D or 0D) material. Development of reliable guidelines relating the cation's structure to the formation of different classes of low-dimensional hybrid perovskite and perovskitoid materials, would be highly desirable and would enable engineering materials with specific structures and properties. 1D perovskites, in the strict sense, consist of chains of vertex-sharing octahedra but haloplumbate examples, $A_3PbHal_5$ (A = organic cation, Hal = halogen), are relatively rare. On the other hand, reports of perovskitoids, where there are chains of octahedra sharing faces instead of vertices, which we will refer to here as 1D face-sharing iodoplumbates (FSIPs), $APbI_3$, are somewhat more numerous. Aspects of 1D materials studied include their visible light absorption,[84] high dielectric constant,[85] high photo-conductivity,[86, 87] luminescence,[88] and their use as potential photo or thermochromic,[89, 90] photocatalytic,[91] switchable dielectric,[90, 92-94] hybrid ferroelectrics,[88, 95-97] magnetic,[98] and third-order nonlinear optical (NLO)[99] materials. 1D $APbI_3$ have increased moisture and heat stability compare to 2D and 3D perovskites,[100, 101] with some examples even stable to immersion

in water.[102] This stability has led to the recent use of 1D $APbI_3$ compounds to protect 3D perovskite films.[103]

Overall our understanding of how the chemical structure of the organic cation affects the crystal structure of the resulting perovskite or perovskitoid is rudimentary. An improved understanding would be useful, not only in order to design low-dimensional materials for particular applications, but to help understand the possible effects and side products of using the relevant organic cations as additives or protective layers in 3D materials. We have, partly supported by this award and by a Canadian fellowship, conducted a number of investigations of this relationship.

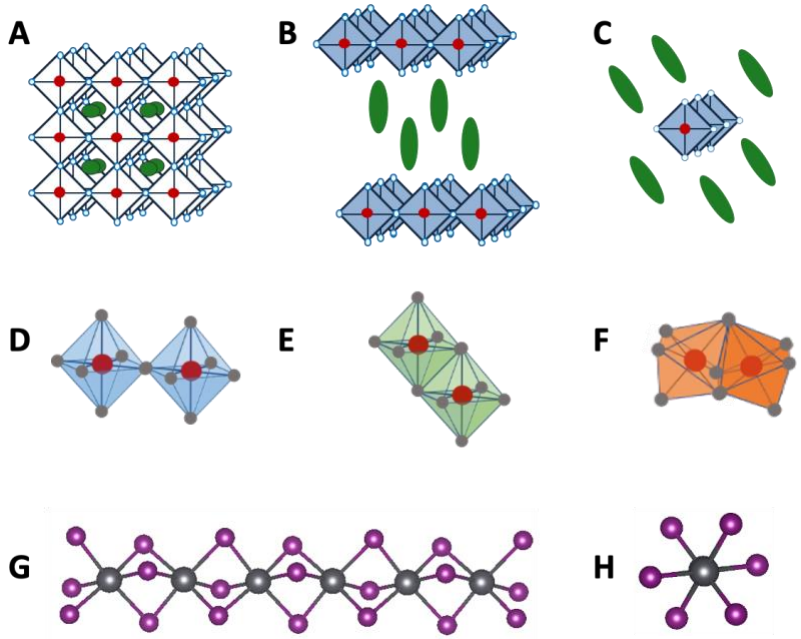


**Fig. 42**. Structural variation in perovskites and perovskitoids. Top: schematic structures of (A) 3D, (B) 2D and (C) 1D perovskites. Center: different connectivities of octahedra: (D) face-sharing, (E) edge-sharing, and (F) vertex-sharing. Bottom: representation of a 1D face-sharing wire where the wire propagation is in the axis (G) parallel or (H) perpendicular to the page.

*Layered Lead-Halide Perovskites*

In one study (#1 in section V.1)[104] – in collaboration with the groups of Aditya Mohite at Rice University, Mecorui Kanatzidis at Northwestern University, and Carlos Silva at Georgia Tech) – we reported the first example of a 3×3 corrugated 2D organic-Pb/I perovskite, $(4NPEA)_2PbI_4$ (4NPEA = 4-nitrophenylethylammonium) (Fig. 43). The nitro groups are involved in cation-cation and cation-iodide interactions. The structure contains both highly distorted and near-ideal $PbI_6$ octahedra, consistent with the observation of two $^{207}Pb$ NMR resonances, while the optical properties resemble those of other 2D perovskites with distorted $PbI_6$ octahedra.

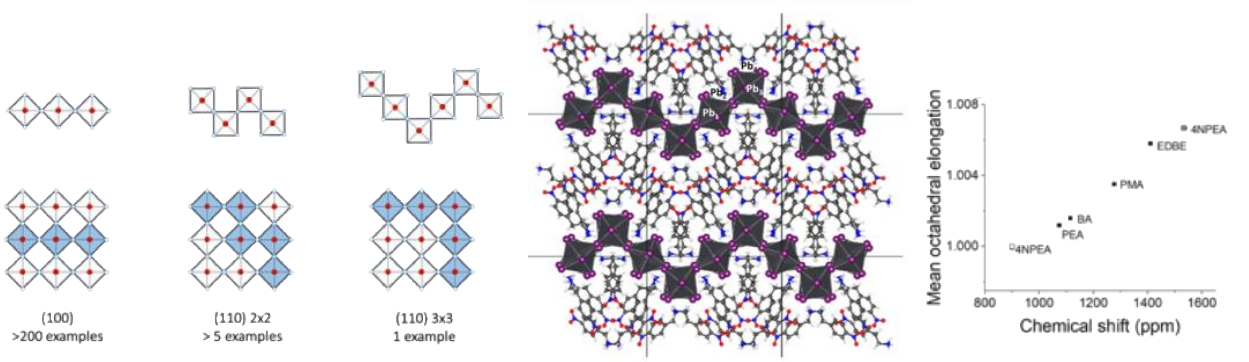


**Fig 43.** Left: schematic showing how 2D perovskite structures can be regarded as derived from "cutting" a 3D structure. Center: the (110) 3×3 structure of $(4NPEA)_2PbI_4$. Right: plot showing that the $^{207}Pb$ NMR chemical shift is related to the degree of distortion present in the $PbI_6$ octahedra of 2D perovskites. Note that the low chemical shift for $(4NPEA)_2PbI_4$ corresponds to the relatively undistorted Pb1 and Pb2 octahedra, whereas the high chemical shift corresponds to Pb3 and Pb4.

In another study (#5 in section V.1) we examined a series of 4-Y-$C_6H_4CH_2NH_3)_2PbI_4$ (Y = H, F, Cl, Br, I) structures (Fig. 44), which consist of single ⟨100⟩-terminated perovskite sheets separated by *p*-halobenzylammonium cations.[105] In analogy to their oxide counterparts, 2D hybrid organic-inorganic perovskites have been classified, in many cases, as either Dion-Jacobson (DJ) or Ruddlesden-Popper (RP) structures, where DJ and RP refer to the offset of successive inorganic layers from one another. Often (also following an analogy with oxides) the former are assumed to require an organic dication, whereas the latter are associated with monocations. We quantified the offset of the inorganic layers in this series to allow the structures of hybrid organic inorganic perovskite to be consistently related to these two structure types. In contrast to the previous RP structure of $(C_6H_5CH_2NH_3)_2PbI_4$, where the inorganic layers are offset from one another, the Y = F, Cl, and Br examples tend towards the DJ structure in which successive layers eclipse one another, despite the use of an organic monocation. Close Y···I approaches suggests that halogen bonding plays a role in these structures. Use of Y = I, for which stronger halogen bonding is expected and is also suggested by a more linear C–Y···I angle, results in a RP-like structure. We also showed that several previously reported structure also have DJ-like stacking despite incorporating monocations and whereas the use of a dication does not guarantee ideal DJ stacking. The optical properties of the series show relative minor variations, consistent with the large interlayer spacings and highly distorted Pb-I-Pb angles found in each case.

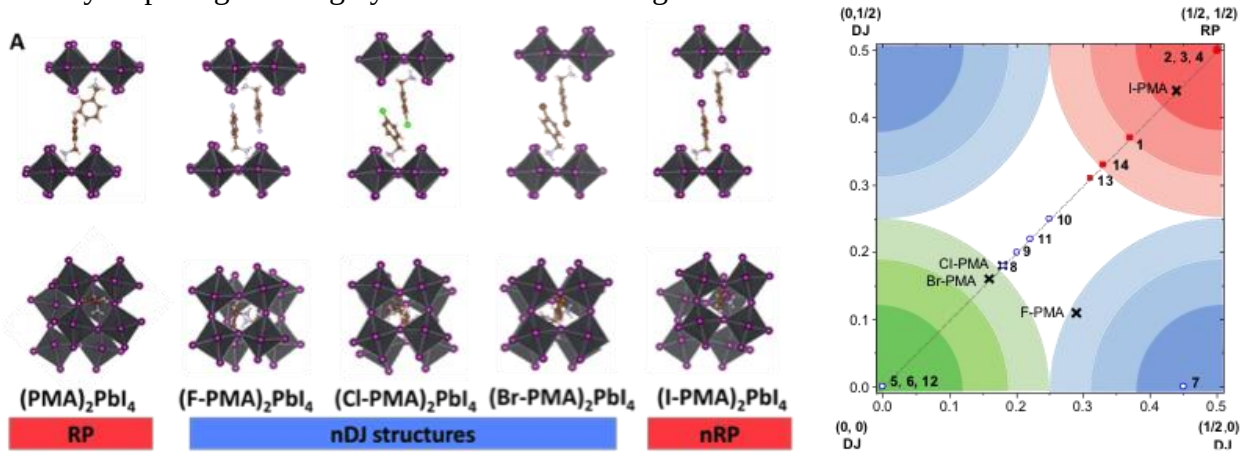

**Fig. 44.** Left: figures showing the stacking of successive inorganic layers in the structures of 4-Y-$C_6H_4CH_2NH_3)_2PbI_4$ (Y = H, F, Cl, Br, I). Right: offsets of the organic layers in the two Pb–I–Pb directions for 4-Y-$C_6H_4CH_2NH_3)_2PbI_4$ and other structures from the literature. Note the offsets 0,0 and ½,0 are considered DJ and ½,½ RP. Compounds **9**, **11**, and **12** also incorporate monocations yet have DJ or DJ-like stacking (not recognized in the original publications).

In another study (#8 in section V.1),[106] we investigated the structure and optical characteristics of 2D $A_2PbI_4$ materials with aromatic A cations of increasing width. Cations used include PEA (2-phenylethylammonium), dF-PEA (2-(3,5-difluorophenyl)ethylammonium), dCl-PEA (2-(3,5-dichlorophenyl)ethylammonium), dBr-PEA (2-(3,5-dibromophenyl)ethylammonium), and dMe-PEA (2-(3,5-dimethylphenyl)ethylammonium). In all cases, we obtained $PbI_4^{2-}$ layers of corner-sharing octahedra separated by bilayers of the organic cations (Fig. 45).

Multiple cation-cation interactions can be found in these HOIPs single crystals. For dF-PEA and dCl-PEA, the benzene rings from the two different organic layers are found to lie on top of each other. The distance between the centroid of one benzene to the plane made by another benzene is 3.343 Å for Y = F and 3.508 Å for Y = Cl, which could arise from a dipole-dipole interaction between the two cation. In the case of dBr-PEA, there is a close approach between the bromine atoms from the two layers. This may be due to a Br···Br van der Waals interaction. A close approach between the methyl groups is also seen for dMe-PEA.

Fig. 46A shows the Kubelka-Munk transformation of the diffuse reflectance of the different HOIP powders and indicate the presence of two distinct bands. The energy of the high-energy peak is assigned to the exciton band energy (see Fig. 46A). As expected, there is a linear relationship between the Pb−I−Pb angle and the exciton energy; the exciton band is red shifted by ca. 100 meV from dBr-PEA to dF-PEA (see Fig. 46B).[108] The relationship between the Pb–I–Pb angle and the band gap in 3D HOIP[109-113] or with the exciton band energy in 2D HOIPs[79, 108, 114-117] has been observed in many instances. It was shown that, in 3D HOIPs, band gap significantly opens upon octahedral tilting, mainly as a result of a decrease of the overlap integral.[110] Since trends in the exciton energy often closely follow those in the band gap, this rule can be extrapolated for the exciton energy of 2D HOIPs.

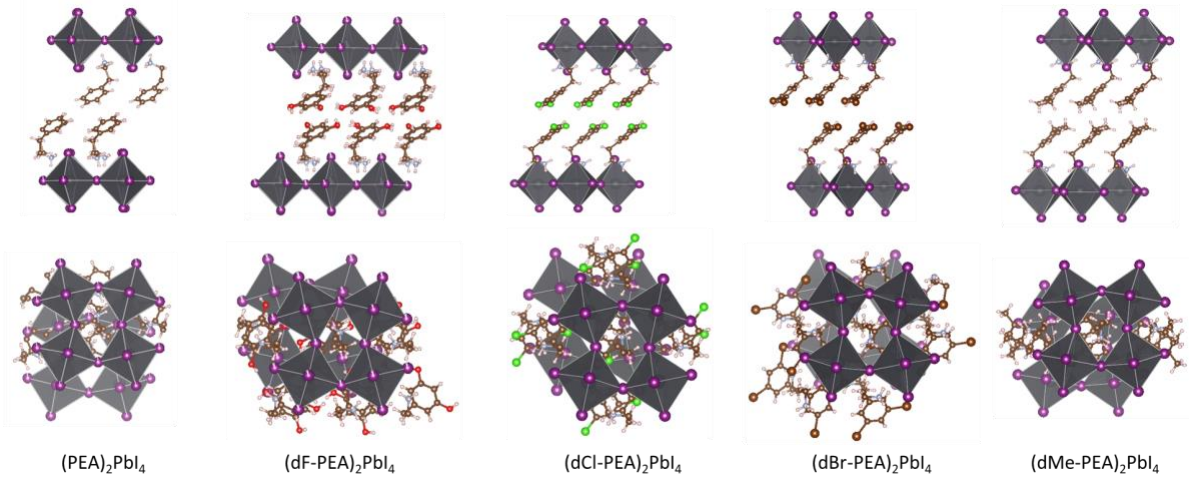

**Fig. 45.** Crystal structures of $(dY\text{-}PEA)_2PbI_4$, Y = H, F, Cl, Br, Me, viewed along the plane of the inorganic sheet and after + 90° rotation around the long in-layer axis. The structure of $(PEA)_2PbI_4$ is taken from the literature.[107]

There is also a linear trend between the Pb–I–Pb angle and the width of the cation (see Fig. 46C). What emerges, based on these 5 compounds, is that, even if the reference compound (PEA, smallest cross-section size) does not follow the trend, that the width of the cation is a *fair* indicator of the Pb–I–Pb of the HOIPs.

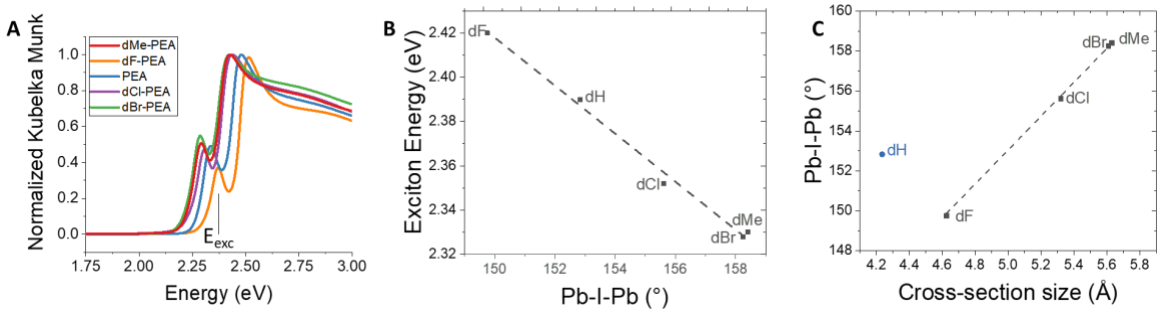


**Fig. 46.** (A) Normalized Kubelka-Munk transform of diffuse reflectance data for the different HOIPs powders (with exciton energy, $E_{exc}$, indicated for the example of $(dF\text{-}PEA)_2PbI_4$). (B) Relationship between the exciton energy and the Pb–I–Pb angle. (C) Relationship between the Pb–I–Pb bond angle and the width (calculated from the MM2-minimized geometry of the cation in Chem3D) (dH is excluded from the fit). The width of dMe-PEA is calculated as the average of the three longest H-H distances of the methyl.

In order to establish whether this trend holds true for cations other than 3,5-disubstituted PEAs, we extended the study to other families of cations (see Fig. 47). First, we synthesized *meta*-substituted phenylethylammonium-based HOIPs (3Y-PEA, where Y = Cl, Br, Me) and determined the structures. Again, the Pb–I–Pb bond angle is linearly proportional to the width. Moreover, data for three compounds fit the same linear plot between the exciton energy and the Pb–I–Pb bond angle as the dY-PEA derivatives discussd above (see Fig. 47B).

We then examined additional structures available from literature reports. *para*-Substituted phenylethylammonium-based perovskites (in which the cross-section size is constant) have similar Pb–I–Pb bond angles ($A_2PbI_4$ where A = PEA 152.9°,[107] 4F-PEA 151.5°,[118] 4Cl-PEA 152.48°,[118] 4Br-PEA 152.15°,[118] 4Ph-PEA 153.1°,[119] 4Cl-Ph-CH($CH_3$)$NH_3$ 152.7°[120]), reinforcing the hypothesis that cross-section size is an important factor in determining the Pb–I–Pb bond angle, although the data points for these derivatives do not fall on the same line as the disubstituted and *meta*-substituted derivatives. $A_2PbI_4$ perovskites for A = TMA[121] and TEA[122] cations (TMA = 2-(2-thienyl)methylammonium, TEA = 2-(2-thienyl)ethylammonium), which have the same cross-section size but different alkyl length, have similar Pb–I–Pb bond angles to one another, but larger than one would expect based on the trend in the disubstituted and *meta*-substituted compounds. On the other hand, Pb–I–Pb angle and cross-section size data for $A_2PbI_4$ perovskites based on several other cations including 2-(naphth-2-yl)ethylammonium (NEA),[107] 2-(1-cyclohexenyl)ethylammonium (CycEA),[123] 2-fluorophenylethylammonium (2F-PEA)[124] and 2-(3-fluorophenyl)ethylammonium (3F-PEA)[125] do lie close to the line defined by the $(dY\text{-}PEA)_2PbI_4$ derivatives (and other $(3Y\text{-}PEA)_2PbI_4$ derivatives) reported here.

There are cases of families of 2D $A_2PbI_4$ structures reported in which the cross-section and Pb–I–Pb angle do not linearly correlate: (1) when the two layer of cations interpenetrate one

another, instead of being separated in two sheets (*para*-substituted PMAs);[114] (2) when the 2D structure is not planar, but corrugated instead (as in the case of A = 2-(4-nitrophenyl)ethylammonium);[126] and (3) when the core of the cation is much larger than that of 2-(phenyl)ethylammonium (pyrene and perylene derivatives).[127-37]

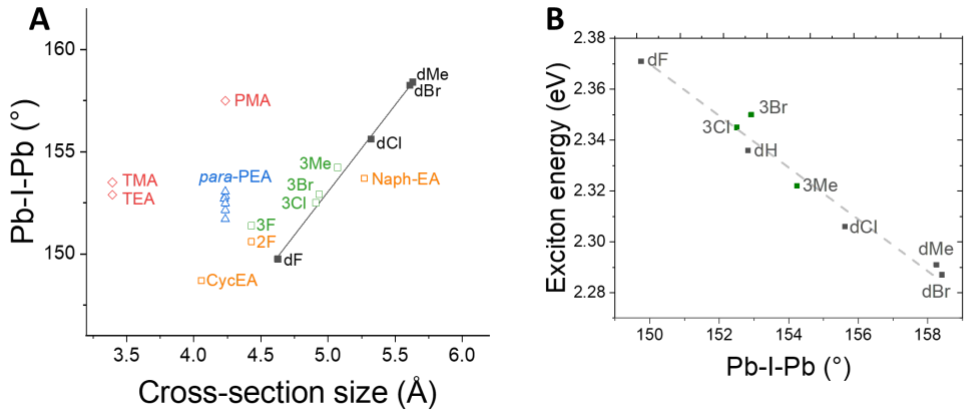


**Fig. 47.** Relationship between the Pb−I−Pb bond angle and the cross-section sizes (Y-Y distance calculated from the MM2-minimized geometry in Chem3D). The Pb−I−Pb bond angle of 2F-PEA, 3F-PEA, 4F-PEA, 4Cl-PEA, 4Br-PEA, 4Ph-PEA, TMA, TEA, NEA, CycEA, PMA were calculated using the reported crystallographic data. The red diamonds are compounds that don't follow the hypothesis. The blue (*para*-PEA), black (dY-PEA), green (3Y-PEA) and yellow (others) compounds represent different families of compounds and follow the hypothesis.

In summary, we reported a total of 7 new 2D HOIPs containing 1,3-disubstituted-phenylethylammonium cations, dY-PEA (Y = F, Cl, Br, Me) and 3-substituted-phenylethylammonium cations, 3Y-PEA (Y = Cl, Br, Me). We were able to demonstrate that, at least for some limited series of compounds, the width of the cation influences the distortion of the inorganic sheet through Pb−I−Pb bond angle variation, which leads to a variation of the exciton energy. Due to the complexity of these structures, the mechanism by which width affects angle is not entirely clear. Indeed, the fact that it is not universally applicable reflects that it cannot be straightforward. However, modifying the steric demands of the cation "tail" necessarily affects the packing in the organic interlayer, and thus places demands on the inorganic layer. This is unlikely to be a universal indicator; multiple factors must be taken into account, but it brings us closer to developing an understanding between the structure of the organic cation and the structure of the corresponding 2D HOIP. The deviations observed from the proposed relation may afford insight into other descriptors that could be looked at in the future.

*Lead halide Materials Forming Lead-Halide Chains*

As noted above 1D perovskitoids, such as those consisting of chains of face-sharing $PbI_6$ octahedra (which will henceforth refer to as face-sharing iodoplumbates, FSIPs), have a number of useful and interesting characteristics. To date there exists no reliable general strategy for ensuring formation of 1D FSIPs, beyond the use of bulky cations lacking hydrogen-bond donor groups. Although it has been recognized that synthetic conditions affect the crystal structure obtained, no guidelines for using primary ammonium-based cations to engineer the structure have been proposed yet.[128-130] We were interested in how the choice of different ammonium cations of the general type $R(CH_2)_nNH_3^+$ (R = aryl, substituted cyclohexyl; n = 1, 2) can be used to engineer 1D FSIP crystals (Fig. 48). This study (not yet published, although a manuscript is under revision, #13 in section

V.1) involved collaboration with the groups of Ruth Pachter at AFRL (quantum-chemical calculations, an interaction initiated by Marder's visit to AFRL), Nathan Jui (Emory, synthesis of some of the amines used), and Tatiana Timofeeva (New Mexico Highlands University, crystallography).

To test whether intra- or inter-cation hydrogen bonding between an ammonium group and a HBA is a general approach that favours the formation of FSIPs, we set out to examine a wide variety of structures in which the ammonium cation is based on a six-membered ring (primarily benzene, but also including a naphthalene and a cyclohexane derivative) is 1,2- or 1,3-functionalized with both a methylammonium ($CH_2NH_3^+$) or ethylammonium ($(CH_2)_2NH_3^+$) group and a moderate-to-strong HBA (CN, $NO_2$, OMe, $CO_2Me$, F, OMs [$OSO_2Me$], OH), as shown in Fig. 48. In addition, we examined several examples of cations containing substituents with similar steric bulk, but weak (Cl, Br, $CF_3$), or no HBA character (Me). Unsubstituted PEA, PMA and NEA are known in the literature and all form 2D HOIPs when synthesized in these conditions. Moreover, *para*-substituted PEA ions, where no intramolecular hydrogen bonding is possible, form 2D structures when the same substituents are used (CN, $NO_2$,[126] OMe,[131] $CO_2Me$, Me[118]).

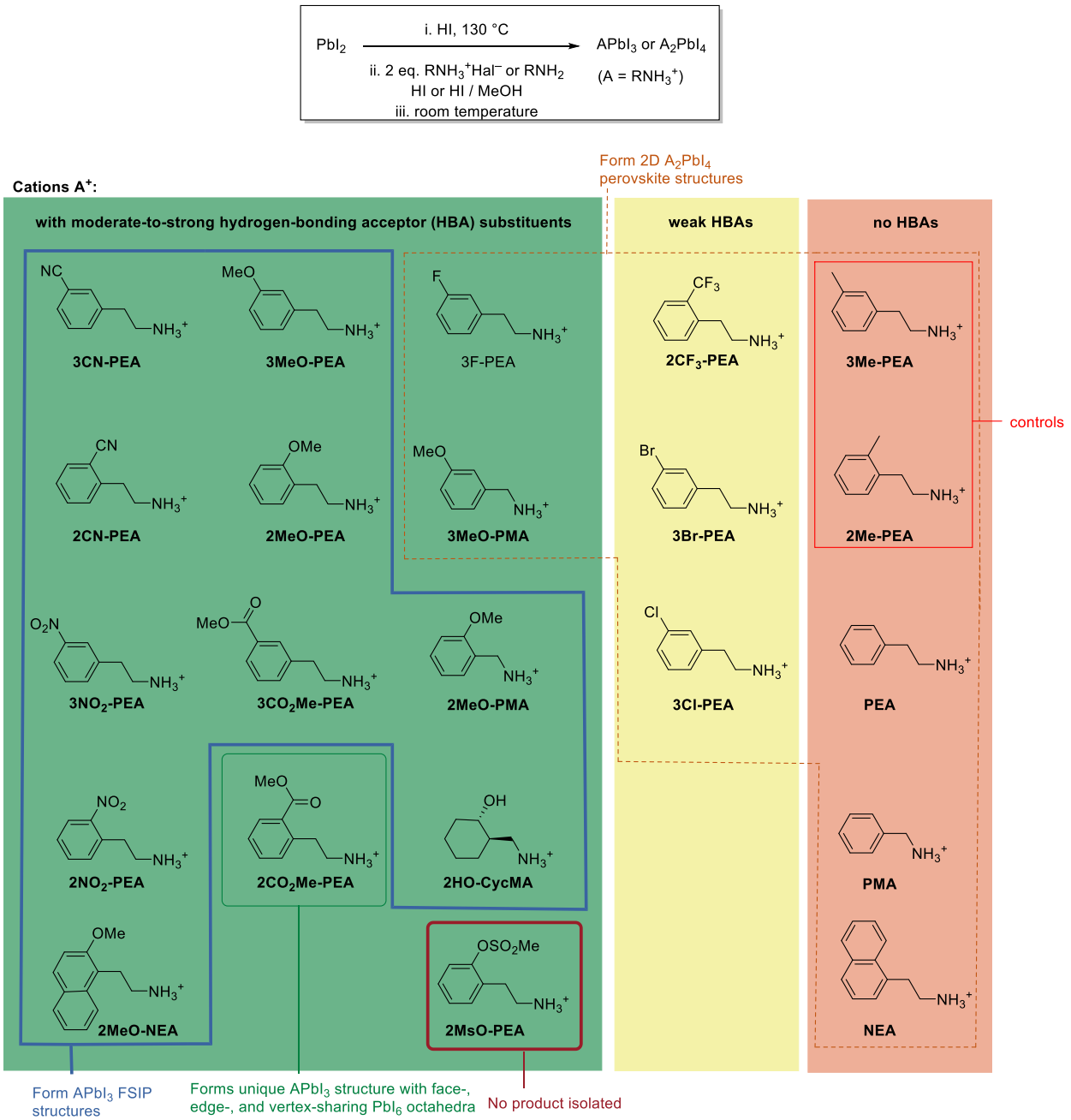


**Fig. 48**. Top: general synthesis of hybrid organic-inorganic materials used in this work. Bottom: structures of cations employed, and structure types obtained. The use of cations in bold in HIPC synthesis has not previously been reported, while HIPCs derived from 3F-PEA,[132] 3Cl-PEA, 3Br-PEA, PMA[133] and NEA[107] are reported in the literature.

Most of the ammonium salts, or corresponding amines used in our study were available commercially or through literature syntheses. However, to broaden the range examined, several new derivatives (2MsO-PEA-Cl, 3CN-PEA-Cl, 2CN-PEA-Cl, 3$CO_2$Me-PEA-Cl, 2$CO_2$Me-PEA-Cl, 3Me-PEA-Cl, 2Me-PEA-Cl) were synthesized according to a recently developed procedure.[134] We used conditions commonly used to synthesize 2D HOIPs, i.e., slow crystallization of mixture of solutions obtained by dissolving $PbI_2$ in HI and by dissolving the halide salt of the cation (or the corresponding neutral amine) in HI,[75, 79, 115, 126, 135, 136] and investigated the purity and structure

of the resulting crystalline materials using single-crystal X-ray diffraction (SC-XRD), powder XRD (PXRD), and elemental analysis. Fig. 48 summarizes the cations employed and the structure types obtained. Of the fourteen cations examined that bear moderate-to-strong HBA substituents, ten of the resulting hybrid organic-inorganic structures were found to be 1D $APbI_3$ FSIPs, i.e., linear $PbI_3^-$ wires composed of face-sharing octahedra separated by layers of organic cations. Of the remaining four structures, $2CO_2$Me-PEA forms a highly unusual $APbI_3$ structure in which there is face-, edge-, and vertex-sharing by the $PbI_6$ octahedra (see SI for further description and discussion), while 3MeO-PMA and 3F-PEA form a $A_2PbI_4$ 2D perovskite. In the case of 2MsO-PEA, no solid product was formed. When the substituents have little or no HBA character, but similar bulk as those described previously, 1D FSIPs are not formed under the same conditions.

In two cases – 2MeO-PEA and 3MeO-PEA – 2D materials (identified as such by their PXRD patterns) could also be obtained instead of 1D FSIPs when higher concentrations of reagents were used. This is not particularly surprising, since other examples in which the structure of hybrid materials depend on the concentration employed have been reported in the literature.[137] Nevertheless, for 2MeO-PEA the thermodynamic product is still apparently the 1D FSIP; 2D $(2MeO\text{-}PEA)_2PbI_4$ was observed to transform to 1D $(2MeO\text{-}PEA)PbI_3$ on standing at room temperature over a timescale of days using the PXRD (presumably with loss of $A^+I^-$).

In each of the FSIP structures, there is hydrogen bonding between the ammonium moieties and the HBA, either intermolecular and forming chains of hydrogen-bonded organics (see Fig. 49A), intermolecular and forming dimers (Fig. 49B), or intramolecular (Fig. 49C). We suggest that it is these interactions that promote formation of a 1D structure, rather than a 2D layered perovskite. While $R\text{-}NH_3\cdots I$ close contact are present in certain cases, the intra- or intermolecular H-bonding present between cations prevent the ammonium substituent to penetrate the half-cubooctahedral "pocket" of a 2D HOIP.

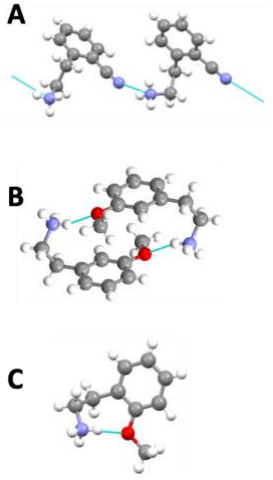


**Fig. 49.** Type of hydrogen bonding found in the FSIP: examples of (A) linear, (B) close pair, (C) intramolecular hydrogen bonding taken from the structures of 3CN-PEA, 3MeO-PEA, and 2MeO-PEA, respectively.

The ten new FSIP structures referred to above, and their comparison to previously reported structures, enables us to further classify these materials into different families based on their structural characteristics. 2D HOIP structures are often classified based on the type of cation used and/or the offset of the inorganic layers from one another as Ruddlesden-Popper or Dion-Jacobson

structures. For 1D structure, to the best of our knowledge, no comparable classifications have been suggested in the literature. The geometries of the wires themselves show little variation. However, FSIP structures do fall into several groups, based on the relation between neighboring wires.

In many cases, all the $PbI_3$ chains are crystallographically equivalent; when viewed along the chain direction these structures from a roughly square, rectangular, or rhombic lattice of chains. We have designated as a W structure type when all the wires are related only by translation operations; multiple examples are found in the literature[89, 138-140] and several structures reported here belong to this class (Fig. 50A; A = 2HO-CycMA, 2MeO-PEA, 3CN-PEA, 3MeO-PEA, $2NO_2$-PEA). Other FSIPs have wires related by operations other than translation. We have designated the situation of two crystallographically equivalent wires W and W' (where the "middle" wire, W', is related to the "corner" wires, W, by translation *and* rotation), in which, when viewing along the chain direction, W' falls roughly in the center of four W wires (and vice versa) as W:W' (see Fig. 50B).[141, 142] In other cases, two crystallographically equivalent wires W' can be in the center of four W wires and we have used the label W:2W'.[88, 143, 144] Moreover, there are also exceptions that do not fall within these categories.[145-147] For example, $(3NO_2\text{-PEA})PbI_3$ has two crystallographically inequivalent wires in its unit cell and, therefore, cannot be described in the same way as the examples above.

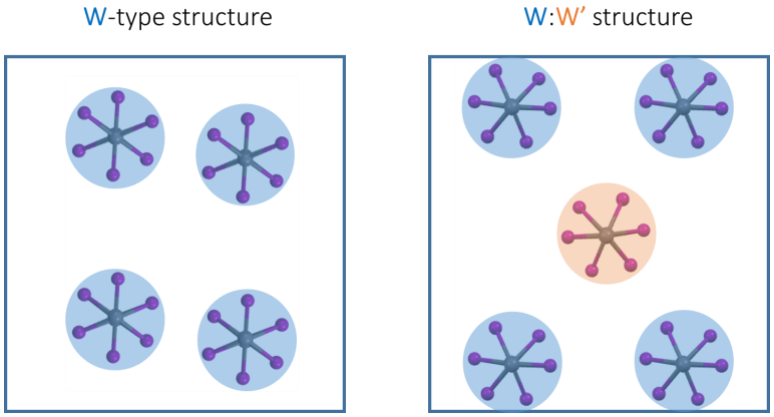


**Fig. 50.** Schematic representation of W (left) and W:W' (right) structure of 1D FSIPs. The different color shown for the central chain of the W:W' structure indicates a crystallographically equivalent chain related to the corner ones by translation and rotation.

The photophysical properties of the HOIP films were investigated by UV−vis spectroscopy (see Fig. 51). The exciton energy, $E_{ex}$, was in each case estimated using the maximum of the low-energy peak. Overall, there is little variation in the optical properties of the materials examined here. For the W-type structures, all compounds have similar exciton energy (3.26 eV) (see Fig. 51C). However, among the W:W' structures, $(2MeO\text{-}NEA)PbI_3$ and $(2CN\text{-}PEA)PbI_3$ have exciton energies at lower energy (3.06 eV) than those of $(3CO_2Me\text{-}PEA)PbI_3$ and $(2MeO\text{-}PMA)PbI_3$ (3.26 eV, see Fig. 51D). Different crystal structure characteristics were examined for possible correlation with this variation in exciton energy. Variation in the inter-chain distance is, at least in principle, expected to affect the quantum-confinement of the exciton within the wire. However, the exciton energy is constant for W-type structures regardless of the closest interwire distances, likely because these distances are sufficiently long that the excitons are well confined in all the structures. Indeed, for the W:W' type structures, $(2MeO\text{-}NEA)PbI_3$ and $(2CN\text{-}PEA)PbI_3$, in which there is a larger interwire distance, the exciton bands are red shifted compared to those of $(3CO_2Me\text{-}$

PEA)$PbI_3$ and (2MeO-PMA)$PbI_3$ (in which the interchain distance is relatively short), the reverse of what is expected on exciton-confinement grounds.

The distortion of the $PbI_6$ octahedra from ideal geometry also correlates well with the exciton energy of 3D and 2D perovskites, with the Pb–I–Pb bond angle often being found to be a good indicator of the optical gap. For the 1D wires, we considered that the smallest I–Pb–I angle might be important distortion parameter, since this is largely responsible for the distortion in the wire axis direction. However, there is no clear correlation between the exciton energy and this angle.

The one criterion that seems to be related to the exciton energy is the position of the W' wire in the W:W' structures; the W' wire can either be aligned more-or-less symmetrically in the middle of the four W wires or in a significantly asymmetric way (see Fig. 51E). The two pseudo-centered W:W' structures have an exciton band red-shifted compared to the other two structures. However, more structures are needed to understand the generality of this observation, and it is not clear to us why this arrangement should afford a red shift. For the W structures, it seems that, in the absence of charge transfer between the inorganic and organic components found where the organic cation is an electron acceptor, the exciton energy is constant regardless of structural modifications. Indeed, other W-type structures where charge transfer was observed have orange to black color.[84, 88, 148, 149]

To further analyze the consequences of the structural difference between W and W:W' type structures, we investigated one example of each, W structure, 2MeO-PEA, and a W:W' structure, 2CN-PEA, using density functional theory (DFT) calculations, including spin-orbit coupling (SOC). A good agreement between the experimental and the computationally optimized structures was obtained, as expected. The band structures and projected density of states (PDOS) were calculated at the HSE06+SOC level of theory. The *k* paths are shown in Fig. S52. For 2CN-PEA, the inorganic 1D wires are oriented along the $Y_2\Gamma$ direction, where the inorganic parts are stacked. Therefore, stronger band dispersions are expected in the Γ-A, E-Z-$C_2$, and $Y_2$-Γ segments due to stronger interactions in 1D $[PbI_3]^-$ wire, and weaker dispersions in the Γ-Z-D-B-Γ, A-E, and $C_2$-$Y_2$ segments due to weaker van der Waals interactions between the organic cations (see Fig. 52A). For 2MeO-PEA, the inorganic wires run along the Γ-Z direction. Stronger band dispersions are thus shown for the Γ-Z, D-B, A-E, and $C_2$-$Y_2$ segments, and weaker dispersions for the Z-D, B-Γ, and E-Z-$C_2$ segments (see Fig. 52B). The PDOS for 2CN-PEA indicate strong band hybridization near the bottom of the conduction band, but no hybridization near the top of the valence band (Fig. 52A, right panel). On the other hand, the PDOS for 2MeO-PEA show strong band hybridization both near the bottom of the conduction bottom and the top of the valence band (Fig. 52B, right panel). We note that hybridization generally tends to decrease band dispersions in the inorganic framework. The band gap for 2NC-PEA occurs at Γ and has a magnitude of 3.13 eV, and the band gap for 2MeO-PEA occurs at A and has a value of 3.45 eV. These show the same trend as the measured exciton energies of 3.06 eV for 2CN-PEA and 3.26 eV for 2MeO-PEA, respectively.

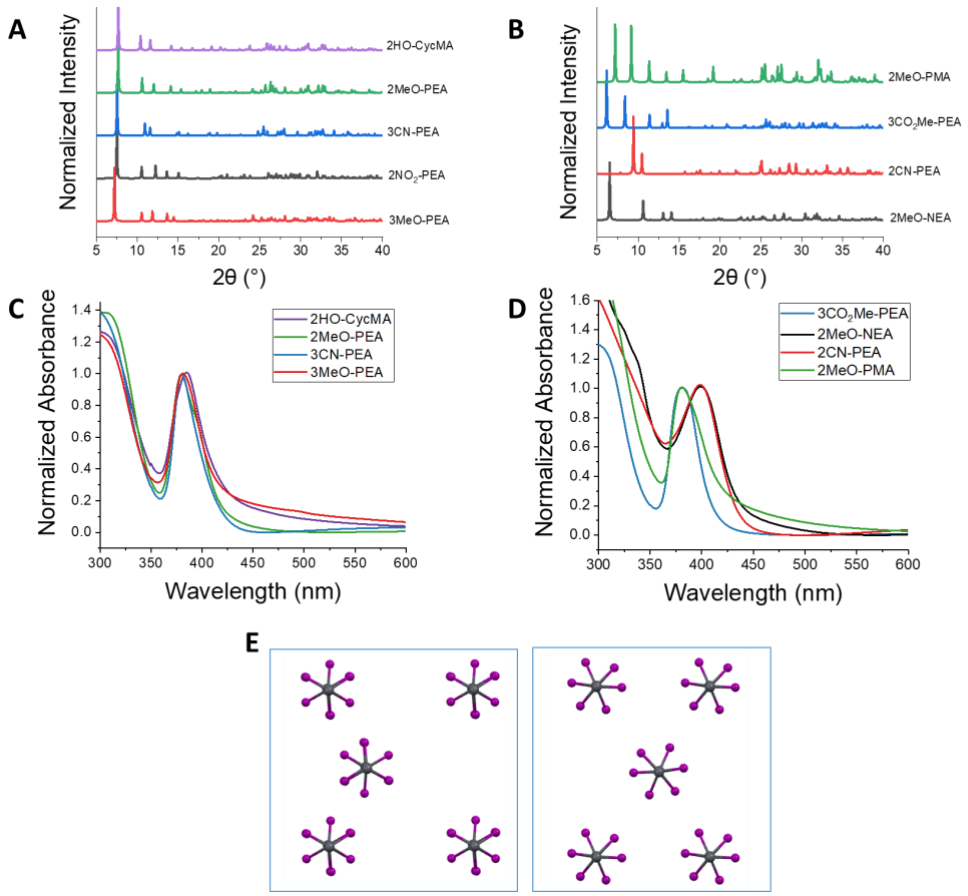


**Fig. 51**. PXRD of the 1D FSIP W (A) and W:W' (B) structures. Absorbance of FSIP films on glass: W (C) and W:W' (D) structures. (E) Wire arrangement in W:W' FSIP when the W' wire is unsymmetrically (left, $3CO_2Me$-PEA shown here, 2MeO-PMA is similar) and symmetrically (right, MeO-NEA shown here, 2CN-PEA is similar) located in the middle of the W wires.

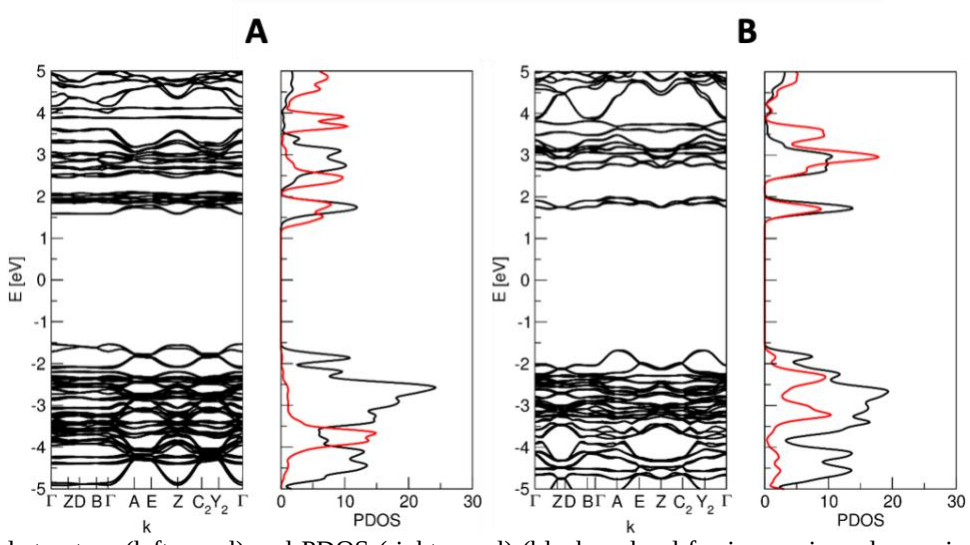


**Fig. 52.** Band structure (left panel) and PDOS (right panel) (black and red for inorganic and organic components, respectively) for 2CN-PEA (A) and 2MeO-PEA (B).

In summary, hybrid lead iodide materials incorporating $R(CH_2)_nNH_3$ (n = 1, 2; R = aryl, substituted cyclohexane) cations show a strong tendency to adopt a FSIP structure where hydrogen bonding interaction between the cation and itself or neighboring cations is possible. Considering the potential applications of this class of materials, including their use as capping layers to improve the long-term stability of 3D perovskite solar cells, some ability to predict the tendency to form a FSIP rather than a 2D perovskite is significant. Adding more structures to this family of compound could help further understand the optical properties of this class of materials.

We have also collaborated with Shijun Sun (MIT) on the use of ammonium halide salts that form 1D chains with $PbI_2$ as protective layers for 3D perovskites (Fig. 53). Machine learning is being used by Sun to establish the descriptors that enable one to identify which materials form the best protective layers. A manuscript is currently under preparation.

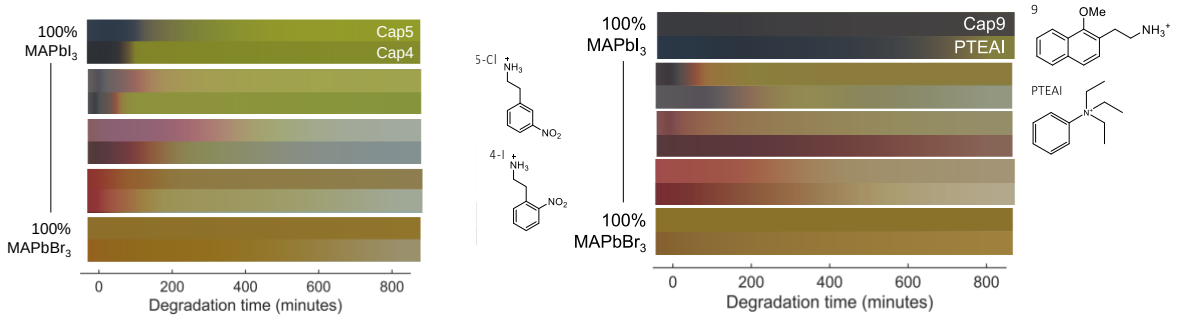


**Fig. 53.** Examples of stability studies of 3D perovskites using 1D-material-forming halide salts. Darker regions indicate retention of the 3D phase. The left panel indicates that despite similar chemical structures, two isomers of nitrophenylethylammonium have different impacts on stability and, moreover, that these impacts depend on the composition of the 3D material. The right panel shows one material ("9") can, depending on the 3D material, outperform PTEAI, which is one of the best materials examined to date for this application.

Low-Dimensional Lead-Halide Materials Incorporating Naphthalene Diimide-Based Cations

An attractive feature of 1D, and to a lesser extent, 2D perovskitoids, is that they can incorporate a much greater diversity of cations than 2D and 3D perovskites, opening the possibility of introducing new properties to the HIPC. The naphthalene diimide (NDI) moiety has been incorporated into a number of HIPCs,[150-152] all of these NDI-iodoplumbates showed absorption spanning the visible part of the spectrum. We set out to examine the structures and properties that could be obtained using the 2,2'-[naphthalene-1,8:4,5-bis(dicarboximide)-*N,N*'-diyl]-bis(ethylammonium) dication (NDIC2).[153] This work involved collaboration with the groups of Oanu Jurchescu at Wake Forest University (electrical measurements) and Tatiana Timofeeva at New Mexico Highlands University (crystallography) and has now been published (#7 in section V.1).[153] In addition, we have also collaborated with the group of Ted Sargeant at the University of Toronto on the use of the same dication in combination with methylammonium and formamidinium cations and study of the resulting materials with transient absorption measurements (also now published, #9 in section V.1).[154]

Reaction of $(NDIC2)I_2$ and $PbI_2$ in ca. 2:1 molar ratio in either NMP or DMF, followed by different crystallization conditions, resulted in four materials of general formula $(NDIC2)_xPb_yI_{2(x+y)}S_z$ (S = DMF, NMP) (**1-4**, Fig. 54), each of which has been characterized by single-crystal X-ray diffraction (SCXRD). Additional materials (**5-8**) were obtained by subsequent treatment of these initially formed materials (again, as shown in Fig. 53). The formation of a large number of different

materials emphasizes the great structural diversity achievable in organic haloplumbates. In the present study, the cation is always the same, yet multiple structures are still obtained. As in some previous studies,[150, 151, 155] the specific solvent also strongly affects the crystallization; indeed, as discussed below, **1-5** and **8** all incorporate solvent.

The crystal structure of **1** (Fig. 55) reveals a 1D material consisting of: zigzag wires of formula $[Pb_5I_{14}(DMF)_2^{4-}]_n$, in which DMF molecules are coordinated through oxygen to some of the Pb centers; $NDIC2^{2+}$ dications that bridge adjacent wires; and additional uncoordinated DMF molecules.

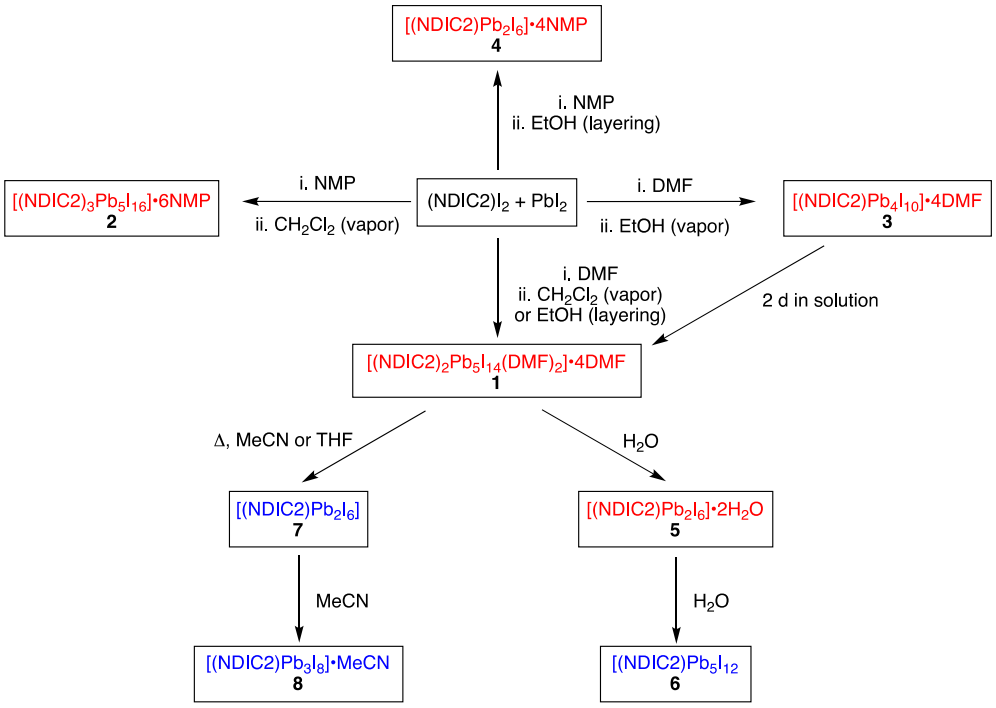


**Fig. 54.** Synthesis of NDIC2-containing perovskitoids obtained. The formulae shown in red were established through single-crystal structure determinations, while those shown in in blue were deduced based on elemental analysis and PXRD. For simplicity, the equations are not balanced; in principle, each reaction can be balanced by loss of either $PbI_2$ or $(NDIC2)I_2$, in addition to loss or gain of solvent molecules.

The wires contain three crystallographically distinct lead environments – two types of $PbI_6$ octahedra and $PbI_5(DMF)$ octahedra – in a 1:2:2 ratio. The main chain is defined by the two types of $PbI_6$ octahedra, with the $PbI_5(DMF)$ octahedra fused to the sides of the chains. The first of the two types of $PbI_6$ octahedra shares two of its faces with $PbI_6$ octahedra of the second type, while two of its vertices are also shared with two $PbI_5(DMF)$ units. Each $PbI_6$ octahedron of the second type each share a face with one of the first type, an edge with another $PbI_6$ of the second type, another edge with a $PbI_5(DMF)$ unit, and a corner with another $PbI_5(DMF)$ unit. Each $PbI_5(DMF)$ moiety shares two adjacent edges with $PbI_6$ units of the second type, with one of those edge iodides being further shared with a $PbI_6$ of the first type.

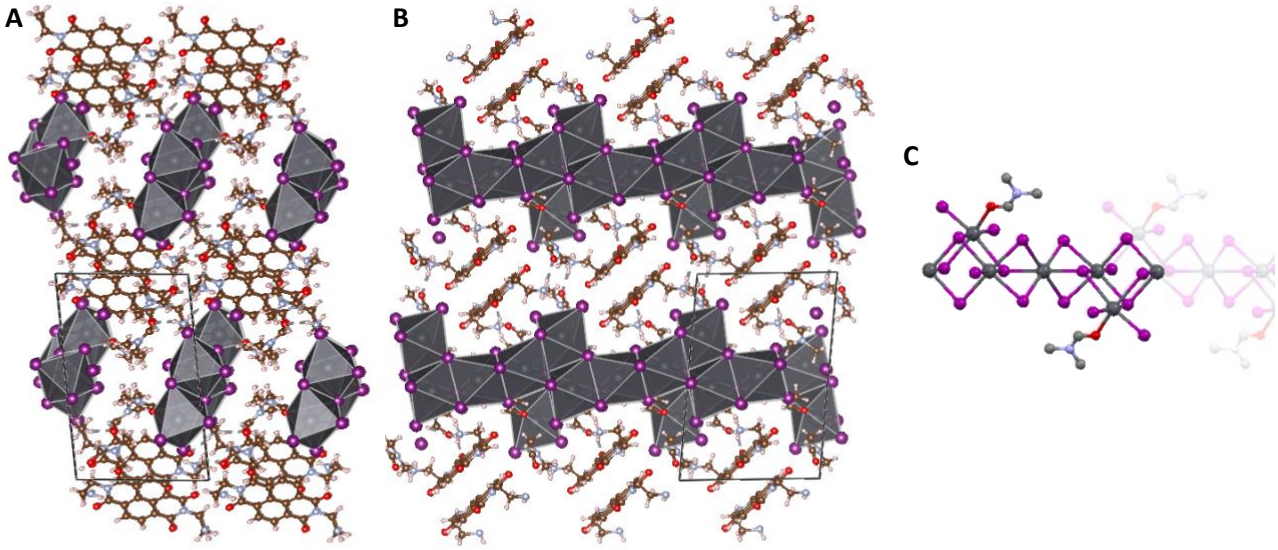


**Fig. 55.** (A, B) Two views of the crystal structure of **1**, $[(NDIC2)_2Pb_5I_{14}(DMF)_2]\cdot 4DMF$. (C) Detail showing a $[Pb_5I_{14}(DMF)_2]^{4-}$ chain (NDIC2 and non-coordinated DMF not shown).

The ammonium moieties of the NDIC2 dication each form hydrogen bonds to iodide ions in the wires. The N···I distances (3.65-3.83 ± 0.1 Å) are similar to those in 2D HOIPs (e.g. 3.63 Å for $(PEA)_2PbI_4$ (PEA = 2-phenylethylammonium)). In addition, there are a variety of close NDIC2···NDIC2 and NDIC2···DMF interactions. The NDIC2 dications also form π-stacked dimers with an interplanar distance of 3.35(0) Å and on offset between the two molecules of around half a benzene ring,[156] the π-stacking involving a different neighbor to that with which there is a DMF bridge.

Red plate-like crystals of **2** were obtained following slow vapor diffusion of dichloromethane into an NMP solution of $(NDIC2)I_2$ and $PbI_2$ over 3 days. SCXRD (Fig. 56) revealed that this material contains iodoplumbate clusters, isolated from each other by NDIC2 dications and NMP solvent molecules. Compounds, such as this, in which there is finite metal-halide catenation, rather than formation of infinite 1D chains, 2D sheets, or 3D frameworks are often described as 0D perovskite-like materials;[157, 158] however, only a few such 0D iodoplumbates have been reported.[159-166] The present structure is particularly unusual, however, in that the clusters are linked to one another by NDIC2 dications acting as bridging ligands in the coordination sphere of Pb, rather than by purely hydrogen-bonding or Van der Waals interactions, and so could also arguably be described as a 1D structure.

The core of each cluster in **2** consists of a linear $Pb_3I_{12}$ moiety formed by face-sharing between three octahedra (Fig. 56B), similar to that seen in the structure of $[(H_3N(CH_2)_7NH_3)_4Pb_3I_{12}(I)_2]$.[167] To each end of this core is attached a highly distorted Pb coordination polyhedron in which there are three short Pb—I bonds, two long Pb···I interactions, and a NDIC2···Pb interaction (see below). The three short bonds coordinate the lead in a trigonal prismatic fashion, but together with the three longer range interactions, form a highly distorted octahedron.

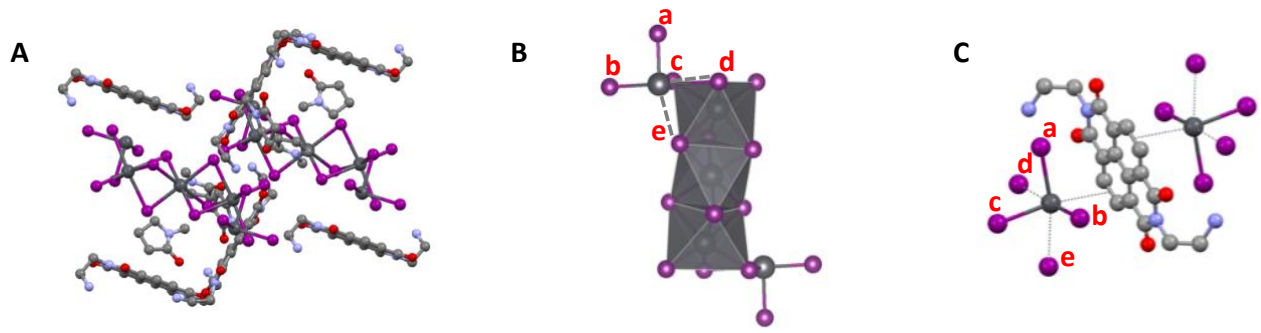


**Fig. 56.** (A) Crystal structure of **2**, $[(NDIC_2)_3Pb_5I_{16}]\cdot 6NMP$. (B) Detail showing the structure of the inorganic $Pb_5I_{16}^{6-}$ "0D" clusters consisting of a linear chain of three face-sharing $PbI_6$ octahedra and two terminal distorted Pb environments characterized by 3 short Pb—I bonds (to iodides a-c) and two very long bonds (to d and e). (C) Detail showing how NDIC2 molecules in the structure serve as $\eta^2$:$\eta^2$ ligands bridging the inorganic clusters and complete the octahedral coordination of the terminal Pb centers of the clusters.

There are two independent types of NDIC2 dication present in a 1:2 ratio in the structure of **2**. The first of these is coordinated to two Pb centers in separate clusters. Each interaction can be regarded as $\eta^2$-coordination of one of the aromatic rings of the NDIC2 dication to a Pb center; C—Pb distances are 3.61(4)-3.71(2) Å, with a distance of 3.59(2) Å between the centroids of the C—C bonds and the metal centers (Fig. 56). Thus the dication acts as an $\eta^2$:$\eta^2$ bridging ligand that stitches the iodoplumbate clusters into chains. Although a number of $Pb^{II}$-arene π-interactions have previously been reported,[168] the arene is usually coordinated in an axial ($\eta^6$) fashion, and examples with $\eta^2$-arenes are rare.[169, 170]

As in the structure of **1**, the structure also exhibits NDIC2···(solvent) hydrogen bonding and NDIC2···NDIC2 π-stacking. Each ammonium group on the Pb-coordinated NDIC2 dications is bridged to corresponding groups in neighboring cations through a hydrogen-bonding interaction with two NMP molecules; the oxygen atom of each NMP molecule being hydrogen-bonded to both $NH_3$ groups. Thus, these molecules form hydrogen-bonded chains. The NDIC2 molecules that are not coordinated to Pb exhibit a similar hydrogen-bonding pattern to the NDIC2 groups of **1**: one $NH_3$ group is bridged by two NMP groups to another dication, while the other $NH_3$ is hydrogen-bound to one terminal NMP molecule. Each uncoordinated NDIC2 molecule also forms a π-dimer with a neighboring molecule (not that to which it is connected via hydrogen-bonding), while those coordinated to Pb are not engaged in π-stacking.

A third iodoplumbate compound, **3**, was obtained as yellow crystals by slow vapor diffusion of ethanol in a DMF solution containing $PbI_2$ and $(NDIC2)I_2$ (Fig. 57). **3** is unstable both in solvents and in ambient conditions and is readily converted to **1**. It structure consists of highly distorted octahedra assembled, through multiple edge-sharing interactions, into 1D ribbons that are four octahedra wide. These ribbons are surrounded by DMF molecules and NDIC2 dications.

In contrast to what is seen in the structure of **1** and **2**, the NDIC2 dications in **3** π-π stack in a polymeric, rather than dimeric, fashion. The ammonium groups of the NDIC2 cations each hydrogen bond to an iodide, so that the π-stacked NDIC2 dications bridge adjacent ribbons, and to the oxygen atoms of two DMF molecules. Compared to what is seen in the structures of **1** and **2**, however, the π-conjugated cores of the NDIC2 dications are located further from the inorganic portions of the structure, which is consistent with the yellow, rather than red, coloration (see discussion of optical properties below).

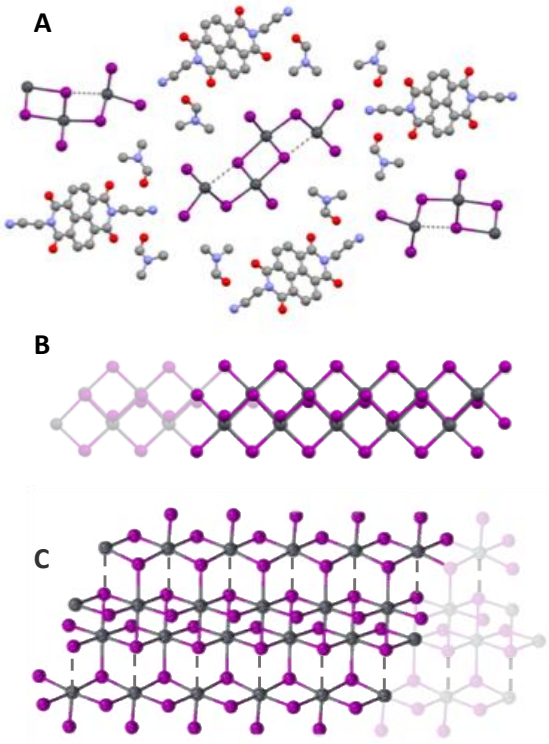


**Fig. 57.** (A) Crystal structure of **3**, $[(NDIC_2)Pb_4I_{10}]\cdot 4DMF$, viewed along the direction of the inorganic ribbons. (B, C) "Side" and "top" views of the inorganic ribbons.

Another compound, **4**, was synthesized by slow diffusion of ethanol in a solution of NMP containing (NDIC2)$I_2$ and $PbI_2$. The inorganic portion of the structure is simple relative to that of **1-3**, consisting of linear 1D wires of *trans*-face-sharing octahedral, i.e., it is an example of FSIP, as defined in the preceding sub-section.[150, 166, 171-174]

Upon immersion in water, most hybrid organic inorganic lead iodide compounds are known to decompose to $PbI_2$ or Pb(OH)H.[175] For example, crystals of the 2D HOIP $(PEA)_2PbI_4$ decompose to $PbI_2$ immediately upon addition of water. However, in the case of **1**, immersion in water for 24 h resulted in formation of a brown powder. EA and PXRD confirmed that we have two components present. Single-crystal X-ray diffraction (see below) indicates one component, namely **5**, of this product to have the composition $(NDIC_2)Pb_2I_6\bullet 2H_2O$ and to consist of 1D wires of *trans*-face-sharing octahedral, i.e. another FSIP, whereas the structure of the other component, **6**, is unknown, although it has an apparent empirical formula of $(NDIC_2)Pb_5I_{12}$. The **5**/**6** mixture is reasonable stable under ambient conditions, but is found to be transformed to PXRD-pure **6** on further exposure to water.

Acetonitrile or tetrahydrofuran, however, lead to the transformation of **1** to **7**, with the change being more rapid in the former solvent. These two solvents have been incorporated into several other haloplumbate structure;[149, 176, 177] however, solution NMR spectroscopy following redissolution of **7** in $d_6$-DMSO indicates only trace amounts of solvent relative to $NDIC2^{2+}$. EA suggests a formula for **7** of $[(NDIC_2)Pb_2I_6]$. Compound **7** is further transformed to another

material, **8**, when left in acetonitrile for more than three weeks. Again, the crystal structure could not be obtained, but, EA suggests a formula of [(NDIC2)$Pb_3I_8$]•MeCN. Although the structure is unknown, it is worth noting that several previous structures incorporating inorganic anions of empirical formula $Pb_3I_8^{2-}$ have been reported; these contain ribbons of edge-sharing or edge- and face-sharing $PbI_6$ octahedra.[178-181] Finally, heating compound **1** to 130 °C also leads to formation of **7**, presumably through loss of DMF and accompanied by formation of (NDIC2)$I_2$.

Diffuse reflectance spectra of **1** and **4-8** are shown in Fig. 58. Spectra were not obtained for **2** and **3** due to the small quantities obtained, but **2** has a similar red color to **1**, **4**, and **5**, while **3** is yellow-orange. The red color and long-wavelength absorption onsets for **1**, **2**, and **4-8** suggests a mixed organic-inorganic origin, since isolated NDI *N,N′*-dialkyl NDIs absorb at ca. 380 nm,[182] while [(piperidinium)$PbI_3$] (which contains similar chains to **4** and **5**) exhibits an absorption maximum of ca. 400 nm.[183] Accordingly, we attribute the long-wavelength absorption of the red materials to charge transfer (CT) from the inorganic portion – the highest-lying states from which are presumably predominantly iodide based – to the NDI. CT of this type has previously been suggested to account for the similar spectrum of another NDI/Pb/I material,[152] while inorganic-to-cation CT has been invoked in other Pb/I materials in which the cations have comparable cathodic reduction potentials to NDIs, for example, in the cases of methylviologen and tropylium materials.[174, 183] Indeed, visible-region CT bands between "free" iodide ions and NDIs are also seen in solution (see ref. [184]).

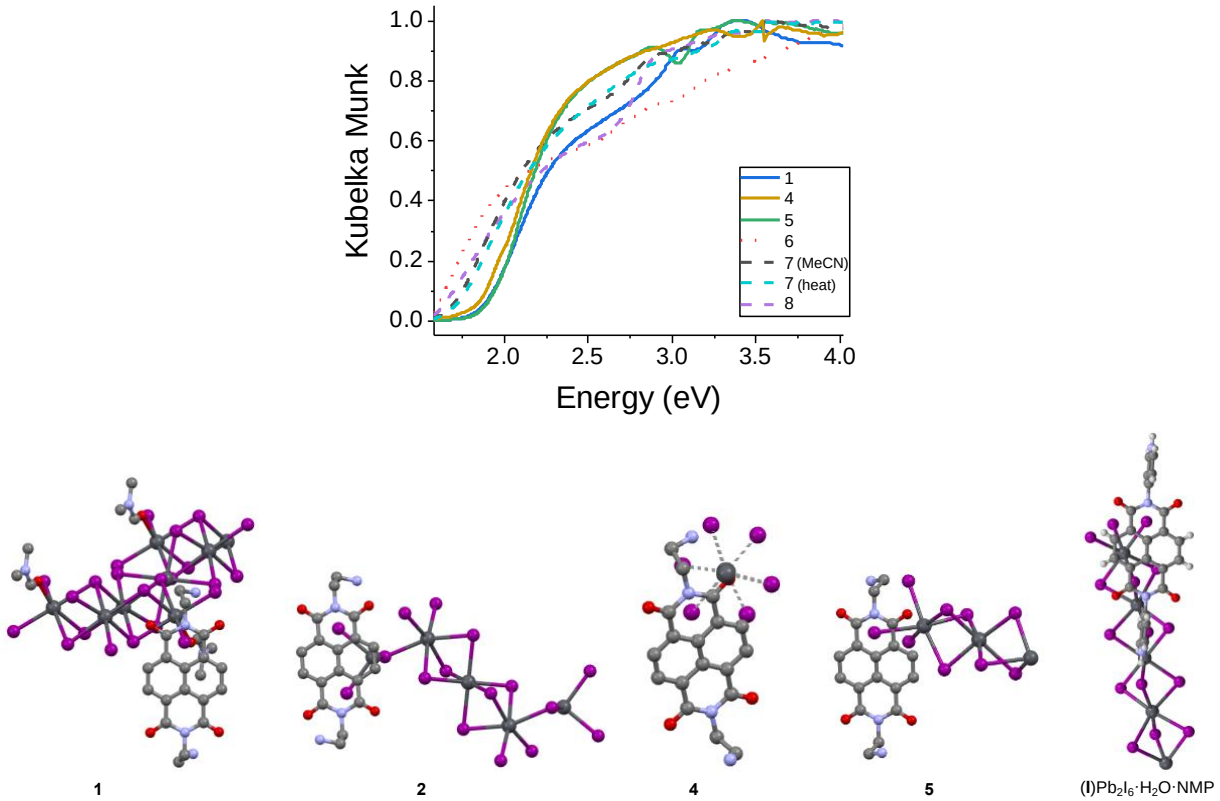


**Fig. 58.** Top: Diffuse reflectance spectra of HIPCs **1** and **4-8** (with data for **7** from two different methods of synthesis). Bottom: Close contacts between iodides and naphthalene diimide cores in the crystal structures of **1** (iodide—ring

centroid distance = 3.534 Å), **2** (3.666 Å), **4** (3.519 Å), and **5** (3.580 Å), and in the previously reported structure of (**I**)$Pb_2I_6$•$H_2O$•NMP (3.485 Å). The distances are calculated from the crystal structure (I to centroid of the ring).

Consistent with an iodide-to-NDI CT origin for their low-energy absorption onsets, all the red crystals, exhibit close contacts between an iodide and an imide ring (Fig. 58), where there are known to be large LUMO coefficients located between the quaternary and CO carbon atoms.[185] Crystals of **3** do not exhibit such close interactions between iodides and the NDI cores, consistent with the orange-yellow, rather than red, color of this material. The somewhat lower-energy absorption onsets of **6-9** (for which we do not have structural information) relative to those of **1**/**4**/**5** may reflect destabilization of the highest filled iodide-based orbitals through significantly different structures in the inorganic portion, or stabilization of the lowest-lying empty NDI-based orbitals through π-aggregation.

The conductivity of crystals of **1** was tested using two-point current-voltage (*I-V*) scans.[186] The linear behavior confirms that ohmic contacts have been established. There is also no hysteresis. The conductivity extracted from the *I-V* curves is $5.4 \times 10^{-5} \pm 1.1 \times 10^{-5}$ S $m^{-1}$. This is comparable to the value reported for (1-methylpiperidinium)$PbI_3$, which contains 1D chains of face-sharing octahedral similar to those in **4** and **5**,[187] but significantly higher than in layered perovskites of the type (β-Me-PEA)$_2MA_{n-1}Pb_nI_{3n+1}$ (β-Me-PEA = β-methylphenethylammonium = 2-phenylpropan-1-ammonium; MA = methylammonium; n = 1-3).[188] Similar conductivities, ranging from ca. $10^{-5}$ to $10^{-4}$ S $m^{-1}$, have been reported for single crystals of $MAPbI_3$.[189, 190]

The photoresponse of the crystals was evaluated by taking *I*−*V* scans under dark and illuminated conditions, using a white LED light source. A slight increase in current with increasing light intensity is consistent with photogeneration of charge carriers. The responsivity (*R*), detectivity (*D**), and on/off ratio at 5 V and a light intensity of 14.5 W $m^{-2}$ were estimated to be $2.2 \times 10^{-3} \pm 0.2 \times 10^{-3}$ A $W^{-1}$, $4.3 \times 10^7 \pm 1.4 \times 10^7$ Jones, and 3.9 ± 0.3, respectively. These properties are quite modest compared with those obtained in related materials, such as $MAPbI_3$ nanowires.[191, 192]

## IV.6. References


1. M. T. Klug, A. Osherov, A. A. Haghighirad, S. D. Stranks, P. R. Brown, S. Bai, J. T. W. Wang, X. Dang, V. Bulovic, H. J. Snaith and A. M. Belcher, *Energy Environ. Sci.*, 2017, **10**, 236-246.
2. J. T.-W. Wang, Z. Wang, S. Pathak, W. Zhang, D. W. deQuilettes, F. Wisnivesky-Rocca-Rivarola, J. Huang, P. K. Nayak, J. B. Patel, H. A. Mohd Yusof, Y. Vaynzof, R. Zhu, I. Ramirez, J. Zhang, C. Ducati, C. Grovenor, M. B. Johnston, D. S. Ginger, R. J. Nicholas and H. J. Snaith, *Energy Environ. Sci.*, 2016, **9**, 2892-2901.
3. P. K. Nayak, M. Sendner, B. Wenger, Z. Wang, K. Sharma, A. J. Ramadan, R. Lovrinčić, A. Pucci, P. K. Madhu and H. J. Snaith, *J. Am. Chem. Soc.*, 2018, **140**, 574–577.
4. D. Pérez-del-Rey, D. Forgács, E. M. Hutter, T. J. Savenije, D. Nordlund, P. Schulz, J. J. Berry, M. Sessolo and H. J. Bolink, *Adv. Mater.*, 2016, **28**, 9839–9845.
5. C. F. J. Lau, M. Zhang, X. Deng, J. Zheng, J. Bing, Q. Ma, J. Kim, L. Hu, M. A. Green, S. Huang and A. Ho-Baillie, *ACS Energy Lett.*, 2017, **2**, 2319–2325.
6. S. Olthof and K. Meerholz, *Sci. Rep.*, 2017, **7**, 40267.
7. J. Emara, T. Schnier, N. Pourdavoud, T. Riedl, K. Meerholz and S. Olthof, *Adv. Mater.*, 2016, **28**, 553–559.
8. P. Cui, D. Wei, J. Ji, H. Huang, E. Jia, S. Dou, T. Wang, W. Wang and M. Li, *Nat. Energy*, 2019, **4**, 150-159.
9. S. N. Habisreutinger, N. K. Noel, H. J. Snaith and R. J. Nicholas, *Adv. Energy Mater.*, 2016, **7**, 1601079.
10. A. Magomedov, E. Kasparavičius, K. Rakstys, S. Paek, N. Gasilova, K. Genevičius, G. Juška, T. Malinauskas, M. K. Nazeeruddin and V. Getautis, *J. Mater. Chem. C*, 2018, **6**, 8874–8878.

11. J. Zhang, T. Zhang, L. Jiang, U. Bach and Y.-B. Cheng, *ACS Energy Lett.*, 2018, **3**, 1677–1682.
12. J. P. Bastos, U. W. Paetzold, R. Gehlhaar, W. Qiu, D. Cheyns, S. Surana, V. Spampinato, T. Aernouts and J. Poortmans, *Adv. Energy Mater.*, 2018, **8**, 1800554.
13. A. Pellaroque, N. K. Noel, S. N. Habisreutinger, Y. Zhang, S. Barlow, S. Marder and H. J. Snaith, *ACS Energy Lett.*, 2017, **2**, 2044-2050.
14. D. Ramirez, K. Schutt, J. F. Montoya, S. Mesa, J. Lim, H. J. Snaith and F. Jaramillo, *J. Phys. Chem. C*, 2018, **122**, 21239–21247.
15. M. I. Saidaminov, A. L. Abdelhady, B. Murali, E. Alarousu, V. M. Burlakov, W. Peng, I. Dursun, L. Wang, Y. He, G. Maculan, A. Goriely, T. Wu, O. F. Mohammed and O. M. Bakr, *Nat. Commun.*, 2015, **6**, 7586.
16. Y. Liu, Z. Yang, D. Cui, X. Ren, J. Sun, X. Liu, J. Zhang, Q. Wei, H. Fan, F. Yu, X. Zhang, C. Zhao and S. Liu, *Adv. Mater.*, 2015, **27**, 5176–5183.
17. P. K. Nayak, D. T. Moore, B. Wenger, S. Nayak, A. A. Haghighirad, A. Fineberg, N. K. Noel, O. G. Reid, G. Rumbles, P. Kukura, K. A. Vincent and H. J. Snaith, *Nat. Commun.*, 2016, **7**, 13303.
18. A. Dai, Y. Zhou, A. L. Shu, S. K. Mohapatra, H. Wang, C. Fuentes-Hernandez, Y. Zhang, S. Barlow, Y.-L. Loo, S. R. Marder, B. Kippelen and A. Kahn, *Adv. Funct. Mater.*, 2014, **24**, 2197–2204.
19. S. D. Stranks, V. M. Burlakov, T. Leijtens, J. M. Ball, A. Goriely and H. J. Snaith, *Phys. Rev. Appl.*, 2014, **2**, 34007.
20. D. W. deQuilettes, S. Jariwala, S. Burke, M. E. Ziffer, J. T.-W. Wang, H. J. Snaith and D. S. Ginger, *ACS Nano*, 2017, **11**, 11488-11496.
21. S. N. Habisreutinger, B. Wenger, H. J. Snaith and R. J. Nicholas, *ACS Energy Lett.*, 2017, **2**, 622-628.
22. S. N. Habisreutinger, N. K. Noel and H. J. Snaith, *ACS Energy Lett.*, 2018, **3**, 2472–2476.
23. N. K. Noel, A. Abate, S. D. Stranks, E. S. Parrott, V. M. Burlakov, A. Goriely and H. J. Snaith, *ACS Nano*, 2014, **8**, 9815-9821.
24. K. Wojciechowski, T. Leijtens, S. Siprova, C. Schlueter, M. T. Hörantner, J. T.-W. Wang, C.-Z. Li, A. K. Y. Jen, T.-L. Lee and H. J. Snaith, *J. Phys. Chem. Lett.*, 2015, **6**, 2399–2405.
25. H. J. Snaith, A. Abate, J. M. Ball, G. E. Eperon, T. Leijtens, N. K. Noel, S. D. Stranks, J. T.-W. Wang, K. Wojciechowski and W. Zhang, *J. Phys. Chem. Lett.*, 2014, **5**, 1511–1515.
26. N. K. Noel, S. N. Habisreutinger, Alba Pellaroque, F. Pulvirenti, B. Wenger, F. Zhang, Y.-H. Lin, O. G. Reid, J. Leisen, Y. Zhang, S. Barlow, Seth R. Marder, A. Kahn, H. J. Snaith, C. B. Arnold and B. P. Rand, *Energy Environ. Sci.*, 2019, **12**, 3063-3073.
27 D. A. Valverde-Chávez, E. Rojas-Gatjens, J. Williamson, S. Jariwala, Y. Shi, D. P. McCarthy, S. Barlow, S. R. Marder, D. S. Ginger and C. Silva-Acuña, *J. Mater. Chem. C*, 2021, **9**, 8204-8212.
28. M. Saliba, S. Orlandi, T. Matsui, S. Aghazada, M. Cavazzini, J.-P. Correa-Baena, P. Gao, R. Scopelliti, E. Mosconi, K.-H. Dahmen, F. De Angelis, A. Abate, A. Hagfeldt, G. Pozzi, M. Graetzel and M. K. Nazeeruddin, *Nat. Energy*, 2016, **1**, 15017.
29. H. Zhang, L. Xue, J. Han, Y. Q. Fu, Y. Shen, Z. Zhang, Y. Li and M. Wang, *J. Mater. Chem. A*, 2016, **4**, 8724-8733.
30. B. Chaudhary, A. Kulkarni, A. K. Jena, M. Ikegami, Y. Udagawa, H. Kunugita, K. Ema and T. Miyasaka, *ChemSusChem*, 2017, **10**, 2473-2479.
31. M. L. Petrus, K. Schutt, M. T. Sirtl, E. M. Hutter, A. C. Closs, J. M. Ball, J. C. Bijleveld, A. Petrozza, T. Bein, T. J. Dingemans, T. J. Savenije, H. Snaith and P. Docampo, *Adv. Energy Mater.*, 2018, **8**, 1801605.
32. S. K. Mohapatra, Y. Zhang, B. Sandhu, M. S. Fonari, T. V. Timofeeva, S. R. Marder and S. Barlow, *Polyhedron*, 2016, **116**, 88-95.
33. P. Zhao, B. J. Kim and H. S. Jung, *Mater. Today Energy*, 2018, **7**, 267-286.
34. A. Rajagopal, K. Yao and A. K. Y. Jen, *Adv. Mater.*, 2018, **30**, 1800455.
35. D. S. Lee, J. S. Yun, J. Kim, A. M. Soufiani, S. Chen, Y. Cho, X. Deng, J. Seidel, S. Lim, S. Huang and A. W. Y. Ho-Baillie, *ACS Energy Lett.*, 2018, **3**, 647-654.
36. M.-H. Tremblay, K. Schutt, Y. Zhang, S. Barlow, H. J. Snaith and S. R. Marder, *New J. Chem.*, 2021, **45**, 15017-15021.
37. M.-H. Tremblay, K. Schutt, Y. Zhang, J. Lim, Y.-H. Lin, J. H. Warby, S. Barlow, H. J. Snaith and S. R. Marder, *Sustain. Energy Fuels*, 2020, **4**, 190-198.
38. R. K. Hallani, M. Moser, H. Bristow, M. V. C. Jenart, H. Faber, M. Neophytou, E. Yarali, A. F. Paterson, T. D. Anthopoulos and I. McCulloch, *J. Org. Chem.*, 2020, **85**, 277-283.
39. L. Derue, O. Dautel, A. Tournebize, M. Drees, H. Pan, S. Berthumeyrie, B. Pavageau, E. Cloutet, S. Chambon, L. Hirsch, A. Rivaton, P. Hudhomme, A. Facchetti and G. Wantz, *Adv. Mater.*, 2014, **26**, 5831-5838.

40. N. Deb, R. R. Dasari, K. Moudgil, J. L. Hernandez, S. R. Marder, Y. Sun, A. Karim and D. G. Bucknall, *J. Mater. Chem. A*, 2015, **3**, 21856-21863.
41. K. Wojciechowski, I. Ramirez, T. Gorisse, O. Dautel, R. Dasari, N. Sakai, J. M. Hardigree, S. Song, S. Marder, M. Riede, G. Wantz and H. J. Snaith, *ACS Energy Lett.*, 2016, **1**, 648-653.
42. A. Gügel, P. Belik, M. Walter, A. Kraus, E. Harth, M. Wagner, J. Spickermann and K. Müllen, *Tetrahedron*, 1996, **52**, 5007-5014.
43. D. P. McMeekin, Z. Wang, W. Rehman, F. Pulvirenti, J. B. Patel, N. K. Noel, M. B. Johnston, S. R. Marder, L. M. Herz and H. J. Snaith, *Adv. Mater.*, 2017, **29**, 1607039.
44. O. V. Gusev, L. I. Denisovich, M. G. Peterleitner, A. Z. Rubezhov, N. A. Ustynyuk and P. M. Maitlis, *J. Organomet. Chem.*, 1993, **452**, 219-222.
45. O. V. Gusev, M. G. Peterleitner, M. A. Ievlev, A. M. Kal'sin, P. V. Petrovskii, L. I. Denisovich and N. A. Ustynyuk, *J. Organomet. Chem.*, 1997, **531**, 95-100.
46. O. V. Gusev, M. A. Ievlev, M. G. Peterleitner, S. M. Peregudova, L. I. Denisovich, P. V. Petrovskii and N. A. Ustynyuk, *J. Organomet. Chem.y*, 1997, **534**, 57-66.
47. S. K. Mohapatra, A. Fonari, C. Risko, K. Yesudas, K. Moudgil, J. H. Delcamp, T. V. Timofeeva, J.-L. Brédas, S. R. Marder and S. Barlow, *Chem. Eur. J.*, 2014, **20**, 15385-15394.
48. S. Olthof, S. Mehraeen, S. K. Mohapatra, S. Barlow, V. Coropceanu, J.-L. Brédas, S. R. Marder and A. Kahn, *Phys. Rev. Lett.*, 2012, **109**, 176601.
49. F. Pulvirenti, B. Wegner, N. K. Noel, G. Mazzotta, R. Hill, J. B. Patel, L. M. Herz, M. B. Johnston, M. K. Riede, H. J. Snaith, N. Koch, S. Barlow and S. R. Marder, *Mol. Syst. Des. Eng.*, 2018, **3**, 741-747.
50. J. Avila, M.-G. La-Placa, E. Longhi, M. Sessolo, S. Barlow, S. R. Marder and H. J. Bolink, *J. Mater. Chem. A*, 2019, **7**, 25796-25801.
51. S. Guo, S. B. Kim, S. K. Mohapatra, Y. Qi, T. Sajoto, A. Kahn, S. R. Marder and S. Barlow, *Adv. Mater.* 2012, **24**, 699-703.
52. D. V. Konarev, N. V. Drichko and A. Graja, *J. Chim. Phys.*, 1998, **95**, 2143-2156.
53. B. D. Naab, S. Guo, S. Olthof, E. G. B. Evans, P. Wei, G. L. Millhauser, A. Kahn, S. Barlow, S. R. Marder and Z. Bao, *J. Am. Chem. Soc.*, 2013, **135**, 15018-15025.
54. G. Lu, H. Tang, Y. Qu, L. Li and X. Yang, *Macromolecules*, 2007, **40**, 6579-6584.
55. F. S. Kim and S. A. Jenekhe, *Macromolecules*, 2012, **45**, 7514-7519.
56. J. Sun, B. J. Jung, T. Lee, L. Berger, J. Huang, Y. Liu, D. H. Reich and H. E. Katz, *ACS Appl. Mater. & Interfaces*, 2009, **1**, 412-419.
57. Y. Kubota and Y. Tominaga, *Mater. Today Commun.* 2015, **4**, 124-129.
58. G. Lu, L. Bu, S. Li and X. Yang, *Adv. Mater.* 2014, **26**, 2359-2364.
59. L. Qiu, W. H. Lee, X. Wang, J. S. Kim, J. A. Lim, D. Kwak, S. Lee and K. Cho, *Adv. Mater.*, 2009, **21**, 1349-1353.
60. Z. Bin, J. Li, L. Wang and L. Duan, *Energy Environ. Sci.*, 2016, **9**, 3424-3428.
61. S. S. Kim, S. Bae and W. H. Jo, *Chem. Commun.*, 2015, **51**, 17413-17416.
62. G. Kakavelakis, T. Maksudov, D. Konios, I. Paradisanos, G. Kioseoglou, E. Stratakis and E. Kymakis, *Adv. Energy Mater.*, 2017, **7**, 1602120.
63. C. Kuang, G. Tang, T. Jiu, H. Yang, H. Liu, B. Li, W. Luo, X. Li, W. Zhang, F. Lu, J. Fang and Y. Li, *Nano Lett.*, 2015, **15**, 2756-2762.
64. Z. Yang, J. Xie, V. Arivazhagan, K. Xiao, Y. Qiang, K. Huang, M. Hu, C. Cui, X. Yu and D. Yang, *Nano Energy*, 2017, **40**, 345-351.
65. F. Pulvirenti, Doctoral dissertation, Georgia Institute of Technology, 2019.
66. A. Pellaroque, N. K. Noel, S. N. Habisreutinger, Y. Zhang, S. Barlow, S. R. Marder and H. J. Snaith, *ACS Energy Lett.* 2017, **2**, 2044-2050.
67. M.-H. Tremblay, K. Schutt, Y. Zhang, J. Lim, Y.-H. Lin, J. H. Warby, S. Barlow, H. J. Snaith and S. R. Marder, *Sustain. Energy Fuels*, 2020, **4**, 190-198.
68. M.-H. Tremblay, K. Schutt, F. Pulvirenti, T. Schultz, B. Wegner, X. Jia, Y. Zhang, E. Longi, R. R. Dasari, C. Fuentes Hernandez, B. Kippelen, N. Koch, H. J. Snaith, S. Barlow and S. R. Marder, *J. Mater. Chem. A*, 2021, **9**, 9347-9353.
69. N. Deb, R. R. Dasari, K. Moudgil, J. L. Hernandez, S. R. Marder, Y. Sun, A. Karimd and D. G. Bucknall, *J. Mater. Chem. A*, 2015, **3**, 21856.
70. J. Avila, M.-G. La-Placa, E. Longhi, M. Sessolo, S. Barlow, S. R. Marder and H. J. Bolink, *J. Mater. Chem. A*, 2019, **7**, 25796-25801.

71. R. B. M. Hill, S.-H. Turren-Cruz, F. Pulvirenti, W. R. Tress, S. Wieghold, S. Sun, L. Nienhaus, M. Bawendi, T. Buonassisi, S. Barlow, A. Hagfeldt, S. R. Marder and J.-P. Correa-Baena, *ACS Appl. Energy Mater.*, 2019, **24**, 2402-2408.
72. I. C. Smith, E. T. Hoke, D. Solis-Ibarra, M. D. McGehee and H. I. Karunadasa, *Angew. Chem.*, 2014, **53**, 11232-11235.
73. J. Yan, W. Qiu, G. Wu, P. Heremans and H. Chen, *J. Mater. Chem. A*, 2018, **6**, 11063-11077.
74. Y. Chen, Y. Sun, J. Peng, W. Zhang, X. Su, K. Zheng, T. Pullerits and Z. Liang, *Adv. Energy Mater.*, 2017, **7**, 1700162.
75. D. H. Cao, C. C. Stoumpos, O. K. Farha, J. T. Hupp and M. G. Kanatzidis, *J. Am. Chem. Soc.*, 2015, **137**, 7843-7850.
76. C. Ma, D. Shen, T.-W. Ng, M.-F. Lo and C.-S. Lee, *Adv. Mater.* 2018, **30**, 1800710.
77. H. Lai, B. Kan, T. Liu, N. Zheng, Z. Xie, T. Zhou, X. Wan, X. Zhang, Y. Liu and Y. Chen, *J. Am. Chem. Soc.*, 2018, **140**, 11639-11646.
78. H. Tsai, W. Nie, J.-C. Blancon, C. C. Stoumpos, R. Asadpour, B. Harutyunyan, A. J. Neukirch, R. Verduzco, J. J. Crochet, S. Tretiak, L. Pedesseau, J. Even, M. A. Alam, G. Gupta, J. Lou, P. M. Ajayan, M. J. Bedzyk, M. G. Kanatzidis and A. D. Mohite, *Nature*, 2016, **536**, 312.
79. L. Mao, W. Ke, L. Pedesseau, Y. Wu, C. Katan, J. Even, M. R. Wasielewski, C. C. Stoumpos and M. G. Kanatzidis, *J. Am. Chem. Soc.*, 2018, **140**, 3775-3783.
80. C. C. Stoumpos, D. H. Cao, D. J. Clark, J. Young, J. M. Rondinelli, J. I. Jang, J. T. Hupp and M. G. Kanatzidis, *Chem. Mater.*, 2016, **28**, 2852-2867.
81. S. Ahmad, P. Fu, S. Yu, Q. Yang, X. Liu, X. Wang, X. Wang, X. Guo and C. Li, *Joule*, 2019, **3**, 794-806.
82. M. Yuan, L. N. Quan, R. Comin, G. Walters, R. Sabatini, O. Voznyy, S. Hoogland, Y. Zhao, E. M. Beauregard, P. Kanjanaboos, Z. Lu, D. H. Kim and E. H. Sargent, *Nat. Nanotech.*, 2016, **11**, 872.
83. H. Tsai, W. Nie, J.-C. Blancon, C. C. Stoumpos, C. M. M. Soe, J. Yoo, J. Crochet, S. Tretiak, J. Even, A. Sadhanala, G. Azzellino, R. Brenes, P. M. Ajayan, V. Bulović, S. D. Stranks, R. H. Friend, M. G. Kanatzidis and A. D. Mohite, *Adv. Mater.*, 2018, **30**, 1704217.
84. A. E. Maughan, J. A. Kurzman and J. R. Neilson, *Inorg. Chem.*, 2015, **54**, 370-378.
85. H. Zhang, S.-S. Yu and H.-B. Duan, *Inorg. Chem. Commun.* 2018, **93**, 1-5.
86. K. Matsuishi, Y. Kubo, T. Ichikawa and S. Onari, *AIP Conf. Proc.* 2005, **772**, 1075-1076.
87. I. B. Koutselas, D. B. Mitzi, G. C. Papavassiliou, G. J. Papaioannou and H. Krautscheid, *Synth. Met.*, 1997, **86**, 2171-2172.
88. H.-B. Duan, H.-R. Zhao, X.-M. Ren, H. Zhou, Z.-F. Tian and W.-Q. Jin, *Dalton Trans.*, 2011, **40**, 1672-1683.
89. B.-G. Chen, *Inorg. Nano-Met. Chem.*, 2017, **47**, 1220-1225.
90. M.-J. Wang, X.-R. Chen, Y.-B. Tong, G.-J. Yuan, X.-M. Ren and J.-L. Liu, *Inorg. Chem.*, 2017, **56**, 9525-9534.
91. C.-H. Wang, H.-J. Du, Y. Li, Y.-Y. Niu and H.-W. Hou, *New J. Chem.*, 2015, **39**, 7372-7378.
92. A. Zeb, Z. Sun, T. Khan, M. A. Asghar, Z. Wu, L. Li, C. Ji and J. Luo, *Inorg. Chem. Front.* 2017, **4**, 1485-1492.
93. A. Zeb, Z. Sun, A. Khan, S. Zhang, T. Khan, M. A. Asghar and J. Luo, *Inorg. Chem. Front.*, 2018, **5**, 897-902.
94. G. Liu, J. Liu, Z. Sun, Z. Zhang, L. Chang, J. Wang, X. Tao and Q. Zhang, *Inorg. Chem.*, 2016, **55**, 8025-8030.
95. C. Ji, Z. Sun, A. Zeb, S. Liu, J. Zhang, M. Hong and J. Luo, *J. Phys. Chem. Lett.*, 2017, **8**, 2012-2018.
96. X.-N. Hua, W.-Q. Liao, Y.-Y. Tang, P.-F. Li, P.-P. Shi, D. Zhao and R.-G. Xiong, *J. Am. Chem.Soc.*, 2018, **140**, 12296-12302.
97. H.-R. Zhao, D.-P. Li, X.-M. Ren, Y. Song and W.-Q. Jin, *J. Am. Chem. Soc.*, 2010, **132**, 18-19.
98. S. Mishra, E. Jeanneau, O. Iasco, G. Ledoux, D. Luneau and S. Daniele, *Eur. J. Inorg. Chem.*, 2012, **2012**, 2749-2758.
99. H.-H. Li, Z.-R. Chen, L.-C. Cheng, Y.-J. Wang, M. Feng and M. Wang, *Dalton Trans.*, 2010, **39**, 11000-11007.
100. C. Seth and D. Khushalani, *ChemNanoMat*, 2019, **5**, 85-91.
101. I. Chung, J.-H. Song, J. Im, J. Androulakis, C. D. Malliakas, H. Li, A. J. Freeman, J. T. Kenney and M. G. Kanatzidis, *J. Am. Chem. Soc.* 2012, **134**, 8579-8587.
102. G.-N. Liu, J.-R. Shi, X.-J. Han, X. Zhang, K. Li, J. Li, T. Zhang, Q.-S. Liu, Z.-W. Zhang and C. Li, *Dalton Trans.* 2015, **44**, 12561-12575.

103. L. Gao, I. Spanopoulos, W. Ke, S. Huang, I. Hadar, L. Chen, X. Li, G. Yang and M. G. Kanatzidis, *ACS Energy Lett.*, 2019, **4**, 1763-1769.
104. M.-H. Tremblay, F. Thouin, J. Leisen, J. Bacsa, A. R. Srimath Kandada, J. M. Hoffman, M. G. Kanatzidis, A. D. Mohite, C. Silva, S. Barlow and S. R. Marder, *J. Am. Chem. Soc.*, 2019, **141**, 4521-4525.
105. M.-H. Tremblay, J. Bacsa, B. Zhao, F. Pulvirenti, S. Barlow and S. Marder, *Chem. Mater.*, 2019, **31**, 6145-6153.
106. M.-H. Tremblay, J. Bacsa, S. Barlow and S. R. Marder, *Mater. Chem. Front.*, 2020, **4**, 2023-2028.
107. K.-z. Du, Q. Tu, X. Zhang, Q. Han, J. Liu, S. Zauscher and D. B. Mitzi, *Inorg. Chem.*, 2017, **56**, 9291-9302.
108. L. Mao, C. C. Stoumpos and M. G. Kanatzidis, *J. Am. Chem. Soc.*, 2019, **141**, 1171-1190.
109. C. C. Stoumpos and M. G. Kanatzidis, *Acc. Chem. Res.*, 2015, **48**, 2791-2802.
110. C. Katan, N. Mercier and J. Even, *Chem. Rev.*, 2019, **119**, 3140-3192.
111. L. Pedesseau, D. Sapori, B. Traore, R. Robles, H.-H. Fang, M. A. Loi, H. Tsai, W. Nie, J.-C. Blancon, A. Neukirch, S. Tretiak, A. D. Mohite, C. Katan, J. Even and M. Kepenekian, *ACS Nano*, 2016, **10**, 9776-9786.
112. J. L. Knutson, J. D. Martin and D. B. Mitzi, *Inorg. Chem.* 2005, **44**, 4699-4705.
113. T. Umebayashi, K. Asai, T. Kondo and A. Nakao, *Phys. Rev. B*, 2003, **67**, 155405.
114. M.-H. Tremblay, J. Bacsa, B. Zhao, F. Pulvirenti, S. Barlow and S. R. Marder, *Chem. Mater.*, 2019, **31**, 6145-6153.
115. L. Mao, Y. Wu, C. C. Stoumpos, M. R. Wasielewski and M. G. Kanatzidis, *J. Am. Chem. Soc.* 2017, **139**, 5210-5215.
116. L. Mao, P. Guo, M. Kepenekian, I. Spanopoulos, Y. He, C. Katan, J. Even, R. D. Schaller, R. Seshadri, C. C. Stoumpos and M. G. Kanatzidis, *J. Am. Chem. Soc.*, 2020, 18, 8342-8351.
117. X. Li, W. Ke, B. Traoré, P. Guo, I. Hadar, M. Kepenekian, J. Even, C. Katan, C. C. Stoumpos, R. D. Schaller and M. G. Kanatzidis, *J. Am. Chem. Soc.*, 2019, **141**, 12880-12890.
118. D. B. Straus, N. Iotov, M. R. Gau, Q. Zhao, P. J. Carroll and C. R. Kagan, *J. Phys. Chem. Lett.* 2019, **10**, 1198-1205.
119. N. R. Venkatesan, A. Mahdi, B. Barraza, G. Wu, M. L. Chabinyc and R. Seshadri, *Dalton Trans.*, 2019, **48**, 14019-14026.
120. C.-K. Yang, W.-N. Chen, Y.-T. Ding, J. Wang, Y. Rao, W.-Q. Liao, Y.-Y. Tang, P.-F. Li, Z.-X. Wang and R.-G. Xiong, *Adv. Mater.* 2019, **31**, 1808088.
121. X.-H. Zhu, N. Mercier, A. Riou, P. Blanchard and P. Frère, *Chem. Commun.*, 2002, 2160-2161.
122. H. Dammak, S. Elleuch, H. Feki and Y. Abid, *Solid State Sci.* 2016, **61**, 1-8.
123. D. G. Billing and A. Lemmerer, *Acta Crystallogr. C*, 2006, **62**, m269-m271.
124. J. Hu, I. W. H. Oswald, S. J. Stuard, M. M. Nahid, N. Zhou, O. S. Williams, Z. Gui, L. Yan, H. Hu, Z. Chen, X. Xiao, Y. Lin, J. Huang, A. M. Moran, H. Ade, J. R. Neilson and W. You, *CSD Communication*, 2019, DOI: 10.5517/ccdc.csd.cc21k6wq.
125. J. Hu, I. W. H. Oswald, S. J. Stuard, M. M. Nahid, N. Zhou, O. F. Williams, Z. Guo, L. Yan, H. Hu, Z. Chen, X. Xiao, Y. Lin, J. Huang, A. M. Moran, H. Ade, J. R. Neilson and W. You, *CSD Communication*, DOI: 10.5517/CCDC.CSD.CC21K6XR.
126. M.-H. Tremblay, F. Thouin, J. Leisen, J. Bacsa, A. R. Srimath Kandada, J. M. Hoffman, M. G. Kanatzidis, A. D. Mohite, C. Silva, S. Barlow and S. R. Marder, *J. Am. Chem. Soc.* 2019, **141**, 4521-4525.
127. J. V. Passarelli, D. J. Fairfield, N. A. Sather, M. P. Hendricks, H. Sai, C. L. Stern and S. I. Stupp, *J. Am. Chem. Soc.*, 2018, **140**, 7313-7323.
128. V. Gómez, O. Fuhr and M. Ruben, *CrystEngComm*, 2016, **18**, 8207-8219.
129. M. Safdari, D. Phuyal, B. Philippe, P. H. Svensson, S. M. Butorin, K. O. Kvashnina, H. Rensmo, L. Kloo and J. M. Gardner, *Journal of Materials Chem. A*, 2017, **5**, 11730-11738.
130. P. Gao, A. R. Bin Mohd Yusoff and M. K. Nazeeruddin, *Nature Communications*, 2018, **9**, 5028.
131. T. Li, W. A. Dunlap-Shohl, Q. Han and D. B. Mitzi, *Chem. Mater.*, 2017, **29**, 6200-6204.
132. J. Hu, I. W. H. Oswald, S. J. Stuard, M. M. Nahid, N. Zhou, O. S. Williams, Z. Gui, L. Yan, H. Hu, Z. Chen, X. Xiao, Y. Lin, J. Huang, A. M. Moran, H. Ade, J. R. Neilson and W. You, *CSD Communication*, 2019.
133. M. E. Kamminga, H.-H. Fang, M. R. Filip, F. Giustino, J. Baas, G. R. Blake, M. A. Loi and T. T. M. Palstra, *Chem. Mater.*, 2016, **28**, 4554-4562.
134. A. J. Boyington, C. P. Seath, A. M. Zearfoss, Z. Xu and N. T. Jui, *J. Am. Chem. Soc.*, **141**, 4147-4153.
135. X. Li, J. Hoffman, W. Ke, M. Chen, H. Tsai, W. Nie, A. D. Mohite, M. Kepenekian, C. Katan, J. Even, M. R. Wasielewski, C. C. Stoumpos and M. G. Kanatzidis, *J. Am. Chem. Soc.*, 2018, **140**, 12226-12238.

136. L. Mao, P. Guo, M. Kepenekian, I. Hadar, C. Katan, J. Even, R. D. Schaller, C. C. Stoumpos and M. G. Kanatzidis, *J. Am. Chem. Soc*, 2018, **140**, 13078-13088.
137. H. Krautscheid and F. Vielsack, *Angew. Chem. Int. Ed. Engl.* 1995, **34**, 2035-2037.
138. M. Safdari, A. Fischer, B. Xu, L. Kloo and J. M. Gardner, *J. Mater. Chem. A*, 2015, **3**, 9201-9207.
139. H.-B. Duan, S.-S. Yu, S.-X. Liu and H. Zhang, *Dalton Trans.*, 2017, **46**, 2220-2227.
140. T. Kollek, D. Gruber, J. Gehring, E. Zimmermann, L. Schmidt-Mende and S. Polarz, *Angew. Chem. Int. Ed.*, 2015, **54**, 1341-1346.
141. L. Zhang, W. Zheng, S. Li, J. Han, W. Jiang and D. Jia, *Inorganica Chimica Acta*, 2019, **484**, 104-110.
142. T. Kollek, C. Fischer, I. Göttker-Schnetmann and S. Polarz, *Chem. Mater.*, 2016, **28**, 4134-4138.
143. Y. Arora, C. Seth and D. Khushalani, *Langmuir*, 2019, **35**, 9101-9114.
144. O. J. Weber, K. L. Marshall, L. M. Dyson and M. T. Weller, *Acta Crystallogr. B*, 2015, **71**, 668-678.
145. H. Krautscheid, F. Vielsack and N. Klaassen, *Z. Anorg. Allgem.Chem.*, 1998, **624**, 807-812.
146. S. Mishra, E. Jeanneau, S. Daniele, G. Ledoux and P. N. Swamy, *Inorg. Chem.*, 2008, **47**, 9333-9343.
147. H. Krautscheid, C. Lode, F. Vielsack and H. Vollmer, *J. Chem. Soc., Dalton Trans.*, 2001, DOI: 10.1039/B009488I, 1099-1104.
148. B. Febriansyah, T. M. Koh, R. A. John, R. Ganguly, Y. Li, A. Bruno, S. G. Mhaisalkar and J. England, *Chem. Mater.*, 2018, **30**, 5827-5830.
149. Y. Chen, Z. Yang, C.-X. Guo, C.-Y. Ni, H.-X. Li, Z.-G. Ren and J.-P. Lang, *CrystEngComm*, 2011, **13**, 243-250.
150. J.-J. Liu, Y.-F. Guan, C. Jiao, M.-J. Lin, C.-C. Huang and W.-X. Dai, *Dalton Trans.*, 2015, **44**, 5957-5960.
151. J.-J. Liu, Y. Chen, M.-J. Lin, C.-C. Huang and W.-X. Dai, *Dalton Trans.*, 2016, **45**, 6339-6342.
152. X. Li, J. Yang, Z. Song, R. Chen, L. Ma, H. Li, J. Jia, J. Meng, X. Li, M. Yi and X. Sun, *ACS Appl. Energy Mater.*, 2018, **1**, 4467-4472.
153. M.-H. Tremblay, A. M. Zeidell, S. Rigin, C. Tyznik, J. Bacsa, Y. Zhang, K. A. Kurdi, O. D. Jurchescu, T. V. Timofeeva, S. Barlow and S. R. Marder, *Inorg. Chem.*, 2020, **59**, 8070-8080.
154. A. H. Proppe, M.-H. Tremblay, Y. Zhang, Z. Yang, R. Quintero-Bermudez, S. O. Kelley, S. Barlow, S. R. Marder and E. H. Sargent, *J. Phys. Chem. C*,, 2020, **124**, 24379-24390.
155. N. Louvain, W. Bi, N. Mercier, J.-Y. Buzaré, C. Legein and G. Corbel, *Dalton Trans.*, 2007, 965-970.
156. Z.-F. Yao, J.-Y. Wang and J. Pei, *Cryst. Growth Des.*, 2018, **18**, 7-15.
157. C. Zhou, H. Lin, Y. Tian, Z. Yuan, R. Clark, B. Chen, L. J. van de Burgt, J. C. Wang, Y. Zhou, K. Hanson, Q. J. Meisner, J. Neu, T. Besara, T. Siegrist, E. Lambers, P. Djurovich and B. Ma, *Chem. Sci.*, 2018, **9**, 586-593.
158. S. Öz, J.-C. Hebig, E. Jung, T. Singh, A. Lepcha, S. Olthof, F. Jan, Y. Gao, R. German, P. H. M. van Loosdrecht, K. Meerholz, T. Kirchartz and S. Mathur, *Solar Energy Mater. Solar Cells*, 2016, **158**, 195-201.
159. O. J. Weber, K. L. Marshall, L. M. Dyson and M. T. Weller, *Acta Crystallogr. B*, 2015, **71**, 668-678.
160. B. R. Vincent, K. N. Robertson, T. S. Cameron and O. Knop, *Can. J. Chem.*, 1987, **65**, 1042-1046.
161. H. Lin, C. Zhou, Y. Tian, T. Siegrist and B. Ma, *ACS Energy Lett.*, 2018, **3**, 54-62.
162. M.-G. Ju, J. Dai, L. Ma, Y. Zhou and X. C. Zeng, *J. Am. Chem. Soc.*, 2018, **140**, 10456-10463.
163. G. Giorgi and K. Yamashita, *J. Phys. Chem. Lett.*, 2016, **7**, 888-899.
164. N. Louvain, N. Mercier, J. Luc and B. Sahraoui, *Eur. J. Inorg. Chem.*, 2008, **2008**, 3592-3596.
165. Y.-Y. Zheng, G. Wu, H.-Z. Chen and M. Wang, *Acta Crystallogr. E*, 2007, **63**, m504-m506.
166. H. Krautscheid and F. Vielsack, *Angew. Chem. Int. Ed. Engl.*, 1995, **34**, 2035-2037.
167. A. Lemmerer and D. G. Billing, *CrystEngComm*, 2012, **14**, 1954-1966.
168. E. R. T. Tiekink and J. Zukerman-Schpector, *Aust. J. Chem.*, 2010, **63**, 535-543.
169. J. M. Harrowfield, S. Maghaminia and A. A. Soudi, *Inorg. Chem.*, 2004, **43**, 1810-1812.
170. M. Payehghadr, S. Yousefi and A. Morsali, *J. Organomet. Chem.*, 2008, **693**, 2514-2518.
171. B.-G. Chen, *Inorg. Nano-Met. Chem.*, 2017, **47**, 1220-1225.
172. A. C. Véron, A. Linden, N. A. Leclaire, E. Roedern, S. Hu, W. Ren, D. Rentsch and F. A. Nüesch, *J. Phys. Chem. Lett.*, 2018, **9**, 2438-2442.
173. C.-H. Wang, C.-J. Ma, Z.-P. Huang, Y.-X. Zai, Q. Yang, L. Li, Y. Liang and Y.-Y. Niu, *J. Clust. Sci.*, 2015, **26**, 1027-1039.
174. A. E. Maughan, J. A. Kurzman and J. R. Neilson, *Inorg. Chem.*, 2015, **54**, 370-378.
175. G.-N. Liu, J.-R. Shi, X.-J. Han, X. Zhang, K. Li, J. Li, T. Zhang, Q.-S. Liu, Z.-W. Zhang and C. Li, *Dalton Trans.*, 2015, **44**, 12561-12575.
176. V. Chakravarthy and A. M. Guloy, *Chem. Commun.*, 1997, 697-698.

177. M. Safdari, A. Fischer, B. Xu, L. Kloo and J. M. Gardner, *J. Mater. Chem. A*, 2015, **3**, 9201-9207.
178. J. Cao, X. Jing, J. Yan, C. Hu, R. Chen, J. Yin, J. Li and N. Zheng, *J. Am. Chem. Soc.*, 2016, **138**, 9919-9926.
179. M. A. Tershansy, A. M. Goforth, L. Peterson, M. C. Burns, M. D. Smith and H.-C. zur Loye, *Solid State Sci.*, 2007, **9**, 895-906.
180. H. Miyamae, H. Nishikawa, K. Hagimoto, G. Hihara and M. Nagata, *Chem. Lett.*, 1988, **17**, 1907-1910.
181. G. Vijaya Prakash, K. Pradeesh, R. Ratnani, K. Saraswat, M. E. Light and J. J. Baumberg, *J. Phys. D Appl. Phys.*, 2009, **42**, 185405.
182. A. Nowak-Król, K. Shoyama, M. Stolte and F. Würthner, *Chem. Commun.*, 2018, **54**, 13763-13772
183. J.-i. Fujisawa, N. Tajima, K. Tamaki and M. Shimomura, *J. Phys. Chem. C*, 2007, **111**, 1146-1149.
184. R. E. Dawson, A. Hennig, D. P. Weimann, D. Emery, V. Ravikumar, J. Montenegro, T. Takeuchi, S. Gabutti, M. Mayor, J. Mareda, C. A. Schalley and S. Matile, *Nat. Chem.*, 2010, **20**, 533-538.
185. Z. Zhao, F. Zhang, X. Zhang, X. Yang, H. Li, X. Gao, C.-a. Di and D. Zhu, *Macromolecules*, 2013, **46**, 7705-7714.
186. Most crystals were measured in the plane of the long axis, with the shorter dimension of the crystal perpendicular to the electrical contacts.
187. A. Zeb, Z. Sun, A. Khan, S. Zhang, T. Khan, M. A. Asghar and J. Luo, *Inorg. Chem. Front.*, 2018, **5**, 897-902.
188. T. Li, A. M. Zeidell, G. Findik, W. A. Dunlap-Shohl, J. Euvrard, K. Gundogdu, O. D. Jurchescu and D. B. Mitzi, *Chem. Mater.*, 2019, **31**, 4267-4274.
189. W. Peng, J. Yin, K.-T. Ho, O. Ouellette, M. De Bastiani, B. Murali, O. El Tall, C. Shen, X. Miao, J. Pan, E. Alarousu, J.-H. He, B. S. Ooi, O. F. Mohammed, E. Sargent and O. M. Bakr, *Nano Lett.*, 2017, **17**, 4759-4767.
190. C. C. Stoumpos, C. D. Malliakas and M. G. Kanatzidis, *Inorg. Chem.*, 2013, **52**, 9019-9038.
191. L. Gao, K. Zeng, J. Guo, C. Ge, J. Du, Y. Zhao, C. Chen, H. Deng, Y. He, H. Song, G. Niu and J. Tang, *Nano Lett.*, 2016, **16**, 7446-7454.
192. H. Deng, X. Yang, D. Dong, B. Li, D. Yang, S. Yuan, K. Qiao, Y.-B. Cheng, J. Tang and H. Song, *Nano Lett.*, 2015, **15**, 7963-7969.

## V. STATISTICAL INFORMATION

### V.1. Publications

*Journal Articles (during program to date)*


1. M.-H. Tremblay, F. Thouin, J. Leisen, J. Bacsa, A. R. Srimath Kandada, J. M. Hoffman, M. G. Kanatzidis, A. D. Mohite, C. Silva, S. Barlow, S. R. Marder, "$(4NPEA)_2PbI_4$ (4NPEA = 4-Nitrophenylethylammonium): Structural, NMR, and Optical Properties of a 3 × 3 Corrugated 2D Hybrid Perovskite", *J. Am. Chem. Soc.*, **2019**, *141*, 4521-4525 (doi: 10.1021/jacs.8b13207).

2. R. B. M. Hill, S.-H. Turren-Cruz, F. Pulvirenti, W. R. Tress, S. Wieghold, S. Sun, L. Nienhaus, M. Bawendi, T. Buonassisi, S. Barlow, A. Hagfeldt, S. R. Marder, J.-P. Correa-Baena, "Phosphonic Acid Modification of the Electron Selective Contact: Interfacial Effects in Perovskite Solar Cells", *ACS Appl. Energy Mater.*, **2019**, *24*, 2402-2408 (doi: 10.1021/acsaem.9b00141).

3. N. K. Noel, S. N. Habisreutinger, Alba Pellaroque, F. Pulvirenti, B. Wenger, F. Zhang, Y.-H. Lin, O. G. Reid, J. Leisen, Y. Z. Barlow, Seth R. Marder, A. Kahn, H. J. Snaith, C. B. Arnold, B. P. Rand, "Interfacial charge-transfer doping of metal halide perovskites for high performance photovoltaics", *Energy Environ. Sci.*, **2019**, *12*, 3036-3073, doi: 10.1039/c9ee01773a.

4. J. Avila, M.-G. La-Placa, E. Longhi, M. Sessolo, S. Barlow, S. R. Marder, H. J. Bolink, "Ruthenium pentamethylcyclopentadienyl mesitylene dimer: a sublimable n-dopant and electron buffer layer for efficient n-i-p perovskite solar cells", *J. Mater. Chem. A*, **2019**, *7*, 25796-25801. doi: 10.1039/C9TA09838K.

5. M.-H. Tremblay, J. Bacsa, B. Zhao, F. Pulvirenti, S. Barlow, S. R. Marder, "Structures of $(4\text{-}Y\text{-}C_6H_4CH_2NH_3)_2PbI_4$ {Y = H, F, Cl, Br, I}: Tuning of Hybrid Organic Inorganic Perovskite Structures from Ruddlesden-Popper to Dion-Jacobson Limits", *Chem. Mater.*, **2020**, *31*, 6145-6153, doi: 10.1021/acs.chemmater.9b01564.

6. M.-H. Tremblay, K. Schutt, Y. Zhang, J. Lim, Y.-H. Lin, J. H. Warby, S. Barlow, H. J. Snaith, S. R. Marder, "A Photo-Crosslinkable Bis-Triarylamine Side-Chain Polymer as a Hole-Transport Material for Stable Perovskite Solar Cells", *Sustain. Energy Fuels*, **2020**, *4*, 190-198, doi: 10.1039/c9se00513g.

7. M.-H. Tremblay, A. M. Zeidell, S. Rigin, C. Tyznik, J. Bacsa, Y. Zhang, K. A. Kurdi, O. D. Jurchescu, T. V. Timofeeva, S. Barlow, S. R. Marder, "Structural Diversity in 2,2'-[Naphthalene-1,8:4,5-bis(dicarboximide)-N,N'-diyl]-bis(ethylammonium) Iodoplumbates", *Inorg. Chem.*, **2020**, *59*, 8070-8080. doi: 10.1021/acs.inorgchem.0c00165.

8. M.-H. Tremblay, J. Bacsa, S. Barlow, S. R. Marder, "Exciton-band tuning induced by the width of the cation in 2D lead iodide perovskite hybrids", *Mater. Chem. Front.*, **2020**, *4*, 2023-2028. doi: 10.1039/D0QM00118J

9. A. H. Proppe, M.-H. Tremblay, Y. Zhang, Z. Yang, R. Quintero-Bermudez, S. O. Kelley, S. Barlow, S. R. Marder, E. H. Sargent, "Napthalenediimide Cations Inhibit 2D Perovskite Formation and Facilitate Subpicosecond Electron Transfer", *J. Phys. Chem. C*, **2020,** *124*, 24379-24390. doi: acs.jpcc.0c05521.

10. M.-H. Tremblay, K. Schutt, Y. Zhang, S. Barlow, H. J. Snaith, S. R. Marder, "A polymeric bis(di-*p*-anisylamino)fluorene hole-transport material for stable n-i-p perovskite solar cells", *New J. Chem.*, **2021**, *45*, 15017-15021. doi: 10.1039/D0NJ04157B.

11. M.-H. Tremblay, K. Schutt, F. Pulvirenti, T. Schultz, B. Wegner, X. Jia, Y. Zhang, E. Longhi, R. R. Dasari, C. Fuentes Hernandez, B. Kippelen, N. Koch, H. J. Snaith, S. Barlow, S. R. Marder, "Benzocyclobutene Polymer as an additive for a benzocyclobutene-fullerene: application in stable p-i-n perovskite solar cells", *J. Mater. Chem. A*, **2021**, *9*, 9347-9353. doi: 10.1039/D0TA07733J.

12. D. A. Valverde-Chávez, E. Rojas-Gatjens, J. Williamson, S. Jariwala, Y. Shi, D. P. McCarthy, S. Barlow, S. R. Marder, D. S. Ginger, C. Silva-Acuña, "Nonlinear Photocarrier Dynamics and the Role of Shallow Traps in Mixed-Halide Mixed-Cation Hybrid Perovskites", *J. Mater. Chem. C* **2021,** *9*, 8204-8212.

13. M.-H. Tremblay, A. Boyington, S. Rigin, J. Jiang, J. Bacsa, K. Al Kurdi, V. N. Khrustalev, R. Pachter, T. V. Timofeeva, N. Jui, S. Barlow, S. R. Marder, "Organic Iodoplumbates: Role of Organic Cation Structure in Obtaining 1D Chains of Face-Sharing Octahedra vs. 2D Perovskites", under revision.

14. S. Dahlström. S. Wilken, Y. Zhang, C. Ahläng, S. Barlow, M. Nyman, S. R. Marder, R. Österbacka, "Cross-Linking of Doped Organic Semiconductor Interlayers for Organic Solar Cells: Potential and Challenges" under revision.

*Book Chapters*

none

*Presentations*

1. S. Barlow, SPIE Optics and Photonics 2018, San Diego, August 19$^{th}$-23$^{th}$ 2018
2. S. R. Marder, International Conference on Interfaces in Organic and Hybrid Thin-Film Optoelectronics (INFORM19), Valencia, Spain, March 5$^{th}$-7 $^{th}$, 2019
3. Seth R. Marder, 14$^{th}$ International Symposium on Functional π-Electron Systems in Berlin, Germany, June 2$^{nd}$-7$^{th}$ 2019.
4. S. Barlow, Air Force Research Laboratory, Dayton, OH, June 7$^{th}$, 2019.
5. S. Marder, 47th IUPAC World Chemistry Congress (IUPAC-2019), Paris, France, July 12$^{th}$-17$^{th}$, 2019.
6. H. J. Snaith, Sungkyun International Solar Forum (SISF 2019), Seoul, South Korea, June 19$^{th}$-21$^{st}$, 2019.
7. S. R. Marder, Cambridge Display Technology, Cambridge, UK, September 2019.
8. S. R. Marder, Air Force Research Laboratory, Dayton, OH, January, 2020.
9. H. J. Snaith, International Conference on Perovskite, Organic Photovoltaics and Optoelectronics (IPEROP-20), Tsukuba, Japan, January 20$^{th}$-22$^{nd}$, 2020.

10. S. R. Marder, Princeton University, Princeton, NJ, February, 2020.

11. H. J. Snaith, International Conference on Hybrid and Organic Photovoltaics (online), July 5th-8th, 2020.

*PhD Theses (during program to date)*

Federico Pulvirenti, "Redox-Active Organometallic Compounds as n-Dopants and Surface Modifiers in Optoelectronics", Georgia Institute of Technology, March 2019

Marie-Hélène Tremblay, "Development of Guidelines Towards an Understanding of the Structure of the Cation – Structure of the Hybrid Haloplumbate Material Relationship", Georgia Institute of Technology, August 2020

Farzaneh Saeedifard, "Doping of Organic Semiconductors: Effects of Crosslinking and Dopant Substituents", Georgia Institute of Technology, November 2021

**V.2. Participants Supported for the No Cost Extension period (08/15/20-08/14/2021)**

Seth R. Marder
Person-months supported: de minimus
ORCID: 0000-0001-6921-2536
project role: PI
contribution: overall oversight of the project and of synthetic aspects in particular
international collaboration: yes
international travel: no

Stephen Barlow
Person-months supported: 3 calendar months
ORCID: 0000-0001-9059-9974
project role: Research Scientist
contribution: supervision of graduate students, assistance with experimental design and interpretation, assistance with reporting and publications
international collaboration: yes
international travel: no

Timothy Parker
Person-months supported: 1 calendar months
project role: Research Scientist
contribution: supervision of graduate students, assistance with experimental design and interpretation
international collaboration: yes
international travel: no

Yadong Zhang
Person-months supported: 1 calendar month
project role: Research Scientist
contribution: supervision of graduate students, synthesis of transport materials
international collaboration: yes
international travel: no

Denise Bale
Person-months supported: de minimus
project role: Research Scientist
contribution: assistance with reporting and publications
international collaboration: yes
international travel: no

Marie-Hélène Tremblay
Person months supported: de minimis
project role: Graduate Student
contribution: synthesis of transport materials and low-dimensional perovskites and related materials, work with Snaith group on device fabrication and testing
international collaboration: yes,
international travel: no

Farzaneh Saeedifard
Person months supported: 4 calendar months
project role: Graduate Student
contribution: synthesis of transport materials and dopants
international collaboration: yes
international travel: no

Henry J. Snaith
Person months supported: 1 calendar month
ORCID: 0000-0001-8511-790X
project role: coPI
contribution: synthesis of transport materials and low-dimensional perovskites and related materials
international collaboration: yes
international travel: no

Derek Hollman
Person months supported: 11 months supported
project role: Postdoctoral Fellow
contribution: fabrication and testing of perovskite films and solar cells, including those incorporating ionic additives
international collaboration: yes
international travel: no

Adam Taylor
Person months supported: de minimis
project role: Laboratory and Project Engineer
contribution: f contribution: supervision of postdoctoral researcher, assistance with experimental design and interpretation
international collaboration: yes
international travel: no

**V.3. Collaborators**

Abo Akademie, Finland (collaboration with R. Österbacka group)
AFRL (collaboration with R. Pachter's group)
Emory University (collaboration with N. Jui's group)
Humboldt University of Berlin, Germnay (collaboration with N. Koch's group)
MIT (collaboration with Shijun Sun)
National Renewable Energy Laboratory (collaboration with S. N. Habisreutinger and O. G. Reid)
New Mexico Highlands University (collaboration with T. V. Timofeeva's group)
Northwestern University (collaboration with M. G. Kanatzidis group)
Princeton University (collaboration with B. Rand and A. Kahn's groups)
Rice University (collaboration with A. Mohite)
Wake Forest University (collaboration with O. Jurcescu's group)

**V.4. Patents etc.**

None.